DEVELOPMENT OF PHOTO-ACTIVE SEMI SHELLS AND HOST SPECIFIC QUANTUM CLUSTERS FOR THERAPEUTIC APPLICATIONS

KRITIKA SOOD

A thesis submitted for the partial fulfillment of the

degree of Doctor of Philosophy

Institute of Nano Science and Technology (INST)

Knowledge City, Sector 81, SAS Nagar, Manauli PO, Mohali, 140306, Punjab, India.

Indian Institute of Science Education and Research, Mohali (IISER)

Knowledge City, Sector 81, SAS Nagar, Manauli PO, Mohali, 140306, Punjab, India.

MARCH, 2024

Dedicated to

My parents

For their unconditional love, unwavering support and tireless efforts

To shape me for a better future

My grandparents

Whose heavenly blessings and desire to make me a ‘Doctor’

Is coming to fruition

The Almighty God

Who held my hand at every step and became my beacon in moments of despair

Declaration

The work presented in this thesis has been carried out by me under the guidance of Dr. Asifkhan Shanavas at the Institute of Nano Science and Technology (INST), Mohali. This work has not been submitted in part or in full for a degree, a diploma, or a fellowship to any other university or institute. Whenever contributions of others are involved, every effort is made to indicate this clearly, with due acknowledgement of collaborative research and discussions. This thesis is a bona fide record of original work done by me and all sources listed within have been detailed in the bibliography.

Kritika Sood

In my capacity as the supervisor of the candidate's thesis work, I certify that the above statements by the candidate are true to the best of my knowledge.

Dr. Asifkhan Shanavas

Scientist-D

Institute of Nano Science and Technology, Mohali

Acknowledgement

उद्यमेन हि सिद्ध्यन्तिकार्याणि न मनोरथैः।

नहि सुप्तस्य सिंहस्यमुखे प्रविशन्ति मृगाः।।

First and foremost, I would like to acknowledge **Dr. Asifkhan Shanavas**, my mentor, without whose guidance, support and expertise, this endeavour would not have been possible. His immense knowledge, patience, and encouragement have allowed me to constantly improve and evolve both as a person and as a researcher. I have learned a lot from sir during our brainstorming ideas/discussion sessions that always left me with enthusiasm and renewed my passion for research each time, for which I shall be forever grateful to him.

I am extremely thankful towards my Ph.D. committee members, Dr. Sharmistha Sinha and Dr. Kamalakannan Kailasam who have provided me valuable feedback during yearly evaluations. I extend my gratitude towards our collaborators, Prof. Abhijit De and Ms. Sulagna Rath at ACTREC, Mumbai for carrying out tumor regression studies on CD1 nude mice. Prof. Reena Das and Dr. Manu at PGI, Chandigarh are acknowledged for obtaining the necessary ethical approvals for carrying out research with human blood and components. Dr. Sonalika is highly acknowledged for providing insights into MOF structure that helped in shaping the work.

I am extremely thankful to Department of Science and Technology **(DST-INSPIRE**) for providing me PhD fellowship. My immense gratitude to Prof. Amitava Patra, Director, INST for providing infrastructural support and to the INST administration (finance, technical and support staff) for their hardwork.

My friends and colleagues have helped me a lot during my tenure at INST; both in providing research based help as well as boosting my morale during tough times. Special thanks to Dr. Deepika Rani and Dr. Praveen who had provided me with technical help, despite their own busy schedules. It was a pleasure knowing and learning from such seniors. I would like to extend my gratitude to all my labmates at ION+ lab: Purvi, Pranjali, Priyanka for help with few experiments; Mahendran and Johns for making food arrangements for my thesis seminar. A special note of thanks to Johns, who gave me his laptop for adding citations to my thesis at last minute, when my citation manager crashed. I hope your kindness is reciprocated many folds.

Finally, I would like to thank **my parents (Mr. Anil Sood and Mrs. Anjana Sood)** and **my brother (Mr. Ashish Sood)** who have stood by me through thick and thin and always motivated me to become a better version of myself. Without them, I would definitely have been a lost cause. I whole-heartedly dedicate my PhD thesis to their unconditional support, love and encouragement. I am extremely blessed to receive the heavenly blessings of **my Grandparents Sh. KC Sood and Smt. Raj Sood** and will forever strive to make them proud of me. I am thankful to my furry best friend, **Calvin (Kevy)** for bringing joy & happiness in my life.

However, **the Almighty** can never be thanked enough for the uncountable blessings he has bestowed upon me!

Abstract

Noble metals, especially gold and silver, have been used as nanocolloids for the treatment of various diseases dating back to as early as 2500 BC. With the advancement of science and development of nanotechnology, these nanomaterials are being extensively used in healthcare applications due to their biocompatibility, anti-inflammatory, and antimicrobial properties complemented by their ease of synthesis, surface modification as well as possible clearance from the body. With size playing major role in determining the optical properties of noble metal based nanoparticles, in this thesis we have explored ~ 200 nm sized nanoparticles with unique semi shell morphology and < 2 nm sized quantum clusters for therapeutic applications.

The first two chapters of the thesis discuss a novel procedure for colloidal gold semi shell (SS) fabrication using nano metal organic framework (MOF) as a sacrificial template and its application in photothermal therapy (PTT). The formation of the SS involves simultaneous anisotropic chemical etching of MOF and in situ nucleation & growth of gold. The as synthesized SS possess a strong localised surface plasmon resonance in the near infrared region, which is retained even after surface passivation with polyethylene glycol and cryopreservation for extended shelf-life. Freshly reconstituted PEGylated SS was found to be hemocompatible & biocompatible under in vitro conditions as well as safe & non-toxic in C57BL/6 mice post intravenous administration for up to 28 days. The PEGylated SS displayed significant photothermal efficiency of ~ 37 % with 808 nm laser irradiation. Preclinical assessment of intra-tumoral photothermal efficacy indicated complete remission of primary breast tumor mass with insignificant metastasis to vital organs. PEGylated SS mediated PTT also yielded morbidity free survival of 75 % in a syngeneic breast tumor model, indicating their suitability to manage advanced breast tumors.

In the next two chapters, we investigated personalised nanomedicine with noble metal (Au and Ag) quantum clusters (QC) stabilized by host derived serum proteins called as NanoSera (QCNS). Due to their ultrasmall size, metal QCs are inherently photoluminescent in nature and can be used as optical tracers in bioimaging. As they are derived from host's serum components, QCNS are highly biocompatible and non-immunogenic. We employed Au-QCNS as radiosensitising agents against hepatoma cells while Ag-QCNS were validated as antibacterial agents *in-vitro*. Pre-clinical safety assessment of autologous QCNS in healthy C57BL/6 mice – including hemocompatibility, inflammatory cytokine analysis, serum biochemical parameters and histopathology of vital organs established their safety post intravenous administration. The proof of concept results demonstrate both Au-QCNS and Ag-QCNS as promising host-specific nanomedicines.

Synopsis

Noble metal nanostructures, especially gold and silver, are being extensively explored for healthcare applications due to their biocompatibility, anti-inflammatory, and antimicrobial properties complemented by their ease of synthesis, surface modification as well as possible clearance from the body. The size and shape dependent tuneability of optical properties motivate several research groups to fabricate and utilise these nanomaterials for a wide variety of biomedical applications. Metal nanoparticles with tailored size and shape exhibit tuneable surface plasmon resonance for application in bio-sensing, therapeutics and diagnostics. Symmetric metal nanoparticles such as gold nano shells can be well explained by the Mie's theory and their plasmonic properties can be tuned by shell thickness and core size. However, asymmetric nanoparticles such as semi shells (or incomplete nano shells) due to the lack of an isotropic plane possess unique plasmonic properties. Nonetheless, the major limitation in arriving at the semi shell (i.e., nano cup, nano cap, half-shell) morphology is the complex multi-step procedure which either a) involves toxic precursors b) requires high temperature conditions c) relies on dissolving the templates by additionally adding harsh etching agents like HF acid and/or d) requires sophisticated instrumentation for anisotropic ablation or etching of material.

To overcome this synthetic challenge, in the first part of the thesis we have developed a rapid colloidal room temperature synthetic protocol for gold semi shell fabrication using nano metal organic framework as a sacrificial template. The avoidance of any toxic precursor along with simultaneous pH dependant degradation of MOF template in the absence of additional etching agents imparts novelty and uniqueness to this synthetic procedure. A step-by step characterisation involving XRD, FESEM and TEM has been performed in order to elucidate the mechanism of semi shell formation. The semi shells due to their anisotropic morphology depict near infra-red absorbance which enables them to act as excellent photothermal nanotransducers. The semi shells are surface passivated using polyethylene glycol for colloidal stability and preservation of the morphology & optical property after lyophilization for its easy on-demand aqueous reconstitution with increased shelf-life and uncompromised optical and photothermal activity.

Further, we have explored the photothermal efficacy of semi shells for management of metastatic breast cancer. Preliminary hemocompatibility and biocompatibility of PEGylated semi shells were established *in-vitro* accompanied by their acute and sub-acute preclinical

safety assessment in C57BL/6 mice with intravenous dual dosage regimen over a period of 28 days. The PEGylated semi shells were found to be non-toxic and non-immunogenic following which their *in-vitro* and *in-vivo* photothermal therapy (PTT) was assessed using an 808 nm laser. Tumor regression analysis was carried out in 4T1 FL2 breast tumor bearing CD1 nude mice for determining their PTT efficacy and effect on metastasis over a period of 21 days. Additionally, the survival rate with semi shell mediated PTT was established in 4T1 tumor bearing Balb/c mice for up to 3 months to assess their suitability to manage advanced breast tumors.

The second part of the thesis explores metal quantum clusters (QCs) that are a collection of finite number of atoms and exhibit fundamentally unique optical properties owing to their ultra-small size (< 2-3 nm) mediated quantum confinement phenomena. QCs are emerging rapidly since the recent decade due to their unique optical properties including: molecule like absorption, strong photoluminescence and tuneability of core size and ligand choice leading to different emission wavelengths. The ligand not only imparts stability to the core-shell nanocluster morphology but can also provide biocompatibility to the QC and affect their pharmoacokinetic properties *in-vivo*. Biologically derived macromolecular ligands such as nucleic acids or proteins could act as safe scaffolds for QC with improved biocompatibility, water solubility and high photo stability. However, a more precise and personalised approach needs to be followed in order to increase the efficacy and reduce the adverse immunological effects. Taking this into account, we have ventured into the field of personalised nanomedicine by developing gold QC stabilized with whole serum proteome (Nano sera stabilised Au Quantum clusters: Au-QCNS) of bovine, human and murine origin. After establishing their biocompatibility and hemocompatibility with mammalian cells, we also assessed the ability of Au-QCNS to radiosensitize hepatoma cells PLC/PRF5 *in-vitro* as a proof-of concept. The preclinical safety along with non-immunogenicity of autologous Au-QCNS in healthy C57BL/6 mice demonstrated their safe translational potential. Further, we developed silver QC stabilized with serum proteome (Ag-QCNS) and effectively established their *in-vitro* antibacterial activity using E.coli as a model organism. The biocompatibility and migratory abilities were also established *in-vitro* in mammalian fibroblast cell lines. The *in-vivo* hemocompatibility as well as preclinical safety of autologous Ag-QCNS was established over a period of 28 days.

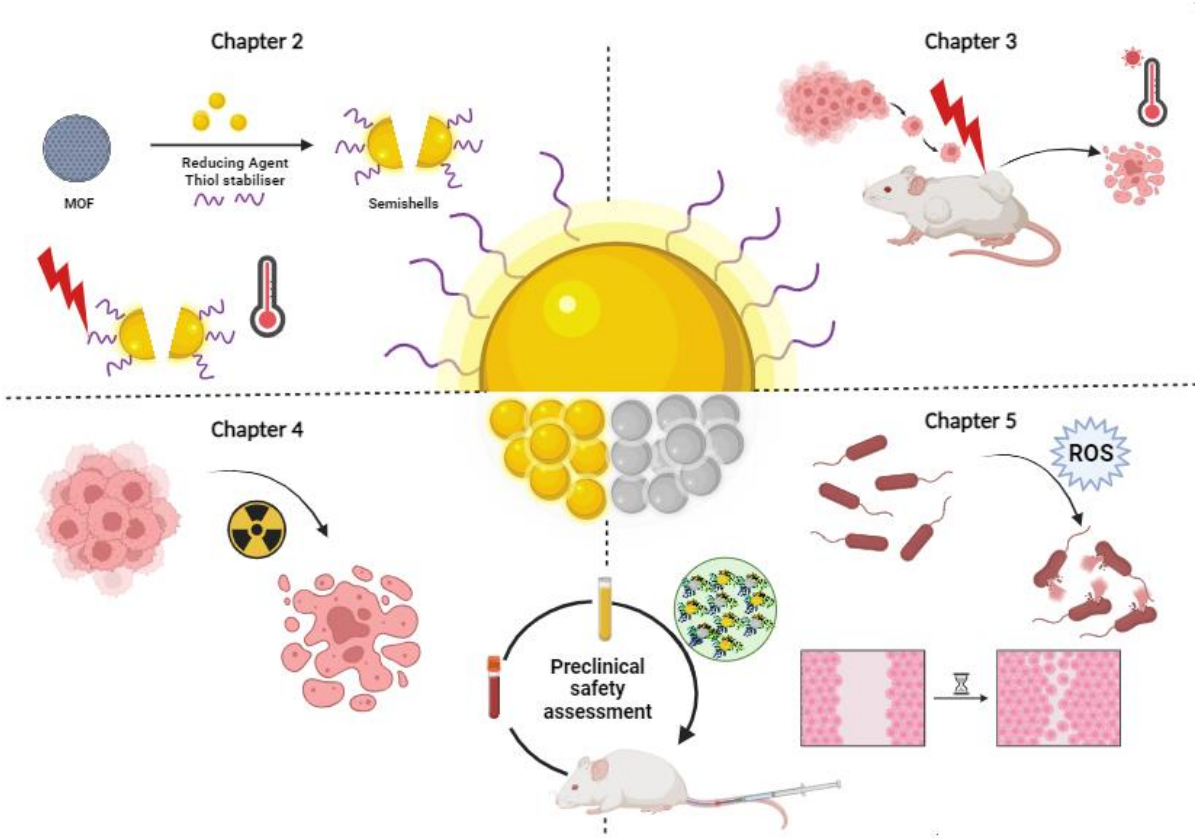

As illustrated in the above figure, all the nanomaterials (semi shells as well as quantum clusters) reported in this thesis have an intrinsic potential for therapeutic (i.e., photothermal therapy, radiation therapy and antibacterial therapy) applications. Further assessment of systemic toxicity and bio distribution in pre-clinical models revealed their safe nature for clinical translation.

Table of Contents

Contents

List of Figures

List of Tables

Chapter 1

INTRODUCTION

1. INTRODUCTION

The history of using noble metals in medicine, especially gold and silver, has an interesting story that dates back to 2500 B.C. originating from the ancient Indian medicine system of Ayurveda wherein fine ground metallic powder or "Bhasma" was used for treatment of wide variety of diseases as well as for providing strength and immunity [1]. In ancient medicinal history, the use of gold in medicine was particularly prevalent in treatment of diseases like tuberculosis, smallpox, measles, rheumatoid arthritis, syphilis as well as skin ulcers. Noble metal nanoparticles (NPs), especially gold and silver NPs, are the most extensively used metal NPs for a wide variety of biomedical applications, which include their anti-cancer, antimicrobial, anti-HIV activities, as well as their use in implantable medical devices such as oral implants and pacemaker devices. Gold NPs are widely used in nanomedicine due to their high biocompatibility in vivo, ease of synthesis and surface modification which makes them a highly attractive nanomaterial for targeted theranostics. Silver complexes are well known for their anti-inflammatory, antibacterial and antiseptic properties. The use of silver nitrate solution in topical ointments especially in burn treatment is prevalent even till date [2].

1.1 Metal Nanoparticles and their tuneable Surface Plasmon Resonance

Nanoparticles exhibit fascinating shape and size dependant properties that are entirely different from their bulk and atomic counterparts. Noble metal nanoparticles have been employed widely in various fields including photonics, energy conversion, spectroscopies, therapeutics, sensing and diagnostic applications. The metallic nanoparticles exhibit unique optical characteristics based on their geometry which has motivated researchers to develop a rapidly expanding array of shapes, such as nano rods, nano shells, semi shells, nano flowers, nano prisms, nano stars, and nano cages to name a few.

When light hits the surface of a conductive nanomaterial, herein metal nanoparticles, electromagnetic field of photons in turn induces the collective coherent oscillation of the metal valence band electrons, known as plasmons. This plasmon cloud induce charge separation on the metal nanoparticle as shown in **Fig 1.1a)**, such that a dipole oscillation is formed along the

direction of the electric field of the incoming photon. The maximal amplitude of these oscillating electrons at a particular frequency is termed as Surface Plasmon Resonance (SPR). **Fig 1.1b)** depicts the shape-dependant plasmon resonances for different nanoparticle morphologies.

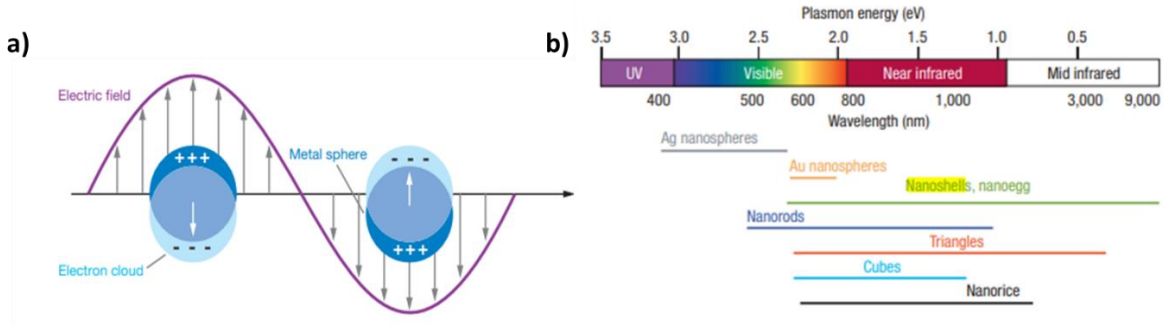

Fig 1.1: a) Localised SPR of metallic nanosphere. Reprinted with permission from [3] b) Plasmonic resonances range for different types of particle morphologies. Reprinted with permission from [4]

Since both the shape and size of metal nanoparticles dictate the spectral signature of its plasmon resonance, hence the ability to change these two geometrical parameters is an important experimental challenge. This enables the researchers to understand their structure-property relationship for rationally designing nanostructures in order to utilise them for a variety of applications.

1.2 Metallic Nano shells

Metallic nano shells (NS) are the one of the most widely studied sub-class of plasmonic nanoparticles that are typically composed of a spherical dielectric core homogenously coated with concentric nanoscale metallic shell. The NS, due to their spherically symmetric shape, can be well described by Mie scattering theory that provides a quantitative description of the scattering and absorption spectra of spherical nanoparticles. The LSPRs of NS are extremely sensitive to the inner and outer dimensions of the metallic shell layer. Hence, their optical properties can be widely varied by tuning the core-shell geometrical parameters. For example, by adjusting the ration between $HAuCl_4$ and Na_2S in Au_2S–Au core–shell NS, they can be grown into different core sizes and shell thickness to yield tuneable LSPR wavelength through the visible, near infrared (NIR), as well as the mid-infra-red regions (400-900 nm). For example, **Fig 1.2** shows that the LSPR of Au-Silica core shell NS exhibits a blue shift as the Au shell thickness increases from 5 nm to 20 nm thickness. Moreover, the SPR of NS is also highly sensitive to the local environment such as the refractive index of the surrounding medium. It has been observed that the LSPR of metal NS red shifts as the refractive index of

the surrounding solution increases [4]. Henceforth, the design of core-shell NS can be altered to attain tuneable LSPR over a wide range of wavelengths (from visible to NIR regions) thereby enabling their applications in a wide variety of fields including photo thermal therapy and optically triggered drug delivery, as well as chemical and single biomolecule sensing applications, including Surface Enhanced Raman Spectroscopic (SERS) applications.

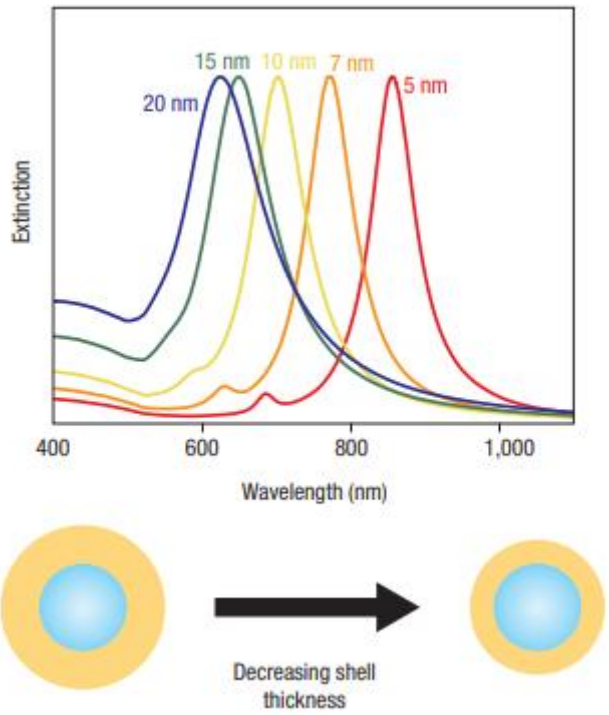

Fig 1.2: Blue-shift in surface plasmon resonance of a silica core (d =120 nm) coated with varying thicknesses of gold shell (5 -20 nm) . Reprinted with permission from [4]**.**

In order to understand the structure-property relationship and to interpret the plasmon resonance of NS, the plasmonic hybridization model was first developed by Halas and Norlander [5]. However, it can also be extended to NS-based geometries with increased structural complexity such as nanomatryushkas, nano eggs and semi shells.

1.3 Metallic Semi Shells: Breaking the Symmetry

Semi Shells or 'incomplete NS' are typically metallic shells with broken symmetry consisting of a dielectric or a hollow core that is only partially covered in metal in contrast to the symmetric metallic NS. The term 'Semi Shell' is a rather generalized denomination as they can be specifically categorized with different terms based on their inner radius (r), outer radius (R), and height (H) as shown in **Fig 1.3**. Upon varying H values, we can have different semi shell (SS) family members such as nano caps (H<R), half-shells (H=R) or nano cups (R<H<2R). Asymmetic shapes such as 'nano crescent moons, 'nano bowls' and 'nano bottles' essentially

fall into one of the above mentioned three categories based on their H:R ratio. Tuning of the core size (r), metal thickness (R/r) and H allows the tuning of optical properties of SS which are characteristic of their unique geometries.

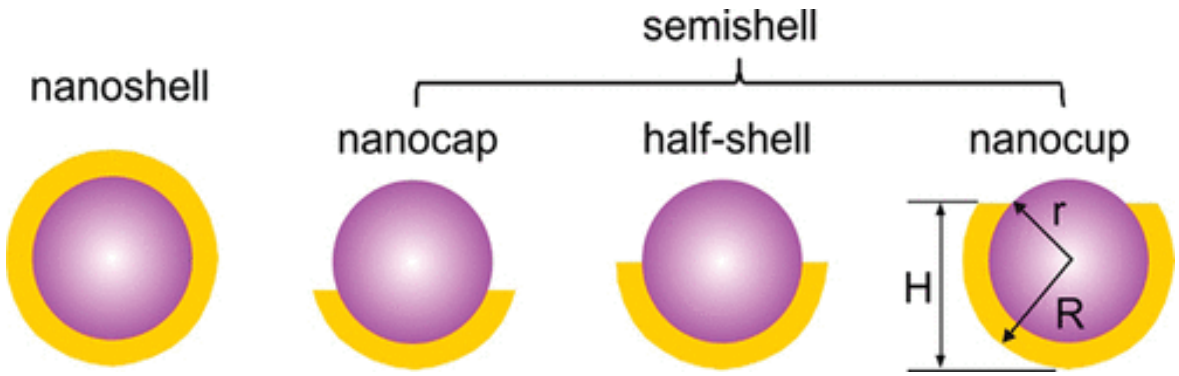

Fig 1.3: Overview of different shell types: (left) a fully covered nano shell with a dielectric core; (right) semi shells categorised based on the fractional height of the metal as nanocap, half-shell or nanocups. Reprinted with permission from [6].

1.3.1 Plasmonic Resonance Modes and Optical Properties of Semi shells

Plasmonic Hybridization (PH) model developed by Halas and Norlander has been utilised to explain the plasmonic dipoles of metallic nanostructure [5]. In a symmetric NS, the plasmonic resonance arises from the hybridisation of two fixed frequency plasmons, i.e. the sphere plasmons (present on the outer surface of metallic shell layer) and the cavity plasmon (present on the inner surface of shell layer). The hybridization of these sphere and cavity based plasmon oscillation modes give rise to 'bonding' and 'antibonding' plasmons. The lower energy symmetric or "bonding" plasmon mode is assigned when the inner and outer surfaces are similarly polarized leading to an overall larger net dipole moment. The higher energy asymmetric or "antibonding" plasmon mode is assigned when the inner and outer surfaces are oppositely polarised leading to an overall smaller net dipole moment. However, in the case of asymmetric metallic structures such as SS or hollow nano bowls, the PH model can be accommodated by allowing the dipolar plasmons of nanoholes to interact with the dipolar and quadrupolar plasmons of NS as shown in **Fig 1.4** leading to 'bonding' and 'antibonding' modes. Due to the asymmetric geometry, the hybridization between the two dipolar modes is stronger than that between the quadrupolar mode and the dipolar mode, resulting in a greater energy splitting.

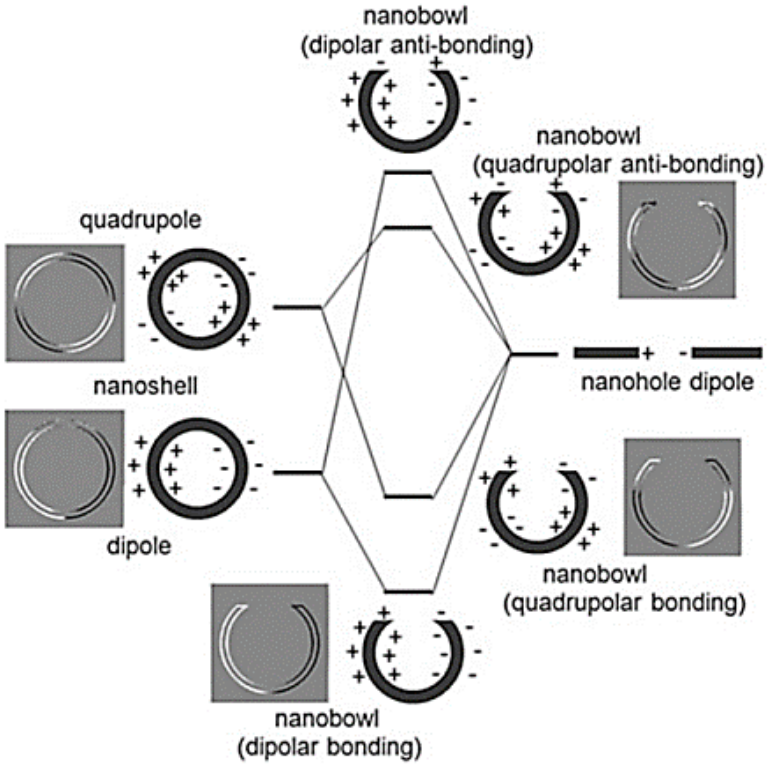

Fig 1.4: Plasmon hybridization model and surface charge distribution for semishell due to interaction between NS and nanohole plasmons. Reprinted with permission from [7].

Hence, in contrast to a single bonding dipole resonance in a symmetric NS, the symmetry-reduced SS exhibit two distinct bonding dipole resonances as shown in **Fig 1.5**. **Axial mode** dipole resonance is exhibited when the incident light is parallel to the axis of symmetry while the **Transverse mode** dipole resonance is exhibited when the incident light is perpendicular to the axis of symmetry of the SS.

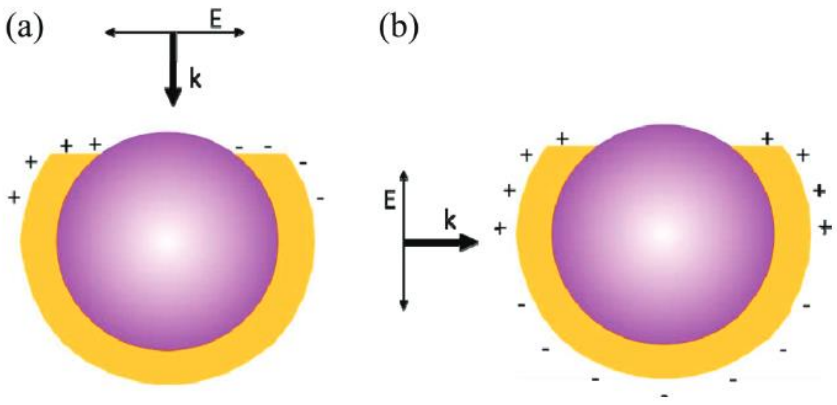

Fig 1.5: Two dipolar plasmon modes in semi shells: (a) the transverse mode and (b) the axial mode. Reprinted with permission from [6].

The inherent asymmetry of these systems leads to the presence of two types of dipole plasmon modes: a blue-shifted axial mode and a red-shifted transverse mode. While the blue-shifted

axial mode is purely electric, theoretical calculations predict that there is also a significant magnetic component in the red-shifted transverse mode [8], [9]. These dipolar resonances display different light-scattering characteristics that are strongly influenced by the angle and polarization of the incident light and by variations in the dielectric environment [8], [9]. Additionally, the optical response can be easily tailored from the visible to NIR by tuning the core radius, metal thickness, and surface coverage. Altogether, plasmonic SS offer a variety of new possibilities for the fabrication of metamaterials with negative refractive indices at NIR and visible frequencies, or of surface-enhanced Raman scattering (SERS) probes. On the basis of the above-described properties, there is a need to develop novel and efficient synthetic methods that allow us to control the morphological and compositional parameters of SS.

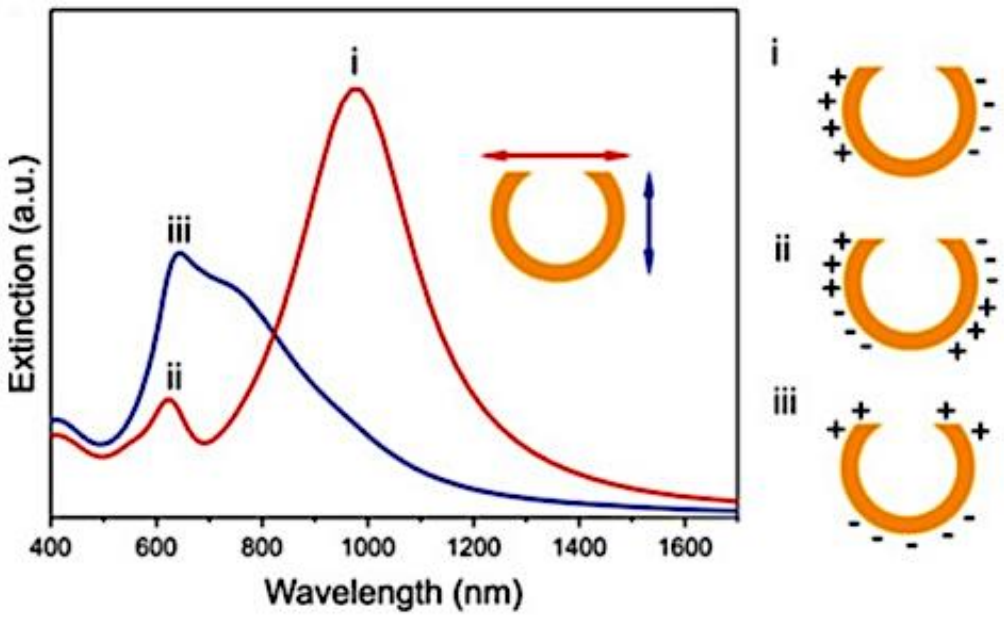

Fig 1.6: Polarization-dependent optical properties calculated for a hollow gold semi shell for transverse and axial polarization (red and blue) respectively. The surface charge distributions at the resonance modes i, ii, and iii are plotted on the side. Reprinted with permission from [10].

The interactions of hollow gold SS with light are different when the light waves are incident in axial and transverse modes as shown in **Fig 1.6**. When the light waves are incidental in transverse mode, the opposite charges gather at the edges of the SS resulting in the formation of a current loop or a magnetic plasmon mode (labelled as i). Additionally, a higher-ordered mode, for example, quadrupolar mode (labelled as ii) may be excited in transverse polarised light. Conversely, in the case of axially polarised light, the electrons within the SS move directly from the top to the bottom, creating an electric dipole mode (labelled as iii). This motion covers a shorter distance, causing a higher frequency, hence shorter wavelength.

However, when the light is polarized at an angle other than horizontal or vertical (obliquely polarised), then both the electric and magnetic modes can be activated together.

1.3.2 Fabrication of Metallic Semi shells

The general experimental methodology behind the fabrication of metallic SS can broadly be classified into two categories: i) Solid state synthesis, and ii) Colloidal state synthesis.

1.3.2.1 Solid State Synthesis

The most obvious approach to SS formation would be to start from nano shells and transform their morphology through different techniques to yield incomplete NS or SS. This is referred to as the 'top down' approach and typically involves two main techniques for SS formation:

1) Anisotropic dry etching of nano shells

Dry-etching methods are used widely to systematically remove a part of NS using sophisticated instrumentation in a systematic and controlled way to yield asymmetric or incomplete NS. This asymmetric etching can be achieved through two procedures:

a) Ion-milling

Ion-milling process utilises energetic beam of xenon ions to bombard the sample surface for a few seconds and in the process the sample is physically etched. The approach as shown in **Fig 1.7** involves synthesis of NS on SiO_2 cores usually through wet-chemistry plating method and their subsequent immobilisation on substrates coated with 3-mercaptopropyltrimethoxysilane or poly(vinyl pyridine) in the form of a monolayer [11]. Thereafter, ion-milling is carried out. The etching rate and depth is dependent on several factors such as the material, intensity of ion beam and time of etching thereby yielding SS of different sizes and aperture diameter. Furthermore, to produce hollow SS, a final vapour HF etching step is carried out to dissolve the SiO_2 template leaving behind hollow 'upward facing' SS. These upward orientations of SS are rather favourable in the application of SERS [12].

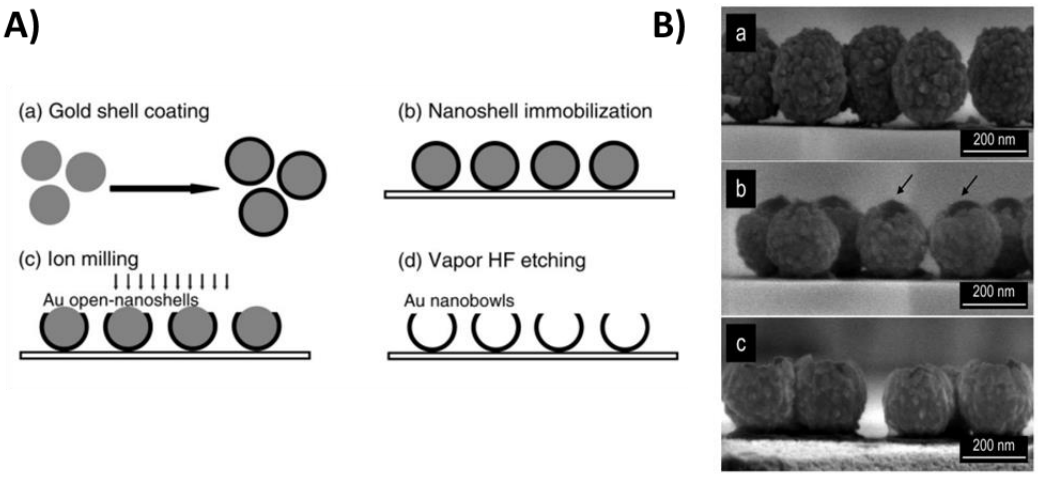

Fig 1.7: A) Schematic on fabrication of Au nanobowls using ion-milling process. B) Side-view SEM images of (a) Self-assembled nanoshells, (b) open nanoshells after ion milling 40 s, and (c) nanobowls after vapor HF etching 45 min. Reprinted with permission from [11].

b) Electron beam-induced ablation

Semi shells can also be prepared through an electron beam-induced ablation (EBIA) process by employing environmental scanning electron microscopy (ESEM) as shown in **Fig. 1.8** [13]. The electron beam from ESEM scans a smaller sample area (~500 nm^2) for simultaneous ablation and monitoring of the etching process in a directional manner. ESEM allows SEM analysis on non-conductive samples through the introduction of H_2O vapour into the vacuum ESEM environment to stabilize surface charging. EBIA involves an incident electron beam inducing a net negative charge on the nanoparticle surface, which then attracts the positively charged H_2O ions to the nanoparticle, resulting in the sputtering of metallic film from the nanoparticle.

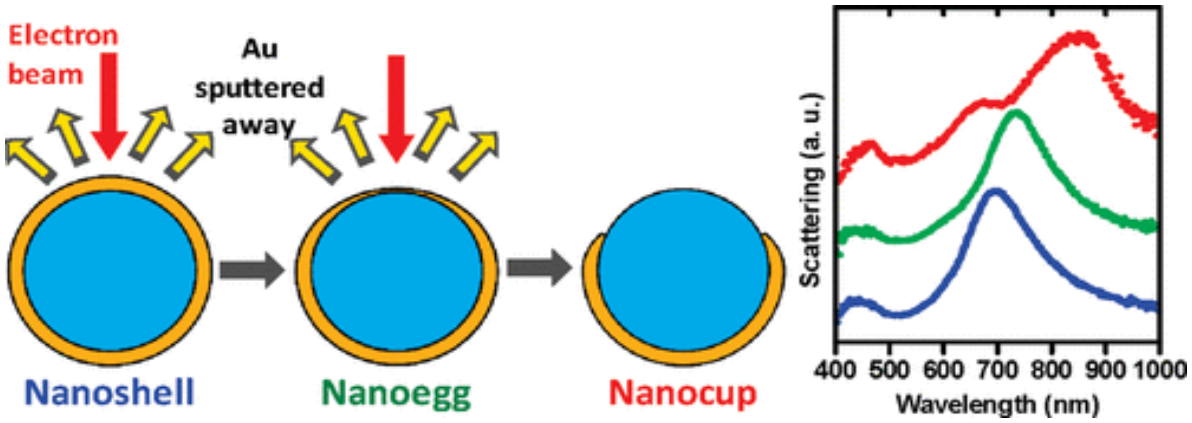

Fig 1.8: Schematic depicting use of the EBIA technique for fabrication of a singular gold semi shell. Reprinted with permission from [13].

Even though both ion milling and EBIA are similar directional dry-etching techniques involving multi-step procedure, the former can fabricate higher density of SS instantaneously over a large area whereas EBIA is more suitable for local and controlled fabrication of a singular SS.

2) Template Deposition strategy

SS can be fabricated by deposition of metallic film coating via either evaporation or sputter coating onto an ordered arrangement of template cores (for example- silica or polystyrene (PS) cores) on the substrate. These could subsequently be separated off from the substrate by the process of sonication as shown in **Fig 1.9a** leading to formation of asymmetric SS due to shadow effect on the template core[14][15]. Thereafter, a wet chemical etching process may further be employed to dissolve the template cores involving HF and toluene/dichloromethane for silica and polystyrene cores respectively. Although simple, this method leads to SS with random orientations which majorly affects their optical properties and SERS based bio-sensing applications.

However, the direct deposition of metal on PS core arrays creates extra metallic truncated tetrahedral NPs on the substrate which have their individual plasmonic response that is separate from the individual SS thereby complicating its accurate analysis. For this reason, a fabrication process involving NS embedded in a poly(dimethylsiloxane) (PDMS) polymer film is preferred that allows tuneable composition and thickness of the metal layer, and a well-controlled orientation of the semi shells. The fabrication process involves metal sputtering on a mono layer of PS particles on the substrate, followed by a curing and peeling of a casted PDMS film on the metallic nanostructures as shown in **Fig 1.9c** [16]. Moreover, introducing a PDMS matrix also decreases the oxidation of certain metals (for example- Ag, Cu, and Al), leading to more precise optical measurement analysis.

Alternatively, SS could also be fabricated by metallic deposition via chemical and electrochemical plating procedures onto template cores. The chemical plating procedure involves template deposition onto a substrate wherein the incomplete or fractional chemical passivation of the template surface is initiated at a particular site followed by NS nucleation and deposition chemistry to selectively coat a particular (unpassivated) section of the template surface with metal. The chemical plating strategy allows the fabrication of SS at any arbitrary yet a conductive substrate. It is worth noting that the chemical technique boasts the advantage

of solely metal-coating the particles, whereas vacuum deposition methods cover the entire surface and require substrate transfer.

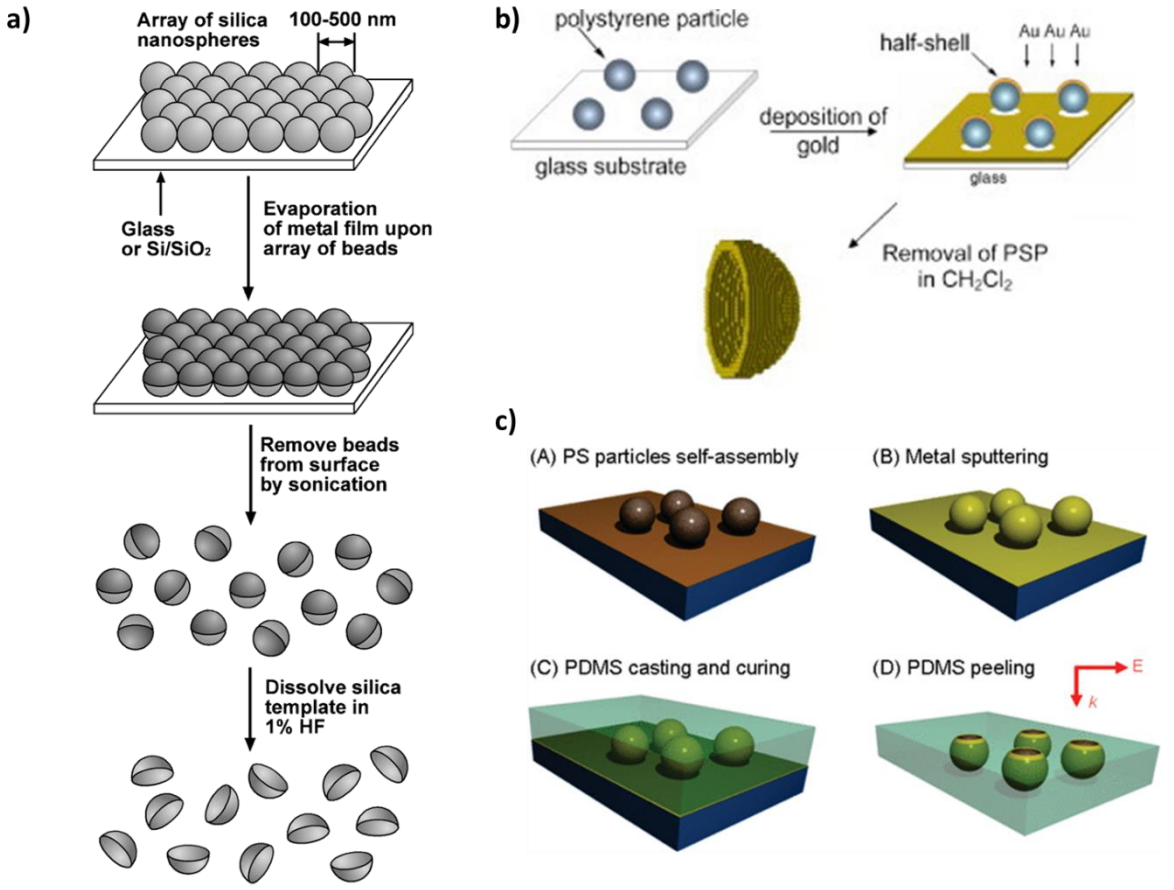

Fig 1.9: Fabrication of semi shells using template deposition strategy: a) By deposition of metallic film coating via evaporation followed by template removal and dissolution, reprinted with permission from [14]. b) By vapour deposition of gold on PS templates followed by template removal in dichloromethane solvent, reprinted with permission from [15]. c) By metal sputtering and casting in PDMS polymer film for preserving optical properties of individual semi shells, reprinted with permission from [16].

1.3.2.2 Colloidal State Synthesis of Semi shells

The recent advances in the preparation of colloidal SS mainly deals with generation of Janus particles that have distinct properties (such as surface functionality, polarity, optical and magnetic properties) on their opposite ends using different templates such as dielectric/ polymeric cores. The core is partially covered with metal to form SS morphologies consisting of half shells, nano caps, or nano cups based upon the metal surface coverage. Fernandez *et. al*. reported the colloidal synthesis of gold SS onto silica nanoparticles wherein partial coverage with metal was achieved through selective amine-functionalization of silica nanoparticles using a masking process based on pickering emulsions resulting in formation of Janus SiO_2@Au

nanoparticles [17]. The selective overgrowth of Au SS occurs on these Janus nanoparticles through a seed-mediated growth process and the fabrication of hollow Au SS was finally achieved by etching the silica cores with hydrofluoric acid solution. Similarly, polystyrene nanoparticles were coated with polyphenylsiloxane protecting patches to prevent partial deposition of metallic Au onto the template surface through a seed mediated growth process [18]. Once the Au is deposited, these patches are dissolved by addition of toluene [**Fig 1.10 A**]. Similar partial blocking technique in combination to galvanic replacement reaction was employed to prepare Au nano bowls [19]. The surface of Fe_3O_4 nanospheres was partially blocked by seed mediated Ag coating to yield heteronanostructures of Ag-Fe_3O_4 and later on a galvanic replacement reaction was carried out between Ag and Au, followed by dissolution of Fe_3O_4 to yield freestanding Au nano bowls. Bimetallic SS have also been reported wherein Au core@Ag SS Janus nanoparticles have been synthesised by a two-step method wherein first the silver shell was chemically deposited onto a gold nanoparticle core resulting in Au@Ag core-shell NP and later on a part of Ag shell was etched away selectively using mixture of H_2O_2 and NH_3 in the water sub phase. This resulted in Janus nanoparticle formation with Ag distributed asymmetrically on the Au core surface, which exhibited enhanced electrocatalytic activity in oxygen reduction reactions as compared to their Au@Ag and Ag@Au core–shell counterparts [20].

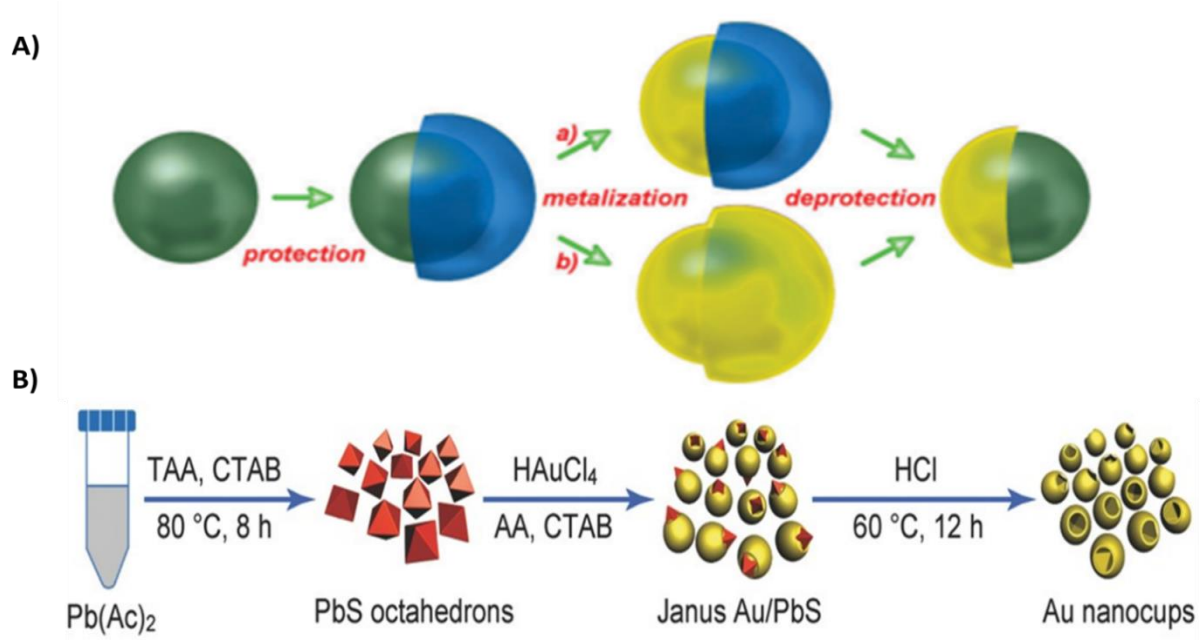

Fig 1.10: A) Colloidal synthesis of gold semi shells by protectant patches: a) Synthesis strategy and (b) actual reaction pathway to realize Au semishells using a polyphenylsiloxane protecting patch (green = crosslinked polystyrene, blue =

polyphenylsiloxane, yellow = gold), reprinted with permission from [18]**. B) Schematic depicting colloidal synthesis of the Au nanocups; reprinted with permission from** [21]**.**

Jiang *et al.* reported colloidal synthesis of gold nano cups using PbS nano octahedrons as sacrificial template for single-vertex initiated selective Au deposition onto Janus Au-PbS nanoparticles. PbS was then dissolved with HCl to ultimately yield Au nano cups [**Fig 1.10 B**] with enhanced magnetic resonance and orientation dependant plasmonic properties [21]. However, each of these methods had their own disadvantages like i) toxic precursors ii) long-tedious multistep procedures iii) need of harsh etchants to dissolve the templates iv) high temperature requirement. Therefore, a rapid colloidal room temperature synthetic procedure without employing non-toxic precursors and/or additional etching agents is need of the hour to facilitate plasmon-enabled applications of Au SS on a larger scale.

1.4 Metal Quantum Clusters

Recent advancements in nanotechnology have introduced a wide range of functional nanomaterials that are being harnessed for therapeutic and diagnostic applications. Among these, metallic quantum clusters (QCs) have gained prominence in recent decades. This surge in interest is primarily due to the growing curiosity in understanding how the optoelectronic properties evolve from the atomic scale to bulk solids as the size of these clusters increases. Metal QCs composed of a few to several hundred metal atoms, act as a crucial link between larger plasmonic metal nanoparticles and individual metal atoms, forming ultra-small nanostructures with sizes generally < 2 to 3 nm. At this scale, the strong quantum effects of electrons result in the division of continuous energy states into discrete electronic states. This gives rise to unique optoelectronic characteristics including a significant Stokes shift, intense photoluminescence, good biocompatibility, and HOMO-LUMO transitions, stemming from a profound quantum confinement effect. These metal QCs are typically composed of a core-shell structure, wherein the core metal atoms are enveloped by organic ligand groups that serve as protective agents, stabilizing the metal core. Different types of ligands can be employed to stabilise the QCs such as thiols (MPA: 3- Mercaptopropionic acid, MUA: 11-Mercaptoundecanoic acid), and bio-macromolecular templates such as DNA, proteins, dendrimers, as shown in **Fig 1.11a**. The ligands predominantly possess thiol groups for the most favourable metal-SH bond formation. Moreover, they act as stabilisers for QCs and avoid agglomeration due to their ultrasmall size. The ligands play an essential role in deciding the atomic precision of QCs as well as their subsequent emission characteristics as shown in **Fig**

1.11b. The ultra-small size of these nanoparticles restricts the free movement of conduction electrons to the metal surface, determining their size-dependent optical properties, largely influenced by the SPR phenomenon. Notably, as these metal nanoparticles decrease in size to the Fermi wavelength of conduction electrons, the band structure undergoes quantization, transitioning from continuous energy bands in nanoparticles to discrete energy levels referred to as HOMO-LUMO energy levels. This quantization of energy levels gives rise to distinct photoluminescent, electronic, and catalytic properties in metal QCs.

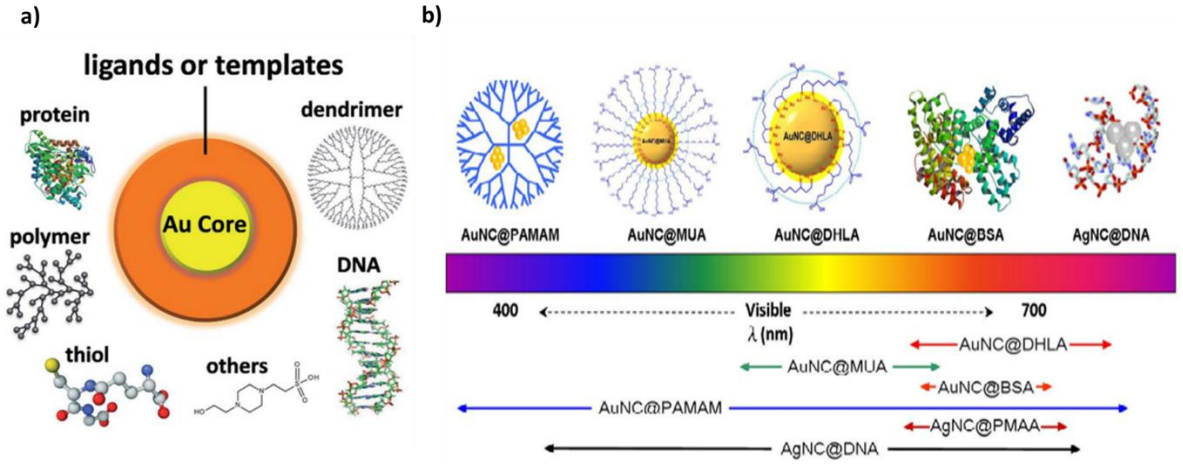

Fig 1.11: a) Different types of ligand groups forming core-shell structure with metal atoms. Reprinted with permission from [22]. b) Different protecting ligands stabilised QCs based on their emission wavelength placed over the spectrum. Reprinted with permission from [23].

In recent years, various metal nanoclusters with diverse metallic cores, such as gold (Au), silver (Ag), platinum (Pt), and copper (Cu), have found substantial utility in theranostic applications. This can be attributed to their exceptional biocompatibility, relatively high cellular uptake, effective renal clearance for *in vivo* applications, ease of conjugation for imparting various functionalities, tuneable quantum yield, tuneable emission in the visible and infrared regions, and good photostability. Of particular interest are the Au and Ag QCs that have gained significant attention in various biomedical domains, including biosensing, therapeutics, and bioimaging. A few of these biomedical applications which are relevant to this thesis including-cancer radio-sensitization and antibacterial therapy have been elaborated in the subsequent sections.

1.5 Cancer Nanotherapy

Cancer in a broader sense refers to the uncontrolled and abnormal cellular proliferation owing to genetic mutations [24]. It is amongst the leading causes of mortality worldwide accounting for ~9.5 million deaths and ~18.1 million new cancer patients per year in 2018 with an expected

rise to ~16.4 million deaths and ~29.5 million new cases per year by the year 2040 [25]. Moreover, tumor relapse and metastasis are a major challenge in the field of oncology due to its diversity in clinical features in different cancer types. Cancer metastasis accounts for ~ 90% of cancer-related morbidity and mortality involving the spread of cancer cells from the primary tumor site to surrounding tissues and distant organs. Once the cancer cells are metastasized to distant organs, it becomes largely incurable and fatal [26]. Hence, the efforts on developing safe and effective cancer therapeutics have been accelerated tremendously in past few decades with a major focus to prevent its relapse. The current clinically employed cancer therapeutic strategies involve the use of aggressive surgery, chemotherapy, and radiotherapy, which although have increased the patient survival rate and life-expectancy suffer from severe side-effects and unsatisfactory results especially in patients with metastatic cancers [27]. Despite the development of new therapeutic strategies such as targeted and combinational therapies for treating metastasis, with little to no improvement in the overall survival expectancy. Typically, in the case of metastatic breast cancer, the 5-year survival rate of patients undergoing intense multimodal treatments is only about 20% [26]. Thus to achieve better clinical outcome, experimental and advanced modalities, such as immunotherapy, gene therapy, photodynamic therapy and photothermal therapy are highly warranted.

1.5.1 Cancer Photothermal Therapy with Plasmonic Nanoparticles

Among the upcoming advanced cancer therapies, photothermal therapy (PTT) by utilising plasmonic nanoparticles is the most attractive therapeutic strategy which is gaining popularity due to its high specificity, minimal invasiveness and precise spatial-temporal selectivity for therapeutic potential. In general, PTT involves the use of NIR laser triggered photo-active agents (PA) that utilize the light energy to generate heat in the localised region for photo-thermal ablation of cancer cells. Typically, the cancer cells show poor endurance to heat. The laser source and dosage can be varied to selectively eliminate the cancer cells of various types and minimize the damage to the surrounding normal tissue. **Fig 1.13** shows the nanomaterial mediated PTT effects in the tumor microenvironment. Once administration into the host, passive accumulation of PA nanomaterials occurs within the solid tumors through the enhanced permeation and retention (EPR) effect wherein they enter the tumor tissue through their leaky vasculature. The PA nanomaterials having strong absorbance in the NIR window can act as excellent nanotransducers by efficiently converting the laser energy to heat energy. For photothermal tumor ablation, the heat (>42 °C) generated during the vibrational relaxation of

the photo-excited PAs is transferred to the tumor tissue. This localized hyperthermia ultimately results in the necrosis, apoptosis, and necroptosis of tumor as shown in **Fig 1.13.**

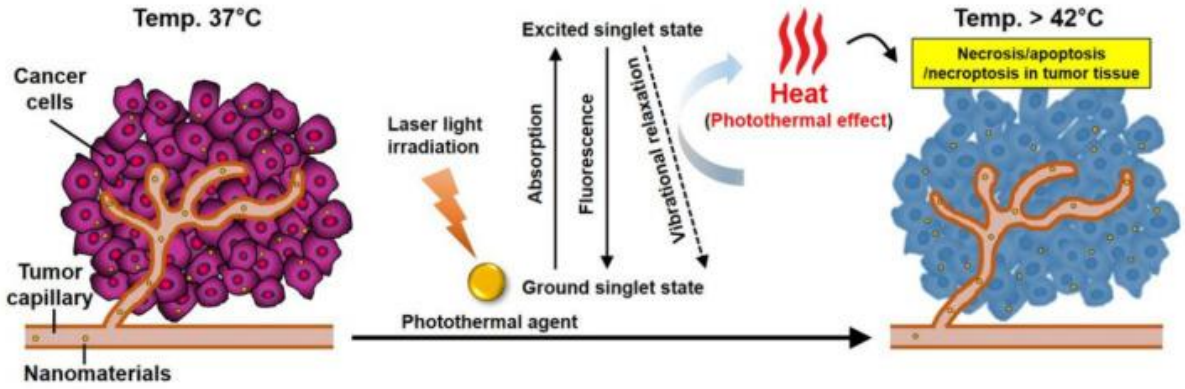

Fig 1.12: Mechanism of nanomaterial-mediated PTT effects in the tumor microenvironment. Reprinted with permission from [28].

To combat cancer metastasis, PTT in isolation or in combination with other therapeutic modalities such as radiotherapy, immunotherapy and chemotherapy have been demonstrated in several metastatic cancer models [29]. PTT alone can be used to directly thermally ablate the cancer cells in primary tumor or local metastasis in lymph node nearby to combat the initial stage of cancer metastasis and supress their further metastasis in distant [29] [30]. This is because at early stages, the main mechanism of cancer metastasis is predominantly due to lymphatic metastasis from the sentinel lymph nodes present near the primary tumor from where the cancer cells start to spread to distant organs as shown in **Fig 1.14.** Hence, the specific targeting of PA to the primary tumor sites and/ or lymph node metastases is an essential precondition for a successful PTT mediated treatment.

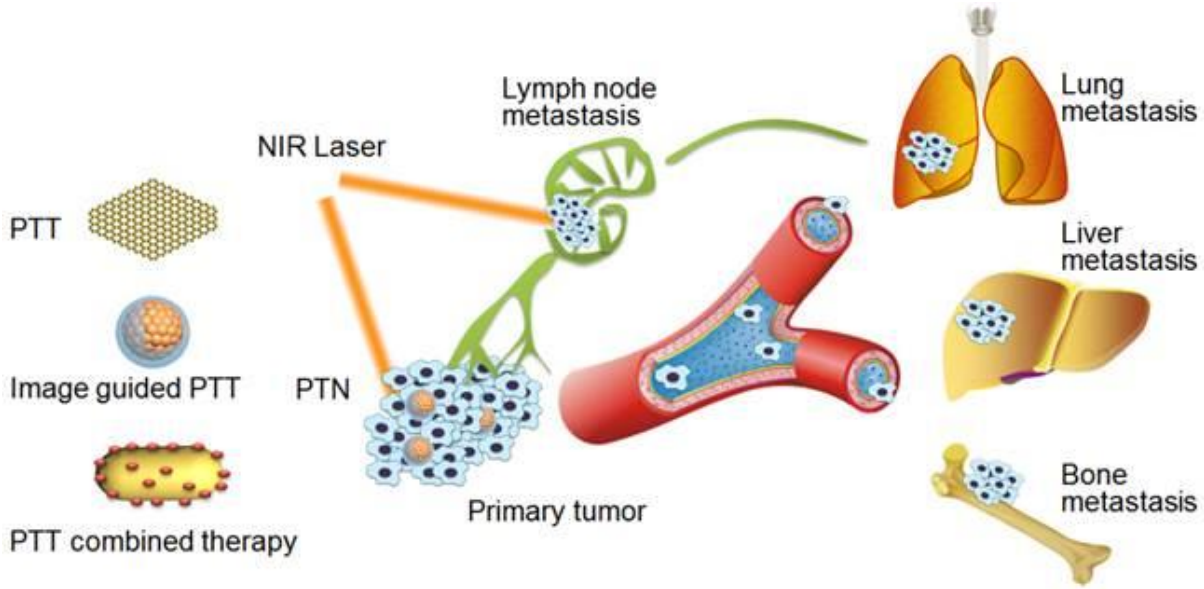

Fig 1.13: The schematic illustration of photothermal therapy of cancer metastasis with various photothermal nanomaterials. Reprinted with permission from [29].

Gold nanoparticles have remained the foremost choice of PA agents due to their biocompatibility and shape tuneability to produce NIR active nanomaterials. By modifying the shell thickness and core diameter, gold nanoshells (GNS) can be made to absorb in the NIR spectrum making them highly suitable for phothermal therapy mediated cancer therapeutics[31]. PEG-coated silica-gold nanoshells (AuroShell ®) have been employed by AuroLase ® (Nanospectra Biosciences) for NIR-facilitated thermal ablation and has been under clinical trials for treatment of solid primary and/or metastatic lung tumors (NCT01679470) as well as for refractory and/or recurrent tumors of the head and neck (NCT00848042) [32]. Gold nanorods (GNRs) with absorption in NIR for deeper tissue penetration were effectively used for treating metastasis in the proper axillary lymph nodes and could be potentially used as an alternative to lymph node dissection [33]. Likewise, aptamer conjugated gold nanorods have been utilised for effectively targeting and killing of both prostate cancer cells and their subpopulation of cancer stem cells by NIR laser irradiation, thereby providing a theranostic approach for early diagnosis and targeted therapy of prostate cancer [34]. Other gold anisotropic nanostructures such as gold nanostars have gained immense popularity due to their enhanced NIR-absorbing capability [35]. Multifunctional gold nanostar conjugates have been utilized for multimodal imaging and combinatorial chemo-photothermal cancer theranostics [36]–[38]. Relatively newer anisotropic structures such as gold nanoflowers have emerged as photoactive agents for photothermal therapy of cancer depicting superior photothermal transduction efficiency over GNRs and GNS alongwith drug loading

capacity and pH/NIR dual-responsive drug delivery performance[39]. This has enabled their use for synergistic chemo-photothermal cancer therapy as well as multimodal imaging guided cancer theranostics [39]–[41].

There have been reports wherein the sub-lethal hyperthermia may promote epithelial to mesenchymal like transition of breast cancer cells and the residual surviving cells may lead to tumor relapse [42]. Moreover, the heterogeneous distribution of PA in tumor and limitation of penetration depth with NIR laser in deep-seated tumors may not cause complete eradication of tumor cells. Hence, PTT is often accompanied by other combinatorial therapies such as chemotherapy [43], surgery [29], radiotherapy [44], and immunotherapy [45] along with imaging agents [46] to exert a synergistic affect and completely eradicate both tumor cells as well as metastatic cells and present as promising combinatorial theranostic strategies for efficacious cancer metastasis treatment.

1.5.2 Cancer Radiosensitization by Gold Quantum Clusters

Radiation therapy (RT) is often used as palliative strategy post-surgery in a clinical setup to reduce the risk of cancer relapse. It uses high energy ionizing radiation such as ɤ-rays or X-rays that cause DNA damage leading to shrinking and killing of tumor cells. However, there are certain limitations around RT such as non-specific targeting, damage to normal/healthy surrounding tissues, resistance of tumor cells, and requirement of high radiation dosage as a standalone therapeutic technique that poses a serious challenge in radiation oncology. Hence, the focus on developing novel nano- radiosensitizers has emerged to enhance the use of RT in clinical settings. Au QCs have been vastly studied for their role as radio sensitizers due to following advantages,

- High atomic number (Z=79) of Au enables it to absorb radiation and emit secondary electrons more efficiently
- Ability of secondary electrons emitted to interact with aqueous environment and produce reactive oxygen species (ROS) thereby causing DNA damage and increasing efficacy of RT
- Increased possibility of renal clearance due to its ultrasmall size
- High biocompatibility
- Multifunctionality of ligand for better and targeted uptake
- Better pharmacokinetic properties
- Photoluminescent QCs provide combinatorial theranostic properties

- Mass attenuation coefficient of gold is 100 times higher than any soft tissue.

Zhang *et. al* first demonstrated ultrasmall glutathione (GSH) stabilised Au_{10-12} $(SG)_{10-12}$ with increased tumor uptake, targeting specificity via the improved EPR effect and high renal clearance as effective radiosensitizers in U14 tumor bearing nude mice model [47]. Similarly, sub 2-nm GSH stabilised Au_{25}QCs also depicted preferential tumor uptake and efficient renal clearance minimizing any side-effects due to accumulation in the body [48]. Albumin stabilised Au_{25}QCs conjugated to AS1411 aptamer have been utilised as targeted cancer radiosensitizer for highly selective treatment in 4T1 tumor bearing breast cancer mice model with increased survival rate [49]. Histidine stabilised AuQC have also been utilised for enhanced RT by synergistically utilising Au for local radiation enhancement along with decreasing the intracellular GSH level [50]. The intracellular GSH depletion effectively enabled to prevent their consumption of ROS generated and increased their anti-cancer effect by arresting the cells at the radiosensitive G2/M phase [50]. Cyclic RGD peptide stabilized AuQCs have been employed for their dual role as radiosensitizers as well as fluorescent imaging of cancer cells for tumour targeted therapeutics [51]. These red/NIR emissive RGD @AuQCs targeted the αvβ3 integrin-positive cancer cells and accumulated preferentially in the tumor site making them highly potent cancer tumor targeted radiosensitizers. Atomically precise levonorgestrel stabilised Au_8QCs have been reported to act as highly enhanced radiosensitisers with very high red photoluminescence (QY~ 58.7%) [52]. Upon X-ray irradiation, these Au_8NCs produced ROS resulting in irreversible apoptosis *in-vitro* and significantly supressed their tumorigenicity (~74.2%) with single radiation dose of 4Gy *in-vivo*. Highly specific prostate-specific membrane antigen targeting peptide ligand i.e. CY-PSMA-1 stabilised Au_{25}QCs have been utilised for highly targeted radiotherapy of prostate tumors with high renal clearance as compared to 5nm PSMA-targeted gold nanoparticles [53]. PSMA-expressing PC3pip cells and PSMA-negative PC3flu cells implanted on the flanks of the same mouse resulted in higher targeting levels to the PC3pip tumor than to the PC3flu tumor as depicted in the **Fig 1.14**.

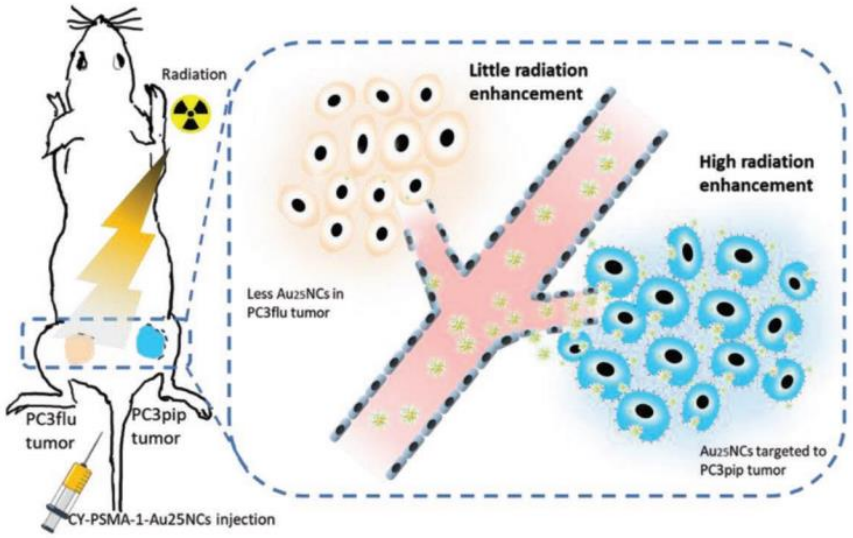

Fig 1.14: Illustration depicting higher affinity of CY-PSMA-1-Au_{25} QCs towards PSMA-expressing PC3pip over PSMA-negative PC3flu implanted on different flanks of the same mouse for tumor targeting and enhanced radiation therapy. Reprinted with permission from [53].

1.6 Antibacterial activity of silver based nanoparticles

The efforts in combating bacterial infections with nanomedicine has been on a tremendous rise especially with the emergence of antibiotic resistant bacteria and in particular, the emergence of multidrug-resistant (MDR) superbugs. This has occurred over time as a natural evolution process in bacteria in the course of antibiotic treatment [54]. Hence, the identification of new antimicrobial targets and/or chemical entities as antimicrobial drugs is in great demand. In this context, researchers have developed many novel approaches like designing antibiotic adjuvants such as β-lactamase inhibitors and drugs targeting biofilm [55]. However, the identification and discovery of novel medicinal targets and strategies is a long and challenging journey. In this context, the role of silver nanomaterials as antibacterial agents cannot be undermined due to their following beneficial properties:

i) Silver (Ag and Ag^+) is a known broad spectrum antibiotic having intrinsic antiseptic, antimicrobial, anti-inflammatory, and wound healing properties [54]
ii) Ability of Ag^+ to interact with bacterial membrane proteins and block respiratory chains [56], [57]
iii) Ag^+ interacts with nucleophilic amino acid residues in bacterial proteins, thereby Ag-S bonds [58], [59]
iv) Interaction of silver ions with both DNA and proteins and subsequent ROS production [60]

Noble metal QCs (especially: Ag, Au) along with Cu, and alloy QCs have been explored widely in the past decade for their antibacterial theranostic effect owing to their low toxicity, ultra-small size, high surface area, ease of surface functionalization, broad-spectrum antimicrobial activity, and low bacterial resistance development. It has been reported that Au nanoparticles are biologically inert to bacteria whereas ultra-small nanocluster exhibit notable wide-spectrum antibacterial activity [61]. Hence, antimicrobial property can be attributed to their size that AuQCs are in general, can interact better with bacteria, induce a metabolic imbalance post internalization leading to ROS generation and subsequently kill bacterial cells as depicted in **Fig 1.15**. Apart from size, various other factors come into play for attributing to the antibacterial effect of metal QCs. One such important factor is the elemental composition of the QCs. Cu and Ag QCs have shown to exhibit superior antibacterial effect as compared to Au due to their inherent antibacterial ability. Moreover, alloying also enhances the antibacterial effect of metal QCs over a single metal composition depending upon the ratio of metals [62], [63]. For example, QC alloy of Au & Pt display highly potent antibacterial activity over their single elemental non-antibacterial Pt QC and Au QC counterparts [64].

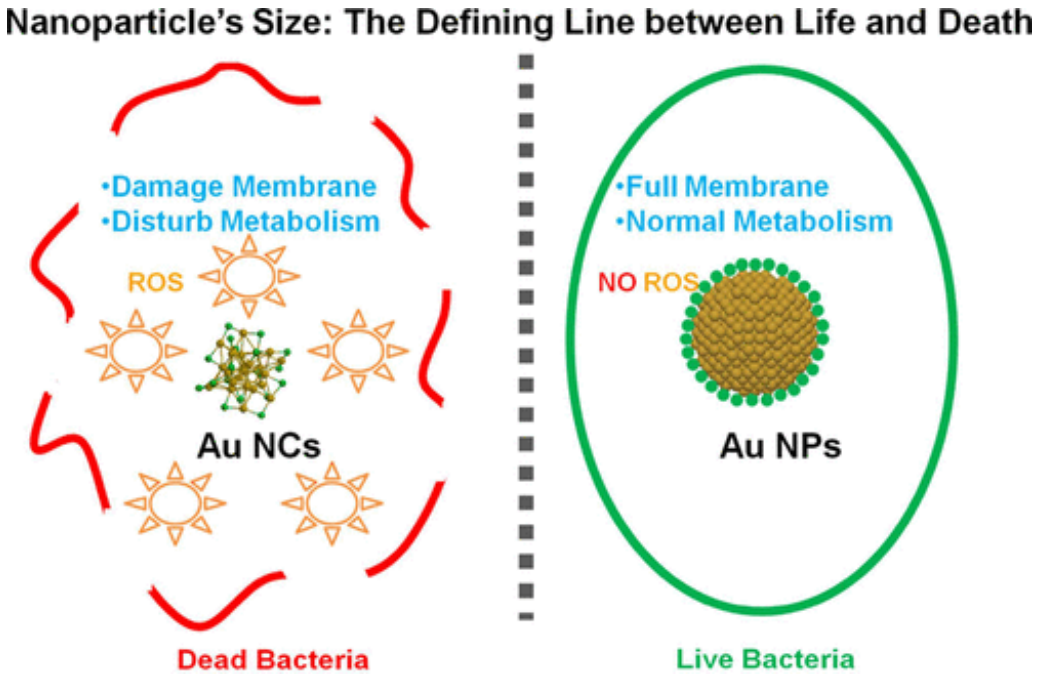

Fig 1.15: Schematic illustration of the size regulation of AuQCs to significantly affect their antibacterial properties. Reprinted with permission from [61].

The surface chemistry of the QCs also play an essential role in deciding the potential of QCs and therefore, the surface ligands can be modulated to enhance the antibacterial functionality of QCs. For example, it has been reported that amongst the 4 types of Au QCs modified by

mercaptopyrimidine analogs with similar structures, the amino-rich ligands AuQCs exhibited stronger antibacterial activity on superbug Methicillin–resistant *Staphylococcus aureus* (MRSA) in both macrophages and animal infection models.

Metal QCs have reportedly caused bacterial inhibition through several mechanisms including:

- Cell membrane damage [61], [65]
- ROS generation [61], [65]–[67]
- Photo-inactivation by metal QCs [68], [69]
- Release of metal ions (Ag^+), [66], [67]
- Damage to other intracellular components (DNA, proteins, mitochondria) [65], [70]
- Delivery of therapeutic/ antibacterial agents such as for their effective synergistic action for QC based nano-antibiotics [71], [72]

Moreover, the overall ligand charge on the shell structure stabilising the metallic core in the QCs also affect the interaction, subsequent internalisation in bacteria and ultimately marks their antibacterial activity. Cationic metal QCs have been known to favourably increase their bacterial internalisation due to their electrostatically favoured interaction with the negatively charged bacterial surface [73][74]. Cationic AuQCs have been reported to induce higher intracellular ROS production due to better interaction thereby leading to enhanced antibacterial activity [75]. Ligand density on the QC is also a key factor leading to altered antibacterial activity and hence can be used to rationally design QCs by tuning the ligand to metal ratio [76]. Additionally, the oxidation state of metals in the QCs have an effect on their antimicrobial property. For example, it has been reported that GSH protected AgQCs with higher Ag^+ content despite having the same size and surface ligand, exhibit a stronger antimicrobial activity towards both Gram-negative and Gram-positive bacteria due to Ag^+ release induced ROS mediated antibacterial activity [67].

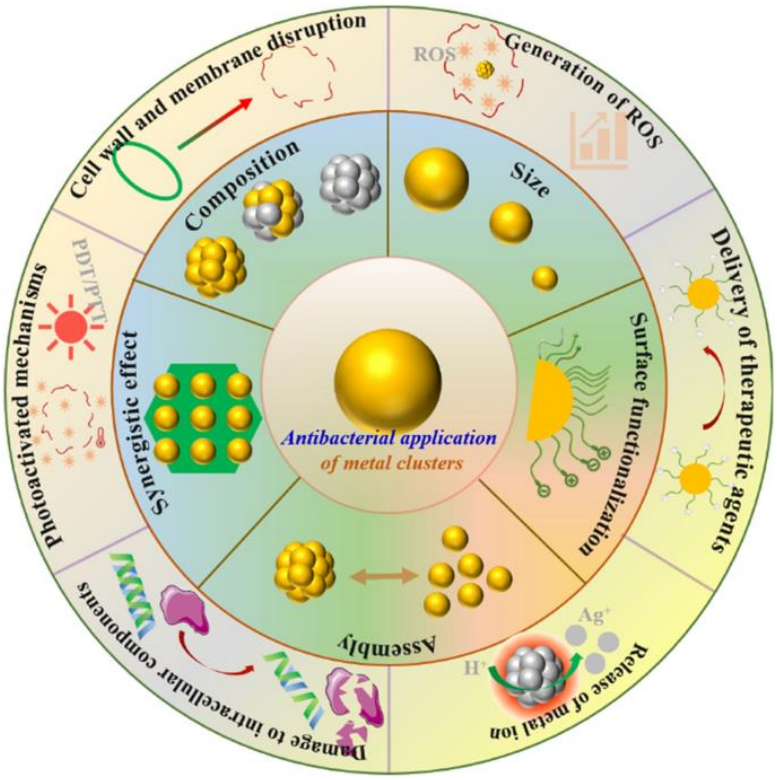

Fig 1.16: Summarising key physicochemical properties of metal QCs governing their antibacterial activity and different mechanisms of QCs based antibacterial activity. Reprinted with permission from [77].

1.7 Personalised Nanomedicine

Personalized nanomedicine is an emerging field that combines the principles of nanotechnology with personalized medicine in order to provide a very sensitive diagnosis and targeted treatment of diseases. It includes designing a defined healthcare strategy aiming to develop specialized theranostics for individual patient or a cohort of patients taking into account their genetic, phenotypic, and environmental factors that could influence the efficacy and safety of the therapy. Certain key aspects of personalized nanomedicine include:

i. **Targeted drug delivery**: Customized therapeutic agents for on-site delivery thereby minimizing the side-effects on normal tissues and reducing the effective dosage required for therapeutic action.

ii. **Diagnostic and imaging agents:** Engineering of nanomaterials so as to help in early disease detection and monitoring the progression of diseases, allowing for timely intervention.

iii. **Biomarker Identification:** Analysing biomarkers specific to an individual and designing tailor-made treatment approaches based on individual response rather than waste the time in trial and eliminate method.

iv. **Theranostics**: Designing nanoparticles that can provide both treatment and monitoring of disease progression to provide real-time adjustment of treatment plans as a patient's condition changes.

v. **Personalized Cancer Treatments:** Involves tailoring cancer treatments based on a patient's genetic profile, tumor characteristics, and treatment response thereby providing a more effective and less toxic cancer therapy.

vi. **Drug Resistance Mitigation**: Antibiotic or drug resistance issue can be effectively resolved by adapting the treatment response as a patient's disease evolves. Nanoparticles can be designed to deliver a combination of drugs or overcome resistance mechanisms that develop over time.

vii. **Immunotherapy Enhancement:** To enhance the effectiveness of immunotherapies, such as checkpoint inhibitors and CAR-T cell therapy. Nanoparticles can be engineered to target immune cells, modulate the immune response, and improve the overall success of immunotherapeutic approaches.

viii. **Tailored Dosage and Release:** Nanoscale drug delivery systems can be designed to release drugs at specific rates and in response to certain triggers, ensuring that patients receive the right dosage at the right time for their specific condition.

ix. **Patient-specific Monitorin**g: Nanosensors and nanodevices can be used for continuous monitoring of a patient's health, allowing for early intervention and treatment adjustments as needed.

While personalized nanomedicine holds great promise for improving the effectiveness and safety of medical treatments, it also presents challenges related to regulatory approval, cost, and scalability. However, as technology and research in this field advance, we can expect to see more personalized and targeted therapies in healthcare.

1.7.1 Host-specific protein nanomaterials for theranostic applications

Nanoparticles when administered into a host, the biomolecules or proteins in the physiological environment, including blood and peritoneum, form a dynamic coating known as ‘Protein corona’ on the NP surface. This protein corona (PC) has been found to be dependent on various factors such as type of nanomaterial (in terms of shape, size or charge) as well as different physiological conditions (such as temperature, protein source or type of disease present).

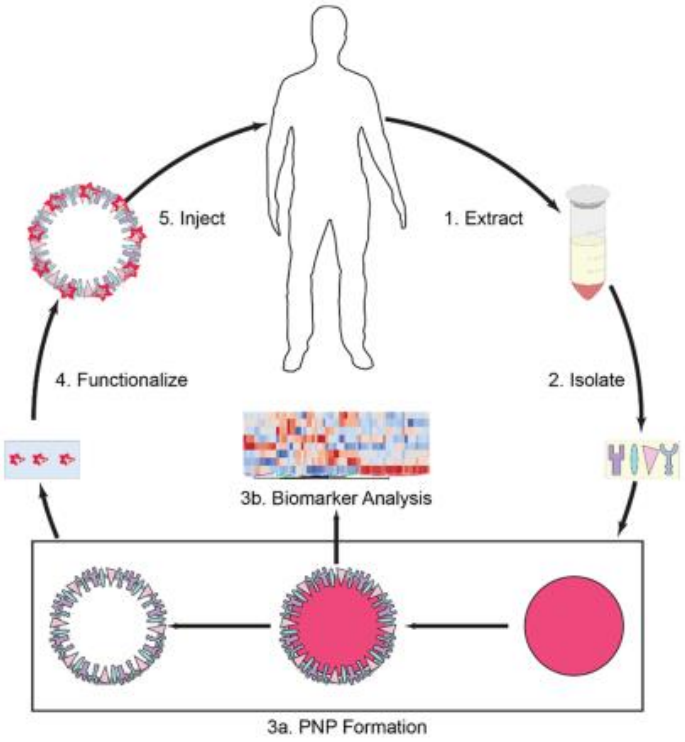

Fig 1.17: Schematic illustration depicting integration of host-specific protein nanomaterials into a clinical setting. Envisioned by Lazarovits et al. and reprinted with permission from [80].

For instance, it has been reported that the human plasma proteins from different medical conditions such as breast cancer, diabetes, hypercholesterolemia, rheumatism, fauvism, smoking, hemodialysis, thalassemia, hemophilia A and B, pregnancy, common cold and hypofibrinogenemia have a differential protein composition based on the PC formed by each of them on both hydrophobic and hydrophilic nanoparticles [78]. Moreover, the protein composition or abundance may be different even in a healthy individual based on their age, gender, lifestyle, geographical conditions or habits [79]. All these factors taken in account can induce the formation of different protein corona on the same nanomaterial and brings in the concept of host-specific nanomaterials wherein each individual whether healthy or diseased has a unique plasma proteome fingerprint and hence forms a host-specific personalised protein corona (PPC) which is the characteristic of an individual. This PPC is of high relevance in a clinical setup wherein it can be used to rationally design a plan of treatment for each individual. Lazarovits *et al.* demonstrated that personalised protein nanoparticles (PNPs) made entirely from host-specific human plasma proteins into different sizes and shapes using template gold nanoparticles had unique molecular fingerprints [80]. These PNPs were found to be highly biodegradable, non-immunogenic (adaptive and innate immune response) for acute and sub-acute dosage and could be actively utilised for protein-cargo delivery *in-vivo* as envisioned in

Fig 1.17. Hence, designing a new class of personalised protein nanomaterials would not only increase the bioavailability of the therapeutic dosage but also mitigate the concerns surrounding their toxicity, inflammation, and immune activation, which are major cause of treatment failure. Moreover, the PPC formation on $Gd@C_{82}(OH)_{22}$ nanoparticles was utilised by Ren *et.al* to investigate the presence of specific biomarkers present in ten human lung squamous cell carcinoma patients based on their natural protein fingerprinting of the PPC formed [81]. It was revealed that complement component C1q bound to these nanoparticles was altered in secondary structure and led to the activation of innate immune response, which could be utilised strategically for designing precision cancer immune therapeutics.

Hence, host specific PPC is of high relevance in a clinical setup wherein it can be used to identify biomarkers acting as diagnostic tools and subsequently for rationally designing a personalised therapeutic strategy for each individual.

1.7.2 Objectives of the thesis

The overall aim of the thesis is to develop novel nanomaterials for various therapeutic applications and analyse their preclinical safety and bio distribution profiles. The specific objectives of the thesis are:

1. Development of a rapid *in-situ* synthetic procedure for Colloidal Gold Semi Shells using MOF (Metal Organic Framework) as sacrificial template and assessment of their Photothermal Transduction Ability.
2. Preclinical safety assessement of Gold Semi Shells and their efficacy in photothermal therapy mediated tumor regression in metastatic breast cancer murine model.
3. Development and preclinical safety assessment of Host-Specific Gold Quantum Clusters stabilized with autologous serum proteins for Cancer Radiosensitization
4. Development and preclinical safety assessment of Host-Specific Silver Quantum Clusters stabilized with autologous serum proteins for Antibacterial Applications.

References:

[1] D. Pal, C. K. Sahu, and A. Haldar, "Bhasma : The ancient Indian nanomedicine.," *J. Adv. Pharm. Technol. Res.*, vol. 5, no. 1, pp. 4–12, Jan. 2014.

[2] T. Gunasekaran, T. Nigusse, and M. D. Dhanaraju, "Silver nanoparticles as real topical bullets for wound healing.," *J. Am. Coll. Clin. Wound Spec.*, vol. 3, no. 4, pp. 82–96, Dec. 2011.

[3] K. A. Willets and R. P. Van Duyne, "Localized Surface Plasmon Resonance Spectroscopy and Sensing," *Annu. Rev. Phys. Chem.*, vol. 58, no. 1, pp. 267–297, Apr. 2007.

[4] S. Lal, S. Link, and N. J. Halas, “Nano-optics from sensing to waveguiding,” *Nat. Photonics*, vol. 1, no. 11, pp. 641–648, 2007.

[5] E. Prodan, C. Radloff, N. J. Halas, and P. Nordlander, “A Hybridization Model for the Plasmon Response of Complex Nanostructures,” *Science (80-.).*, vol. 302, no. 5644, pp. 419–422, Oct. 2003.

[6] P. Van Dorpe and J. Ye, “Semishells: Versatile Plasmonic Nanoparticles,” *ACS Nano*, vol. 5, no. 9, pp. 6774–6778, Sep. 2011.

[7] J. Ye, L. Lagae, G. Maes, G. Borghs, and P. Van Dorpe, “Symmetry breaking induced optical properties of gold open shell nanostructures,” *Opt. Express*, vol. 17, no. 26, pp. 23765–23771, 2009.

[8] N. A. Mirin and N. J. Halas, “Light-Bending Nanoparticles,” *Nano Lett.*, vol. 9, no. 3, pp. 1255–1259, Mar. 2009.

[9] Y. Zhang, A. Barhoumi, J. B. Lassiter, and N. J. Halas, “Orientation-Preserving Transfer and Directional Light Scattering from Individual Light-Bending Nanoparticles,” *Nano Lett.*, vol. 11, no. 4, pp. 1838–1844, Apr. 2011.

[10] J. Ye and P. Van Dorpe, “Optical Properties of Metallic Semishells: Breaking the Symmetry of Plasmonic Nanoshells BT - UV-VIS and Photoluminescence Spectroscopy for Nanomaterials Characterization,” C. Kumar, Ed. Berlin, Heidelberg: Springer Berlin Heidelberg, 2013, pp. 75–98.

[11] J. Ye, P. Van Dorpe, W. Van Roy, G. Borghs, and G. Maes, “Fabrication, Characterization, and Optical Properties of Gold Nanobowl Submonolayer Structures,” *Langmuir*, vol. 25, no. 3, pp. 1822–1827, Feb. 2009.

[12] J. Ye, C. Chen, L. Lagae, G. Maes, G. Borghs, and P. Van Dorpe, “Strong location dependent surface enhanced Raman scattering on individual gold semishell and nanobowl particles,” *Phys. Chem. Chem. Phys.*, vol. 12, no. 37, pp. 11222–11224, 2010.

[13] J. B. Lassiter, M. W. Knight, N. A. Mirin, and N. J. Halas, “Reshaping the Plasmonic Properties of an Individual Nanoparticle,” *Nano Lett.*, vol. 9, no. 12, pp. 4326–4332, Dec. 2009.

[14] J. C. Love, B. D. Gates, D. B. Wolfe, K. E. Paul, and G. M. Whitesides, “Fabrication and Wetting Properties of Metallic Half-Shells with Submicron Diameters,” *Nano Lett.*, vol. 2, no. 8, pp. 891–894, Aug. 2002.

[15] J. Liu, K. E. McBean, N. Harris, and M. B. Cortie, “Optical properties of suspensions of gold half-shells,” *Mater. Sci. Eng. B*, vol. 140, no. 3, pp. 195–198, 2007.

[16] J. Ye *et al.*, “Plasmonic Modes of Metallic Semishells in a Polymer Film,” *ACS Nano*, vol. 4, no. 3, pp. 1457–1464, Mar. 2010.

[17] D. Rodríguez-Fernández, J. Pérez-Juste, I. Pastoriza-Santos, and L. M. Liz-Marzán, “Colloidal Synthesis of Gold Semishells,” *ChemistryOpen*, vol. 1, no. 2, pp. 90–95, Apr. 2012.

[18] D. Mann *et al.*, “Protecting patches in colloidal synthesis of Au semishells,” *Chem. Commun.*, vol. 53, no. 27, pp. 3898–3901, 2017.

[19] Y. Ridelman, G. Singh, R. Popovitz-Biro, S. G. Wolf, S. Das, and R. Klajn, “Metallic Nanobowls by Galvanic Replacement Reaction on Heterodimeric Nanoparticles,” *Small*, vol. 8, no. 5, pp. 654–660, Mar. 2012.

[20] L. Chen, C. P. Deming, Y. Peng, P. Hu, J. Stofan, and S. Chen, “Gold core@silver semishell Janus nanoparticles prepared by interfacial etching,” *Nanoscale*, vol. 8, no. 30, pp. 14565–14572, 2016.

[21] R. Jiang *et al.*, “Colloidal Gold Nanocups with Orientation-Dependent Plasmonic Properties,” *Adv. Mater.*, vol. 28, no. 30, pp. 6322–6331, Aug. 2016.

[22] J. Sun and Y. Jin, “Fluorescent Au nanoclusters: recent progress and sensing applications,” *J. Mater. Chem. C*, vol. 2, no. 38, pp. 8000–8011, 2014.

[23] C. J. Lin *et al.*, “Review : Synthesis of Fluorescent Metallic Nanoclusters toward Biomedical Application : Recent Progress and Present Challenges,” vol. 29, no. 6, pp. 276–283.

[24] S. H. Hassanpour and M. Dehghani, “Review of cancer from perspective of molecular,” *J. Cancer Res. Pract.*, vol. 4, no. 4, pp. 127–129, 2017.

[25] “Cancer Statistics,” 2020. .

[26] T. N. Seyfried and L. C. Huysentruyt, “On the origin of cancer metastasis.,” *Crit. Rev. Oncog.*, vol. 18, no. 1–2, pp. 43–73, 2013.

[27] E. Pérez-Herrero and A. Fernández-Medarde, “Advanced targeted therapies in cancer: Drug nanocarriers, the future of chemotherapy.,” *Eur. J. Pharm. Biopharm. Off. J. Arbeitsgemeinschaft fur Pharm. Verfahrenstechnik e.V*, vol. 93, pp. 52–79, Jun. 2015.

[28] H. S. Han and K. Y. Choi, “Advances in Nanomaterial-Mediated Photothermal Cancer Therapies: Toward Clinical Applications,” *Biomedicines*, vol. 9, no. 3, 2021.

[29] L. Zou *et al.*, “Current Approaches of Photothermal Therapy in Treating Cancer Metastasis with Nanotherapeutics,” *Theranostics*, vol. 6, pp. 762–772, 2016.

[30] R. Zhu, T. Lang, Q. Yin, and Y. Li, “Nano drug delivery systems improve metastatic breast cancer therapy.,” *Med. Rev. (Berlin, Ger.*, vol. 1, no. 2, pp. 244–274, Dec. 2021.

[31] L. R. Hirsch *et al.*, “Nanoshell-mediated near-infrared thermal therapy of tumors under magnetic resonance guidance.,” *Proc. Natl. Acad. Sci. U. S. A.*, vol. 100, no. 23, pp. 13549–13554, Nov. 2003.

[32] “clinicaltrials.gov.”

[33] T. Okuno *et al.*, “Photothermal therapy of tumors in lymph nodes using gold nanorods and near-infrared laser light,” *J. Control. Release*, vol. 172, no. 3, pp. 879–884, 2013.

[34] J. Wang *et al.*, “Aptamer-Conjugated Nanorods for Targeted Photothermal Therapy of Prostate Cancer Stem Cells,” *Chem. – An Asian J.*, vol. 8, no. 10, pp. 2417–2422, Oct. 2013.

[35] W.-H. Chen *et al.*, “Rational Design of Multifunctional Gold Nanoparticles via Host–Guest Interaction for Cancer-Targeted Therapy,” *ACS Appl. Mater. Interfaces*, vol. 7, no. 31, pp. 17171–17180, Aug. 2015.

[36] H. Chen *et al.*, “Multifunctional Gold Nanostar Conjugates for Tumor Imaging and

Combined Photothermal and Chemo-therapy," *Theranostics*, vol. 3, pp. 633–649, 2013.

[37] Y. Gao *et al.*, "Multifunctional gold nanostar-based nanocomposite: Synthesis and application for noninvasive MR-SERS imaging-guided photothermal ablation," *Biomaterials*, vol. 60, pp. 31–41, 2015.

[38] M. Li, L. Li, C. Zhan, and D. S. Kohane, "Core-Shell Nanostars for Multimodal Therapy and Imaging," *Theranostics*, vol. 6, no. 13, pp. 2306–2313, 2016.

[39] S. Li, L. Zhang, T. Wang, L. Li, C. Wang, and Z. Su, "The facile synthesis of hollow Au nanoflowers for synergistic chemo-photothermal cancer therapy," *Chem. Commun.*, vol. 51, no. 76, pp. 14338–14341, 2015.

[40] T. Yin *et al.*, "Self-assembly synthesis of vapreotide-gold hybrid nanoflower for photothermal antitumor activity," *Mater. Sci. Eng. C*, vol. 93, pp. 716–723, 2018.

[41] S. Lu, X. Li, J. Zhang, C. Peng, M. Shen, and X. Shi, "Dendrimer-Stabilized Gold Nanoflowers Embedded with Ultrasmall Iron Oxide Nanoparticles for Multimode Imaging–Guided Combination Therapy of Tumors," *Adv. Sci.*, vol. 5, no. 12, p. 1801612, Dec. 2018.

[42] T. H. Lee, J. Bu, B. H. Kim, M. J. Poellmann, S. Hong, and S. H. Hyun, "Sub-lethal hyperthermia promotes epithelial-to-mesenchymal-like transition of breast cancer cells: implication of the synergy between hyperthermia and chemotherapy," *RSC Adv.*, vol. 9, no. 1, pp. 52–57, 2019.

[43] J. Liao *et al.*, "Combined Cancer Photothermal-Chemotherapy Based on Doxorubicin/Gold Nanorod-Loaded Polymersomes," *Theranostics*, vol. 5, pp. 345–356, 2015.

[44] X. Yi *et al.*, "Imaging-Guided Combined Photothermal and Radiotherapy to Treat Subcutaneous and Metastatic Tumors Using Iodine-131-Doped Copper Sulfide Nanoparticles," *Adv. Funct. Mater.*, vol. 25, no. 29, pp. 4689–4699, Aug. 2015.

[45] L. Guo *et al.*, "Combinatorial Photothermal and Immuno Cancer Therapy Using Chitosan-Coated Hollow Copper Sulfide Nanoparticles," *ACS Nano*, vol. 8, no. 6, pp. 5670–5681, Jun. 2014.

[46] H. Deng *et al.*, "Theranostic Self-Assembly Structure of Gold Nanoparticles for NIR Photothermal Therapy and X-Ray Computed Tomography Imaging," *Theranostics*, vol. 4, pp. 904–918, 2014.

[47] X.-D. Zhang *et al.*, "Ultrasmall Au10−12(SG)10−12 Nanomolecules for High Tumor Specificity and Cancer Radiotherapy," *Adv. Mater.*, vol. 26, no. 26, pp. 4565–4568, Jul. 2014.

[48] X.-D. Zhang *et al.*, "Enhanced Tumor Accumulation of Sub-2 nm Gold Nanoclusters for Cancer Radiation Therapy," *Adv. Healthc. Mater.*, vol. 3, no. 1, pp. 133–141, Jan. 2014.

[49] F. Ghahremani, A. Kefayat, D. Shahbazi-Gahrouei, H. Motaghi, M. A. Mehrgardi, and S. Haghjooy-Javanmard, "AS1411 aptamer-targeted gold nanoclusters effect on the enhancement of radiation therapy efficacy in breast tumor-bearing mice," *Nanomedicine*, vol. 13, no. 20, pp. 2563–2578, Oct. 2018.

[50] X. Zhang *et al.*, “Glutathione-Depleting Gold Nanoclusters for Enhanced Cancer Radiotherapy through Synergistic External and Internal Regulations,” *ACS Appl. Mater. Interfaces*, vol. 10, no. 13, pp. 10601–10606, Apr. 2018.

[51] G. Liang, X. Jin, S. Zhang, and D. Xing, “RGD peptide-modified fluorescent gold nanoclusters as highly efficient tumor-targeted radiotherapy sensitizers,” *Biomaterials*, vol. 144, pp. 95–104, 2017.

[52] T.-T. Jia *et al.*, “Atomically Precise Gold–Levonorgestrel Nanocluster as a Radiosensitizer for Enhanced Cancer Therapy,” *ACS Nano*, vol. 13, no. 7, pp. 8320–8328, Jul. 2019.

[53] D. Luo, X. Wang, S. Zeng, G. Ramamurthy, C. Burda, and J. P. Basilion, “Targeted Gold Nanocluster-Enhanced Radiotherapy of Prostate Cancer,” *Small*, vol. 15, no. 34, p. 1900968, Aug. 2019.

[54] M. Konop, T. Damps, A. Misicka, and L. Rudnicka, “Certain Aspects of Silver and Silver Nanoparticles in Wound Care: A Minireview,” *J. Nanomater.*, vol. 2016, p. 7614753, 2016.

[55] G. Annunziato, “Strategies to Overcome Antimicrobial Resistance (AMR) Making Use of Non-Essential Target Inhibitors: A Review.,” *Int. J. Mol. Sci.*, vol. 20, no. 23, Nov. 2019.

[56] I. Sondi and B. Salopek-Sondi, “Silver nanoparticles as antimicrobial agent: a case study on E. coli as a model for Gram-negative bacteria,” *J. Colloid Interface Sci.*, vol. 275, no. 1, pp. 177–182, 2004.

[57] J. R. Morones *et al.*, “The bactericidal effect of silver nanoparticles,” *Nanotechnology*, vol. 16, no. 10, p. 2346, 2005.

[58] A. D. Russell and W. B. Hugo, “7 Antimicrobial Activity and Action of Silver,” vol. 31, G. P. Ellis and D. K. B. T.-P. in M. C. Luscombe, Eds. Elsevier, 1994, pp. 351–370.

[59] Q. L. Feng, J. Wu, G. Q. Chen, F. Z. Cui, T. N. Kim, and J. O. Kim, “A mechanistic study of the antibacterial effect of silver ions on Escherichia coli and Staphylococcus aureus,” *J. Biomed. Mater. Res.*, vol. 52, no. 4, pp. 662–668, Dec. 2000.

[60] K. Mijnendonckx, N. Leys, J. Mahillon, S. Silver, and R. Van Houdt, “Antimicrobial silver: uses, toxicity and potential for resistance,” *BioMetals*, vol. 26, no. 4, pp. 609–621, 2013.

[61] K. Zheng, M. I. Setyawati, D. T. Leong, and J. Xie, “Antimicrobial Gold Nanoclusters,” *ACS Nano*, vol. 11, no. 7, pp. 6904–6910, Jul. 2017.

[62] X. Kang, Y. Li, M. Zhu, and R. Jin, “Atomically precise alloy nanoclusters: syntheses{,} structures{,} and properties,” *Chem. Soc. Rev.*, vol. 49, no. 17, pp. 6443–6514, 2020.

[63] Y. Zhang, Z. Shao, W. Yuan, H. Xu, X. You, and X. Liao, “Green and rapid synthesis of cysteine-directed novel AgCu nanocluster hydrogel with good antibacterial activity,” *Materialia*, vol. 20, p. 101232, 2021.

[64] Y. Zhao, C. Ye, W. Liu, R. Chen, and X. Jiang, “Tuning the Composition of AuPt Bimetallic Nanoparticles for Antibacterial Application,” *Angew. Chemie Int. Ed.*, vol.

53, no. 31, pp. 8127–8131, Jul. 2014.

[65] Y. Zheng, W. Liu, Z. Qin, Y. Chen, H. Jiang, and X. Wang, “Mercaptopyrimidine-Conjugated Gold Nanoclusters as Nanoantibiotics for Combating Multidrug-Resistant Superbugs,” *Bioconjug. Chem.*, vol. 29, no. 9, pp. 3094–3103, Sep. 2018.

[66] X. Yuan, M. I. Setyawati, A. S. Tan, C. N. Ong, D. T. Leong, and J. Xie, “Highly luminescent silver nanoclusters with tunable emissions: cyclic reduction–decomposition synthesis and antimicrobial properties,” *NPG Asia Mater.*, vol. 5, no. 2, pp. e39–e39, 2013.

[67] X. Yuan, M. I. Setyawati, D. T. Leong, and J. Xie, “Ultrasmall Ag+-rich nanoclusters as highly efficient nanoreservoirs for bacterial killing,” *Nano Res.*, vol. 7, no. 3, pp. 301–307, 2014.

[68] Y. Xie, W. Zheng, and X. Jiang, “Near-Infrared Light-Activated Phototherapy by Gold Nanoclusters for Dispersing Biofilms,” *ACS Appl. Mater. Interfaces*, vol. 12, no. 8, pp. 9041–9049, Feb. 2020.

[69] G. B. Hwang *et al.*, “Continuous Single-Phase Synthesis of [Au25(Cys)18] Nanoclusters and their Photobactericidal Enhancement,” *ACS Appl. Mater. Interfaces*, vol. 12, no. 43, pp. 49021–49029, Oct. 2020.

[70] Y. Wang *et al.*, “Antibacterial mechanism and transcriptome analysis of ultra-small gold nanoclusters as an alternative of harmful antibiotics against Gram-negative bacteria,” *J. Hazard. Mater.*, vol. 416, p. 126236, 2021.

[71] Q. Li *et al.*, “Design and mechanistic study of a novel gold nanocluster-based drug delivery system,” *Nanoscale*, vol. 10, no. 21, pp. 10166–10172, 2018.

[72] S. Kalita, R. Kandimalla, A. C. Bhowal, J. Kotoky, and S. Kundu, “Functionalization of β-lactam antibiotic on lysozyme capped gold nanoclusters retrogress MRSA and its persisters following awakening,” *Sci. Rep.*, vol. 8, no. 1, p. 5778, 2018.

[73] D. Pranantyo, P. Liu, W. Zhong, E.-T. Kang, and M. B. Chan-Park, “Antimicrobial Peptide-Reduced Gold Nanoclusters with Charge-Reversal Moieties for Bacterial Targeting and Imaging,” *Biomacromolecules*, vol. 20, no. 8, pp. 2922–2933, Aug. 2019.

[74] Y. Xie *et al.*, “Gold Nanoclusters for Targeting Methicillin-Resistant Staphylococcus aureus In Vivo,” *Angew. Chemie Int. Ed.*, vol. 57, no. 15, pp. 3958–3962, Apr. 2018.

[75] K. Zheng, M. I. Setyawati, D. T. Leong, and J. Xie, “Surface Ligand Chemistry of Gold Nanoclusters Determines Their Antimicrobial Ability,” *Chem. Mater.*, vol. 30, no. 8, pp. 2800–2808, Apr. 2018.

[76] L. Wang *et al.*, “The Density of Surface Coating Can Contribute to Different Antibacterial Activities of Gold Nanoparticles,” *Nano Lett.*, vol. 20, no. 7, pp. 5036–5042, Jul. 2020.

[77] Y. Zheng, M. Wei, H. Wu, F. Li, and D. Ling, “Antibacterial metal nanoclusters,” *J. Nanobiotechnology*, vol. 20, no. 1, p. 328, 2022.

[78] M. J. Hajipour, S. Laurent, A. Aghaie, F. Rezaee, and M. Mahmoudi, “Personalized protein coronas: a ‘key’ factor at the nanobiointerface,” *Biomater. Sci.*, vol. 2, no. 9, pp. 1210–1221, 2014.

[79] C. Corbo, R. Molinaro, M. Tabatabaei, O. C. Farokhzad, and M. Mahmoudi, "Personalized protein corona on nanoparticles and its clinical implications.," *Biomater. Sci.*, vol. 5, no. 3, pp. 378–387, Feb. 2017.

[80] J. Lazarovits *et al.*, "Synthesis of Patient-Specific Nanomaterials," *Nano Lett.*, vol. 19, no. 1, pp. 116–123, Jan. 2019.

[81] J. Ren *et al.*, "Precision Nanomedicine Development Based on Specific Opsonization of Human Cancer Patient-Personalized Protein Coronas," *Nano Lett.*, vol. 19, no. 7, pp. 4692–4701, Jul. 2019.

Chapter 2

Colloidal Synthesis of Gold Semi Shells using Metal Organic Framework as Sacrificial Template

2. INTRODUCTION

Colloidal asymmetric metal nanoparticles have been gaining a lot of attention due to their unique optical and magnetic properties and are hence finding widespread applications in fields as diverse as imaging probes [1], [2] sensors and therapeutics [3], [4]. This has led to further studies of such NPs for the development of advanced nanomaterials [5], [6]. Colloidal plasmonic nanostructures have optical properties based on their LSPR (Localized Surface Plasmon Resonance) which is observed due to collective oscillations of conduction electrons in the valence band of these metal nanoparticles excited by the incident radiation. This resonance spectra is dependent upon the geometry of these nanoparticles and the resonant wavelength can be tuned in the desired region of the electromagnetic spectrum upon changing the shape and size of these NPs [7]. Symmetric NPs such as gold nano shell (NS) consisting of silica core and thin layer of Au can be well explained by the Mie's theory and their plasmonic properties can be tuned by shell thickness and core size. However, asymmetric NPs do not have an isotropic plane for scattering of light and exhibit anisotropic scattering due to their difference in their plasmonic modes at different angles. Incomplete NS such as nanobowls or nanocups that can be collectively described as 'semi' shells have unique plasmonic properties due to their lack of symmetry [8]. These semi shells (SS) have two distinct dipole resonances- axial mode (parallel to axis of symmetry) and transverse mode (perpendicular to axis of symmetry) as compared to NS that have a single dipole resonance due to its symmetric centre. The transverse mode provides a strong magnetic component to the plasmon resonance due to production of a current loop by oscillating electrons and the dielectric medium on the surface of the metallic semi shells. This hybrid plasmonic resonance along with the charge accumulation at the edge of the rim result in a large field enhancement leading to red shift in the transverse plasmon resonance mode [9]. The magnetic dipole plasmonic mode also confers light bending character to the SS [10]. The possession of these unique properties by SS calls for their widespread use by researchers in study of metamaterials for numerous applications. However, the synthesis of SS remains a challenge due to various complex multistep procedures developed till now; thereby limiting their widespread usage. The physical methods of synthesis

include the template fabrication method wherein a template such as polystyrene beads is coated with metal thin films using chemical plating methods or top down techniques like magnetic sputtering or evaporation in a tedious multistep process that requires harsh and corrosive chemicals for dissolution of substrate required for shadowing of metal film on the template [11], [12] As described in Chapter-1, anisotropic etching of NS to form SS is a multistep procedure requiring various sophisticated techniques such as ion milling process or EBIA (Electron Beam Induced Ablation) for chemical deposition of metal film over NS followed by partially blocking their surface for anisotropic etching using strong acids such as HF for yielding SS [9] [13]. This method of partially blocking the surface for anisotropic growth/etching has been employed in various wet chemical synthesis procedures as well. Mann *et al.* [14] reported method involving polystyrene particles protected with polyphenylsiloxane patches were covered with an Au shell in a two-step seeding-plating sequence. Main disadvantages of this study included: tedious procedure, requiring high temperature and addition of toluene to dissolve polyphenylsiloxane patches. Similarly, Jiang *et al.* [15] reported another colloidal synthesis of gold SS based on vertex initiated selective overgrowth of Au on PbS nano octahedrons. However, the main disadvantages of this method are the use of toxic components like lead & CTAB for synthesis and addition of acid to dissolve the template. Ridelman *et al.* used a combination of partial surface blocking of Fe_3O_4 nanospheres followed by seeded growth of Ag-Fe_3O_4 heteronanostructures and the galvanic replacement of Ag with Au followed by dissolution of the Fe_3O_4 sacrificial template ultimately leading to the synthesis of free standing Au nano cups.[16] In addition, Gao *et al.* also reported synthesis of Au nanocups by thermal dewetting of Au shells encapsulated in between an inner SiO_2 core and an outer SiO_2 shell using calcination and chemical etching procedures.[2] Thus, complex multistep procedures requiring harsh reaction conditions or chemical etchants to dissolve the sacrificial template have been employed till date. Thus the need of a simple and rapid colloidal synthetic procedure for fabrication of SS at room temperature still stands as a challenge amongst material scientists.

In this chapter, we have developed a rapid colloidal one-pot synthetic procedure for *in-situ* formation of gold SS at room temperature using a biocompatible MOF (Metal Organic Framework) material ZIF-8 as a sacrificial template (**Fig 2.1A**). The unique self-etching property of ZIF-8 at acidic pH, as reported earlier [17], [18] has been exploited for the *in-situ* synthesis of gold SS as well as simultaneous dissolution of template without the need of any

additional etching agents. To the best of our knowledge, this is the first study to report a rapid colloidal synthesis of gold SS at room temperature using MOF as a sacrificial template.

2.1. Materials and Methods

Chloroauric acid (HAuCl4), 2-Methylimidazole (2-MIM), DTNB (5,5'-dithio-bis-(2-nitrobenzoic acid) and O-[2-(3-Mercaptopropionylamino) ethyl]-O′-methyl polyethylene glycol (M.W:5000 Da) were obtained from Sigma Aldrich. Zinc nitrate hexahydrate and L-ascorbic acid were obtained from TCI chemicals. Methanol was obtained from SDFCL. The glassware used for synthesis were cleaned with aqua regia carefully and rinsed with water thoroughly and oven dried properly before use. Double distilled water was used throughout the experiments unless mentioned otherwise. All chemicals were of analytical grade and were used as received without any further purification.

2.1.1. Synthesis of Rhombic dodecahedron (RD) ZIF-8

Zinc nitrate hexahydrate (150 mg) and 2-methylimidazole (350 mg) were dissolved in 7.2 mL methanol separately [19]. The 2-methylimidazole solution was added to zinc nitrate solution dropwise under stirring at 2000 rpm. Post 15 minutes of stirring, the solution was washed with methanol thrice with centrifuging at 7500 rpm for 15 mins. Post washing, the pellet obtained was dissolved in 1 mL double distilled water and sonicated in water bath until ZIF-8 was properly dispersed and used as soon as possible for semi shell preparation. It is important to note that ZIF-8 stored in aqueous medium for long term undergoes hydrolytic etching and thus becomes unsuitable for semi shell synthesis.

2.1.2. Colloidal synthesis of gold semi shells (SS)

Firstly, 400 µL of 2 mg/mL RD ZIF-8 was taken in a microfuge tubes to which 450 µL double distilled water was added. Next, $HAuCl_4$ solution (5 mM, 150 µL) was added to the ZIF-8 solution followed by addition of freshly prepared ascorbic acid solution (20 mM, 175 µL). The colour of the mixture turned to cyan indicating formation of the colloidal SS. The reaction was carried out at room temperature.

2.1.3. Characterization

UV-visible absorption spectra were recorded using UV-2600 spectrophotometer at room temperatre. Dynamic light scattering (DLS) and Zeta Potential measurements were performed on a Malvern zetasizer (model: nano ZSP). TEM images were recorded using JEOL 2100 with lanthanum hexaboride (LaB_6) filament at an accelerating voltage of 200 kV. SEM analysis was done using JEOL JSM IT300. Average nanoparticle size from electron micrographs was

measured using Gatan microscopy suite software. XRD measurements were recorded using Powder X-Ray Diffractometer (Model-D8 Advance) with Cu Kα (λ = 1.5406 Å) radiation in the 2θ range of 5°-80°.

2.1.4. Quantification of PEG drafted onto SS via the Ellman's Assay

PEGylation provides steric and thermodynamic stabilisation by controlling intrinsic colloidal aggregation behaviour and non-specific protein adsorption to SS in biological media. We investigated the grafting efficiency for different PEG density coated SS using Ellman's assay as per previous reports [20].

Briefly, freshly prepared SS were taken at a concentration of 5.072 $x10^{15}$ particles and were incubated with Thiol-PEG at different working concentrations (1.7 mM, 0.85 mM and 0.425 mM) overnight. The PEG:Au molar ratios were calculated as 0.34, 0.17 and 0.085 respectively for these PEG densities. The resultant PEG-modified SS were designated as: PEG-$SS_{0.34}$, PEG-SS $_{0.17}$ and PEG-$SS_{0.085}$. Next day, the PEGylated SS were centrifuge washed at 8000 rpm for 30 mins and the supernatant solution was used to detect unreacted thiols.

Briefly, 250 µL of supernatant solution was mixed with 95 µL of Phosphate buffer (0.1 M PB buffer mixed with 1 mM EDTA, pH 8) and 5 µL of 3 mM DTNB. The solutions were mixed thoroughly and were allowed to incubate at room temperature for 15 mins [21]. $DTNB^{-2}$ reacts with free sulphydryl groups to yield a mixed disulphide and 2- nitro-5-thiobenzoic acid TNB^{-2} which can be quantified via a colorimetric assay with maximum absorbance at 412 nm. Each sample was prepared in triplicates and percentage of reacted thiol was calculated using the formula:

$$\% \text{ Reacted PEG} = \frac{(\text{Total PEG added} - \text{Free PEG})}{\text{Total PEG added}} \times 100$$

2.1.5. Lyophilisation and reconstitution of PEGylated SS

The as synthesised SS were subjected to PEGylation at concentration of 5 mg/mL with overnight incubation. Next day, the SS were washed at 7500 rpm and dispersed in 1 mL double distilled water. The SS were then frozen in liquid nitrogen and subjected to lyophilisation (Temp:-120 °C, Pressure: 0.02 bar: Manufactured by Operon, Korea). The lyophilised SS powder was stored in -20 degrees and reconstituted in water as required. Post reconstitution, UV-Vis spectroscopy and TEM analysis were performed to assess retention of the morphology and optical property.

2.1.6. Photothermal transduction efficiency of SS

The photothermal transduction efficiency was carried out for PEGylated SS in accordance to previous study by Ropar *et al.*[22] and calculated according to the following equation:

$$\eta = \frac{[hS(Tmax - Tsurr) - QDis]}{I(1 - 10^{A808})}$$

where *h* is heat transfer coefficient, *S* is the surface area of the container, *Tmax* is the maxium temperature, and T_{Surr} is ambient temperature of the surroundings, QDis is the baseline energy input by the sample cell and A808 is the absorbance of nanoparticles at 808 nm.

Experimental condition for PTE involved reconstitution of 1 mg/mL of SS in a glass vial and sequentially irradiated with 750 nm and 808 nm laser for 5 mins each at 650 mW laser power. Both heating and cooling of the samples were measured using a FLIR Pro thermal imaging camera.

2.2. Results and Discussions

2.2.1. Synthesis and characterisation of SS

Taking advantage of the facet specific etching behaviour of ZIF-8 under acidic conditions, we employed them as sacrificial templates for in situ nucleation and growth of anisotropic gold nanoparticles. The room temperature driven rapid one pot synthesis involve mixture of chloroauric acid and rhombic dodecahedron ZIF-8 followed by reduction of gold with ascorbic acid (**Fig 2.1A**).

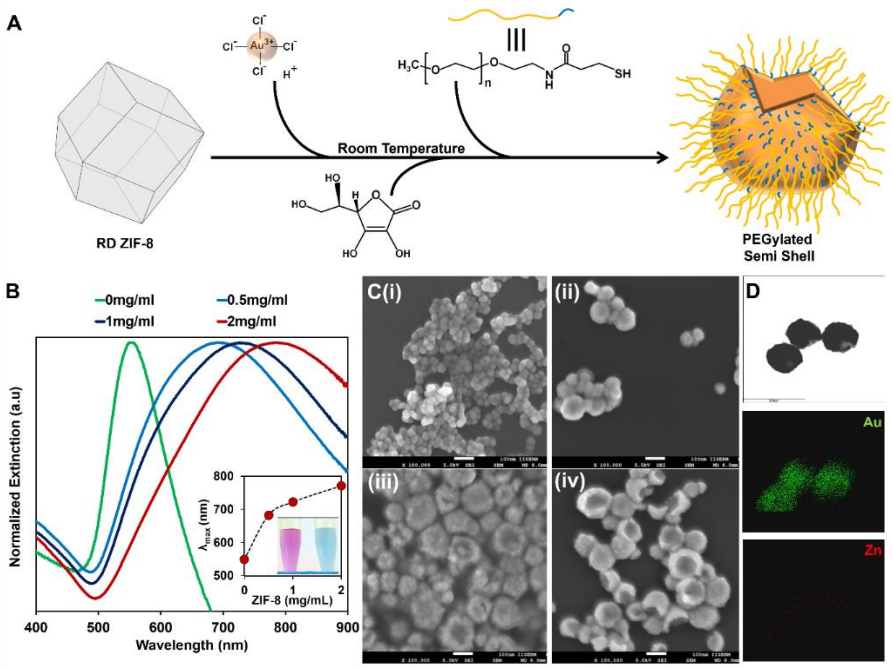

Fig 2.1:(A) Schematic of SS synthesis; (B) Extinction spectra and (C) FESEM images of SS prepared with different concentrations of ZIF-8 (inset in B show shift in λmax of semi

shell and colour change of reaction mixture from light ruby red to cyan in presence of ZIF-8); (D) Elemental mapping of SS for gold and zinc.

ZIF-8 feed concentration play vital role in determining the final shape of the gold nanoparticles, which also provided initial insights on the evolution of semi shell structures. A distinct colour difference of light ruby red and cyan was observed between the colloids synthesized in absence and presence of ZIF-8 respectively. The LSPR spectra of gold nanoparticles derived with different concentration of ZIF-8 showed linear red shift in the absorption maxima (**Fig 2.1B**). FESEM analysis confirmed formation of spherical and discoid shapes at lower concentrations to semi shells at higher concentrations of ZIF-8, while gold and ascorbic acid molar concentrations remained constant (**Fig 2.1C**). Due to complete solubilisation, no trace of ZIF-8 structures could be found in the semi shell colloid after post synthetic washing in double distilled water. However, elemental mapping detected trace amount of zinc being retained in the semi shells (**Fig 2.1D**), which was quantified with ICP-MS to be ~0.02% (w/w).

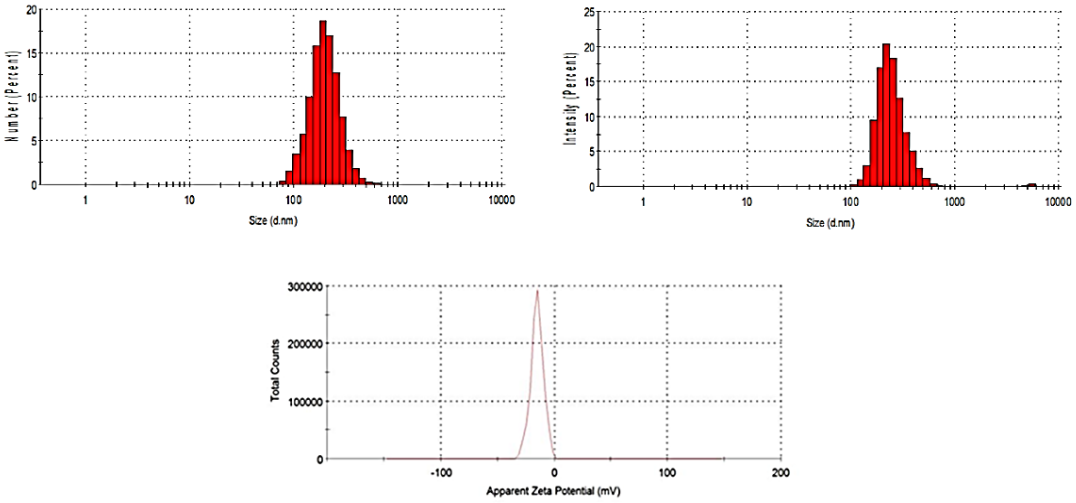

Fig 2.2: Size and charge distribution of reconstituted PEGylated SS.

The as prepared semi shells rapidly precipitated due to their anisotropic shape. Passivating the semi shell surface with polyethylene glycol significantly improved its colloidal stability. A PEG:Au molar ratio of 0.17 provided optimal grafting of ~82% (**Table 2.1**). PEG-$SS_{0.34}$ depicted lowest grafting efficiency while PEG-$SS_{0.42}$ possessed intermediate grafting efficiency.

Hydrodynamic size and zeta potential of PEGylated gold semi shells (SS) were measured to be ~190 nm and -15±5.65 mV (**Fig 2.2**). The size of SS could be tuned based on the size of ZIF-8, while agglomeration of the template interestingly lead to formation of flower petal-like arrangement of the semi shells (**Fig 2.3**).

Table 2.1 PEG grafting efficiency calculation for different PEG densities for gold semi shells structure obtained.

PEG added per Batch of semi shells	Thiol Added (µM)	PEG: Au Molar Ratio	Free thiol (µM)	Reacted thiol (µM)	Reacted thiol %
10 mg/batch	1702.2	0.34	452.88± 10.86	1249.31 ±10.86	73.39± 0.63
5 mg/batch	851.1	0.17	150.22± 3.62	700.87 ±3.62	82.34± 0.42
2.5 mg/batch	425.55	0.085	98.66± 10.42	326.88 ±10.42	76.81± 2.44

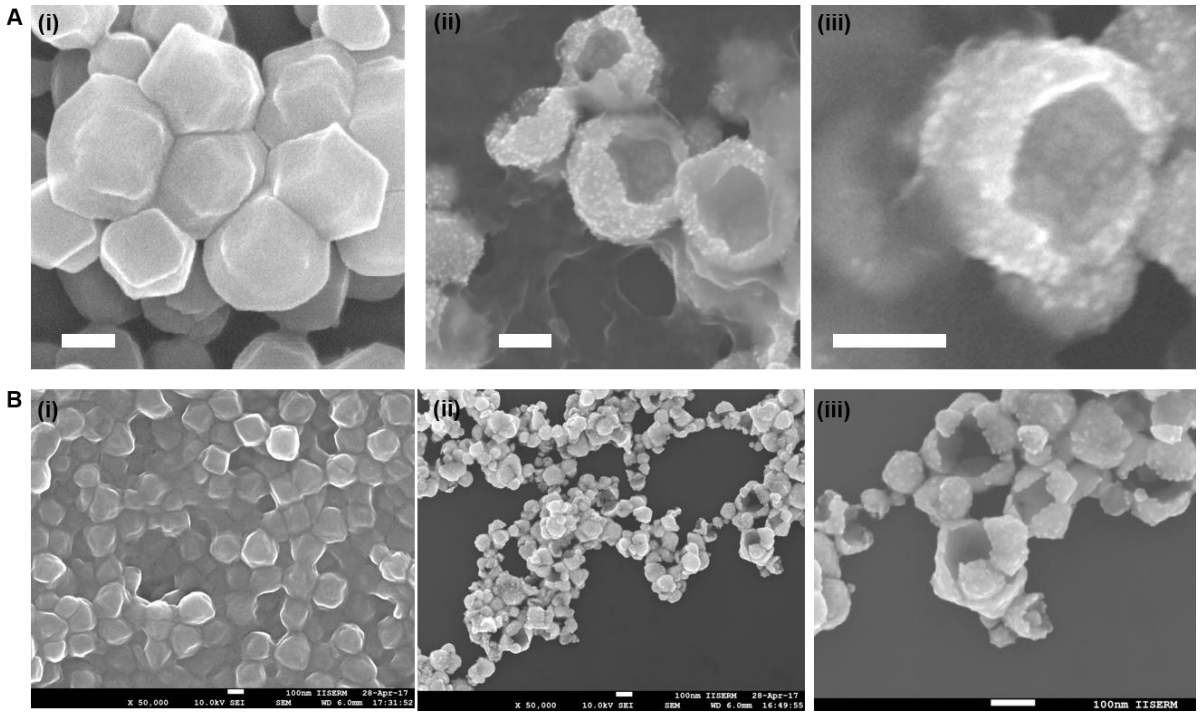

Fig 2.3: Effect of size (A) and agglomeration (B) of ZIF-8 on the morphology of gold nanoparticles. (Scale bar in A – 100 nm)

2.2.2. Elucidating the Mechanism of SS Formation

The mechanism of formation of solid gold semi-shell structures was investigated in conjunction with prior reports on anisotropic acid etching of ZIF-8.

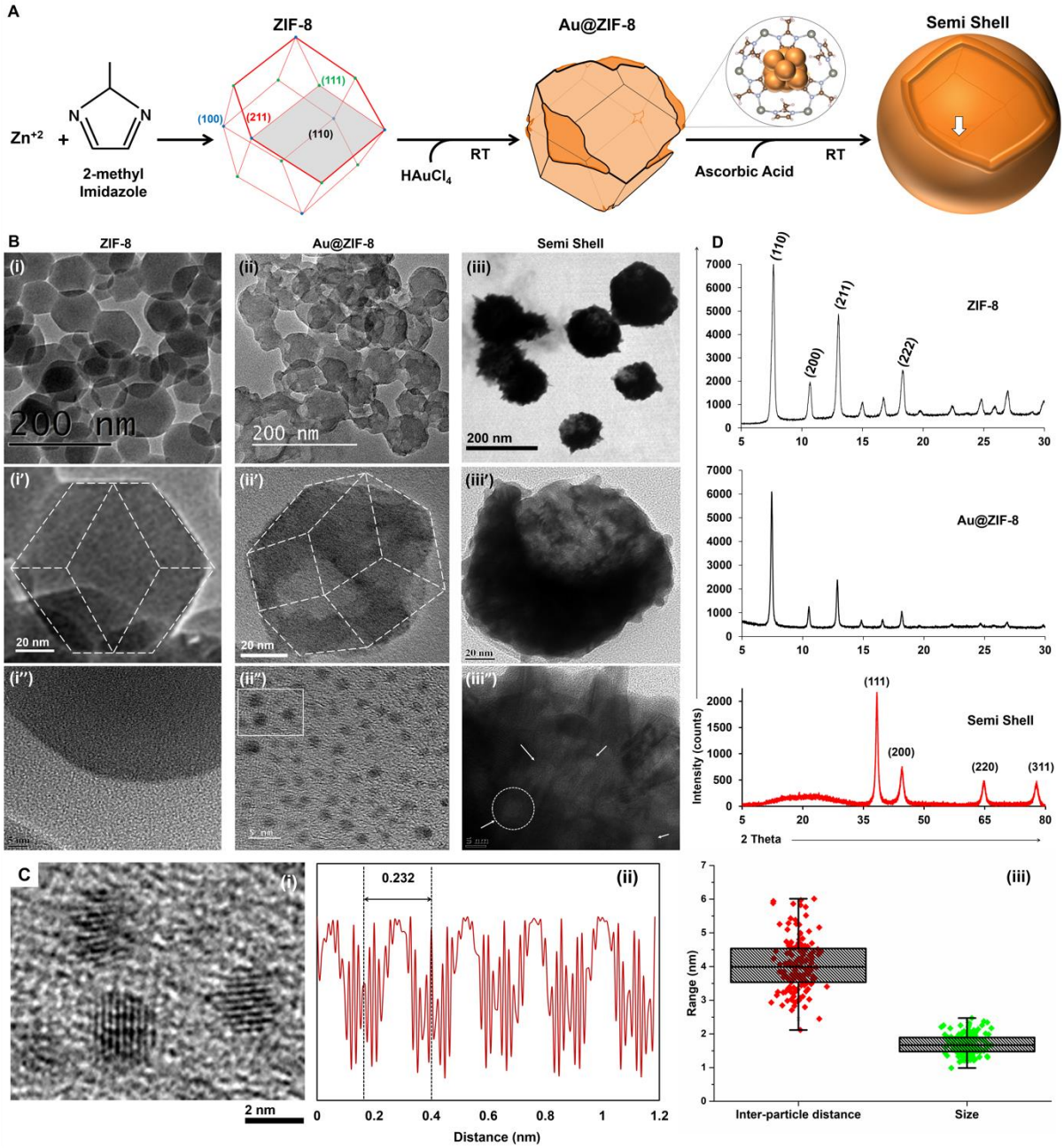

Fig 2.4: A) Summarized mechanism of semi shell formation from ZIF-8 template; B) TEM images of ZIF-8 (i, i' & i''), Au@ZIF-8 (ii, ii' & ii'') and SS (iii, iii' & iii'') at different magnifications (white arrows indicate remnant holes formed for outward diffusion of Zn^{2+} from core); C) High magnification TEM image of insert in B-ii'' (i), lattice spacing profile (ii) and size & inter-particle distance (iii) of gold nanoparticles within Au@ZIF-8. Arrow in A points at the indentation of {111} vertex of the ZIF-8 at the bottom of the semi shell. D) XRD pattern of ZIF-8, Au-ZIF8 and SS.

ZIF-8 with rhombic dodecahedron (RD) structure possesses six {100} surfaces, which are present at the corners bound by four edges, eight {111} surfaces, present at the corners bound

by three edges, and {211} surfaces present on the edge of the RD. Amongst these three kinds of surfaces, {100} and {211} are known to be prone to etching in acidic environments [17]. For the formation of a hollow semi-shell, we hypothesize that mixing of a strong monoprotic conjugate acid, $HAuCl_4$ (5 mM stock pH~2), with RD ZIF-8 induced simultaneous integration of Au^{3+} at the surface and initiated the formation of Kirkendall voids. Such Kirkendall voids are known to form in ZIF-8, wherein polyhedrons (regular hexahedron; RH and rhombic dodecahedron; RD) of ZIF-8 in the presence of Au^{3+} or Pt^{2+} undergo partial surface substitution of Zn^{2+} forming a bimetallic stable shell, followed by a complete diffusion of Zn^{2+} from the core to form Kirkendall voids. However, contrary to the prior observation of co-aggregation of the guest metal (Au^{3+} or Pt^{2+}) and Zn^{2+} [23][24], we noted monocrystalline nanoparticles on the surface of RD-ZIF-8. These nanoparticles were analyzed to be Au, as confirmed by the observed lattice spacing of 0.232 nm corresponding to the Au (111) plane. As ZIF-8 has an established host-guest interaction within its micropores, it is rational to expect Au^{3+} to diffuse into the pore aperture and nucleate inside these pores due to the mild reducing property of the imidazole groups.

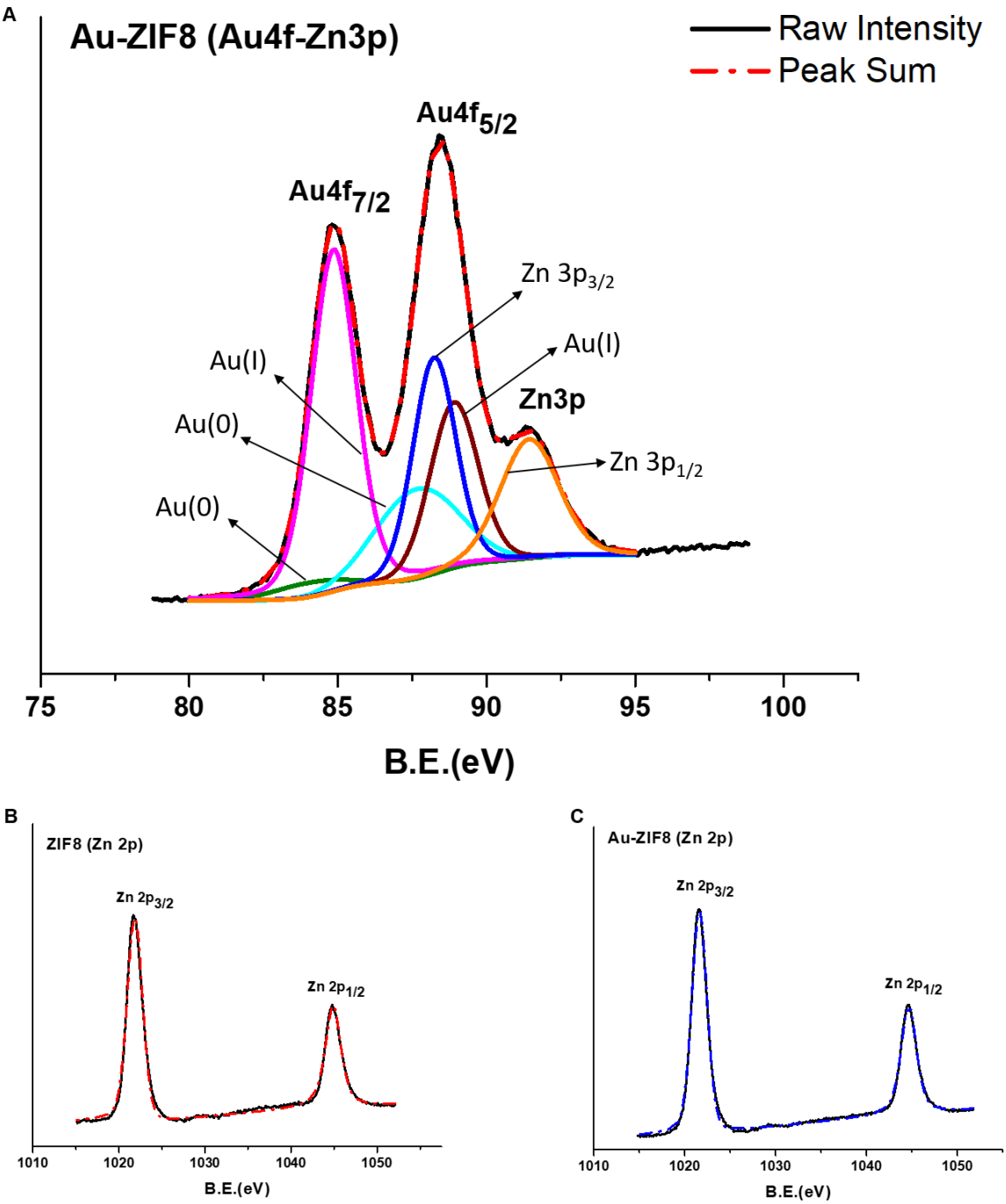

Figure 2.4.1: XPS high resolution (a) Au4f & Zn3p spectra of Au-ZIF8; (b) Zn 2p spectra of ZIF-8; (c) Zn 2p spectra of Au-ZIF-8.

X-ray photoelectron spectroscopy of these Au@ZIF8 revealed high resolution peaks centred at 84.85 eV and 88.9 eV corresponding to Au $4f_{7/2}$ and Au $4f_{5/2}$ respectively for Au (I) and peaks at 84.07 eV and 87.66 eV corresponding to Au (0) (**Figure-2.4.1 A**). The relative ratio of Au (I) to Au (0) was found to be 3:1. This observation indicates a structure similar to gold nanoclusters with Au (0) at the core and Au (I) at the surface interacting with a finite number of ligand, herein 2-methylimidazole. Additionally, peaks centred at 88.24 eV and 91.44 eV

corresponding to Zn $3p_{3/2}$ and $3p_{1/2}$ for Zn in +2 oxidation state were observed. The presence of Zn3p is consistent with previous reports for Au-Zn nanocomposites [25], [26]. Peaks corresponding to Zn $2p_{3/2}$ and $2p_{1/2}$ were also observed at ~1021 eV and ~1044 eV in both ZIF-8 and Au@ZIF-8 (**Figure-2.4.1 B & C**). The uniform and stable distribution of gold nanoparticles with average size of ~1.7 nm and mean inter-particle distance of ~4 nm (**Figure-2.4 C iii**) is expected to have formed within the central cavity of the unit cells of the ZIF-8 matrix that may expand in volume to accommodate host entities [27][28]. Prior reports indicate that gold nanoparticles with wide size range of 1-5 nm can be incorporated into ZIF-8 with local defects & deformities [29].

In addition to inducing such local defects for accommodating gold nanoparticles within the ZIF-8 framework, the acidic condition brought by $HAuCl_4$ also result in the etching of {100} and {211} surfaces of ZIF-8. This anisotropic etching was evident from the XRD analysis of Au@ZIF-8 (**Fig 2.4D**) wherein a reduction in the intensity of (100) and (211) planes by ~25 % and ~43 %, respectively, was observed relative to the (110) plane. The {110} surface is predominantly stable due to the absence of the acid-prone Zn-2-methylimidazole linkages [17]. TEM analysis of Au@ZIF-8 (**Fig 2.4B'**) also revealed etching of {100} and {211} surfaces of ZIF-8, which is consistent with previous report [18]. The addition of ascorbic acid (20 mM stock pH~3) to the Au@ZIF-8 accelerated the degradation of ZIF-8. This could have resulted in the coalescing of the gold aggregates present on the surface of ZIF-8 to grow into a semi shell. Interestingly, as seen with FESEM (**Fig 2.1C iv**) and TEM (**Fig 2.4B iii & iii'**), majority of the semi shells displayed single opening. This is surprising as the symmetric distribution of the (100) and (211) planes is expected to yield at least six independent openings if etched along the six <100> axial directions. However, FESEM (**Fig 2.5**) and TEM (**Figure-2.4B ii'**) analysis of Au@ZIF-8 indicated mostly three clear openings. These three openings are observed to be present on the same side of the hemisphere of RD-ZIF-8. It is presumed that further asymmetrical etching along {100} and {211} surfaces in these three openings, which is expedited by the addition of ascorbic acid, have resulted in the merger of these (small openings) to form a larger opening (the opening of the semi-shell). This is also confirmed with the presence of an indentation corresponding to the {111} vertex of the ZIF-8 at the bottom of the semi shell (**Fig 2.4A**).

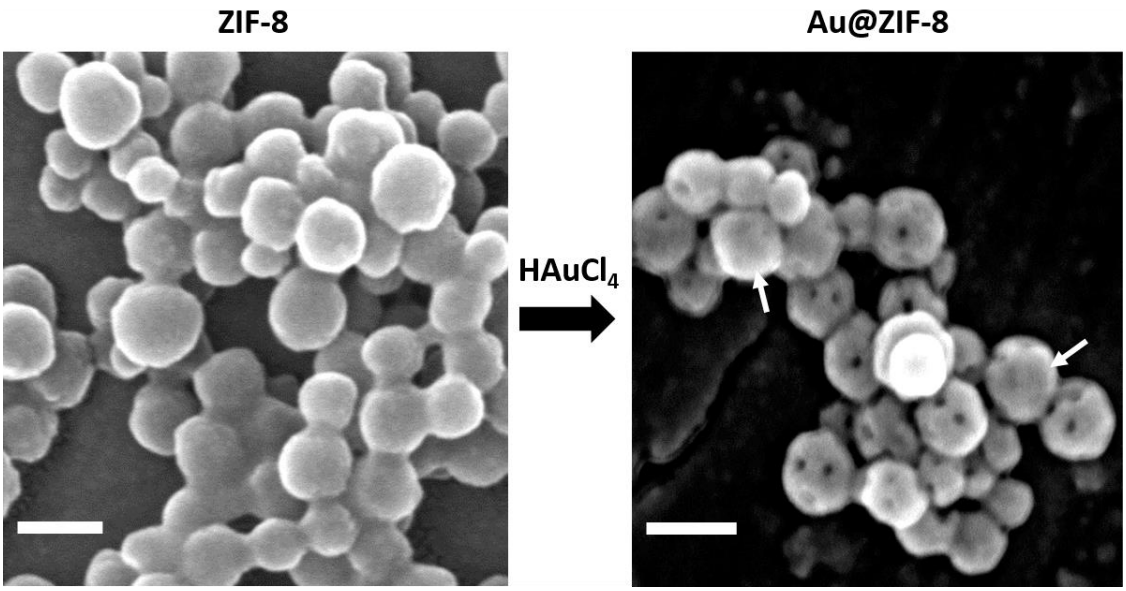

Fig 2.5: Anisotropic & asymmetric etching along three <100> zonal axes of ZIF-8 (2 mg/mL) with chloroauric acid (5 mM). Arrows indicate regions with shallow etching of the three symmetrically opposite <100> axes. (Scale bar – 100 nm).

Careful observation of RD-ZIF-8 structure reveals that the {100} surface, present at the corner, and the {211} surface present on the edges of the RD are not along the same planar level, which could explain the formation of zig-zag like openings of the semi-shell.

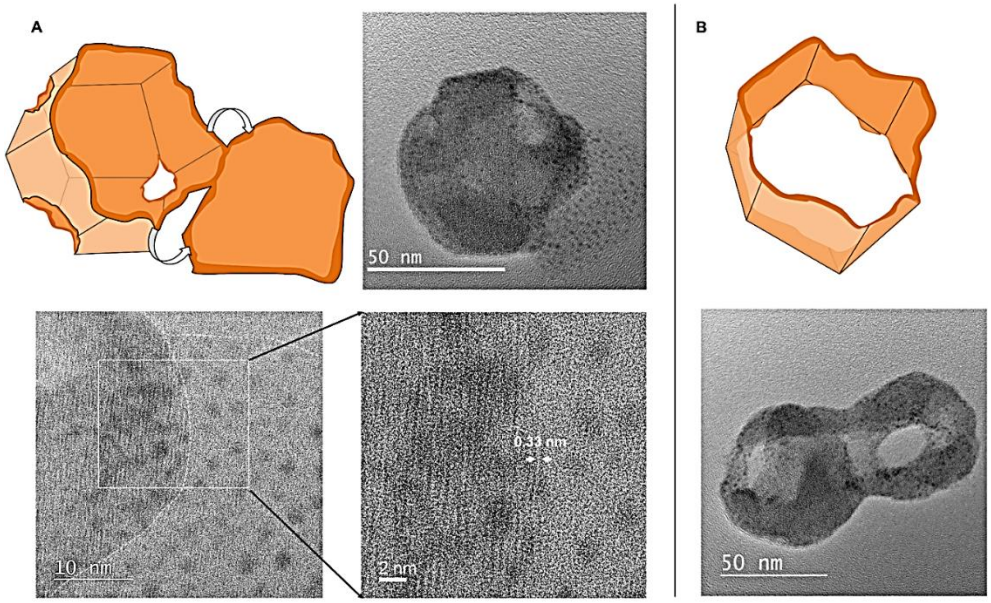

Fig 2.6: (A) Exfoliation of (110) facet from Au@ZIF-8 shell and the high resolution images of the boundary between intact Au@ZIF-8 and the exfoliated layer indicating pore aperture of ~0.33 nm; (B) Morphology of Au@ZIF-8 with symmetrical etching at all six <100> zonal axes.

One could also observe that there are openings symmetrically opposite to each other in Au@ZIF-8 (**Fig 2.6B**) which further confirms our hypothesis. The polycrystallinity, and the phase-purity of the semi shell and absence of structurally intact ZIF-8 at the end of the reaction was confirmed with XRD (Figure-2D). The ZIF-8 concentration dependent formation of semi shells that are shallow (discoid) and deep could be well correlated with this hypothesis (**Fig 2.7 and Fig 2.8**).

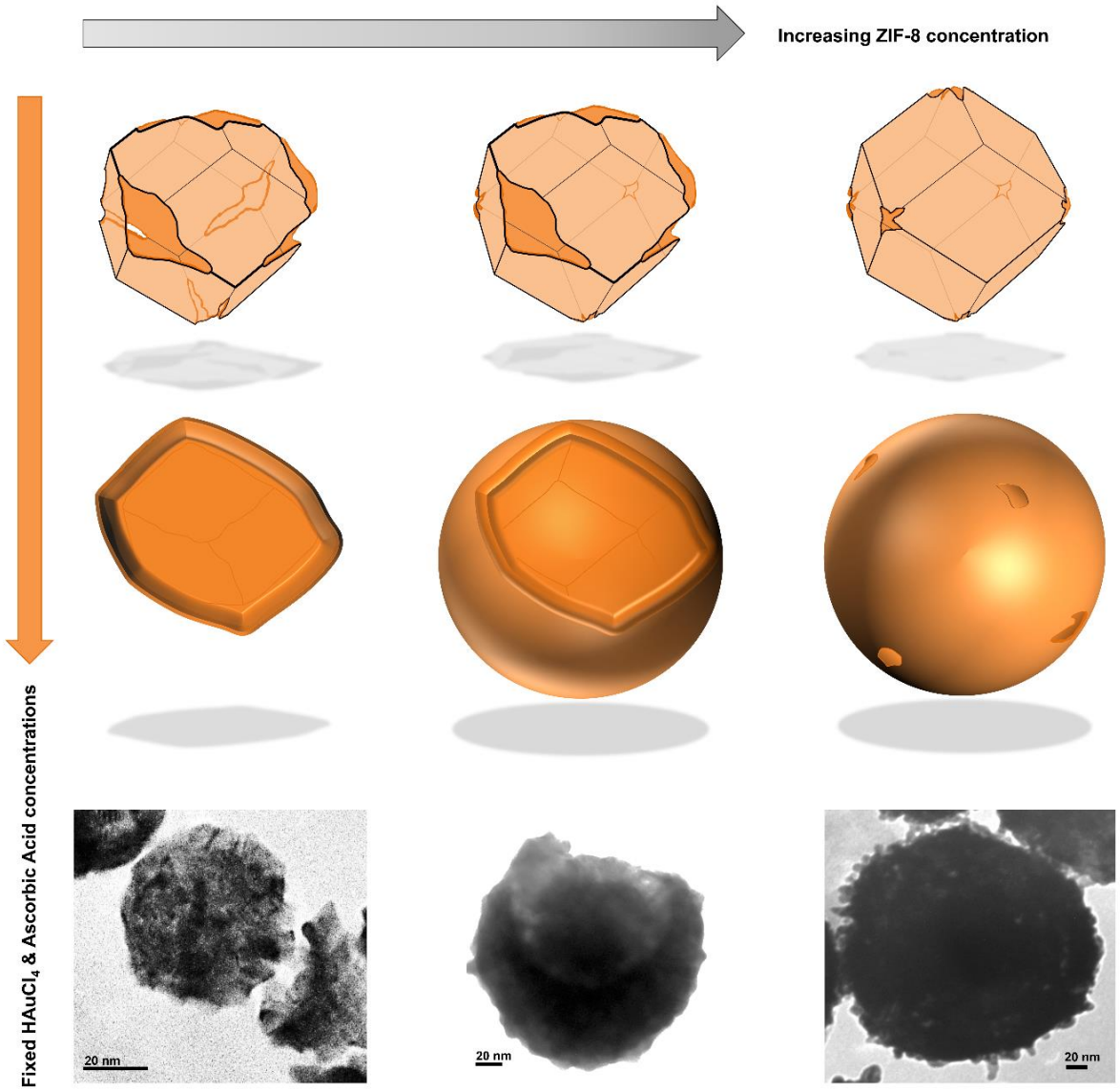

Fig 2.7: ZIF-8 concentration (0.5, 2, 3 mg/mL) dependent morphological outcomes of gold nanostructures at fixed chloroauric acid (5 mM) and ascorbic acid (20 mM) concentration.

At higher concentrations (> 3 mg/mL) of ZIF-8, spherical porous nano shells were observed. This could be explained by the fact that large number of ZIF-8 moieties are likely to be present

in the Au@ZIF-8, due to the increased concentration of ZIF-8. Since, the amount of $HAuCl_4$ and ascorbic acid, added to this was kept constant (same as that added for the formation of semi-shells), there is a possibility of inadequate etching of the {100} and (211} surfaces. This postulated mechanism explains the formation of spherical porous nanoshells of Au with no superior orifice and a broader plasmon resonance band, formed at higher concentration of ZIF-8 (**Fig 2.8**).

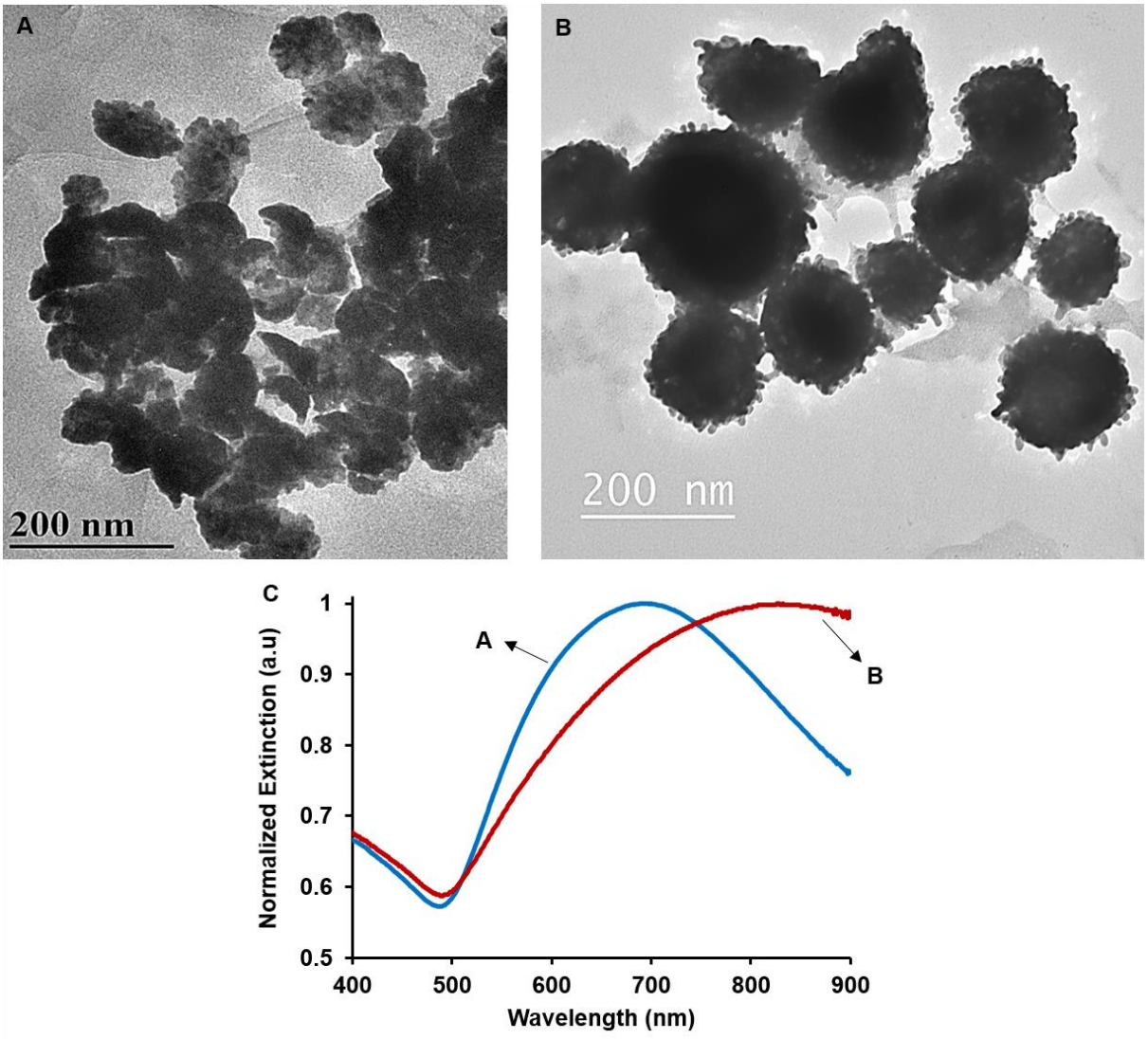

Fig 2.8: TEM images of nanocaps (A) and nano shell (B) prepared from 0.5 mg / mL & 3 mg/mL ZIF-8 respectively and their corresponding extinction spectra (C).

Additionally, we also studied formation of semi shells after adjusting ZIF-8 to pH~10 to neutralize protons contributed by $HAuCl_4$. Intriguingly, even after sequential addition of both $HAuCl_4$ and ascorbic acid the Au@ZIF-8 was predominantly intact displaying shapes similar to semi shells mostly with one large opening (**Fig 2.9**). These structures also clearly showed several holes in the shell involved in the outward diffusion of Zn^{2+} from the core. Remnants of

these holes could also be traced within the final semi shells structures as observed with TEM (**Fig 2.4 B iii''**).

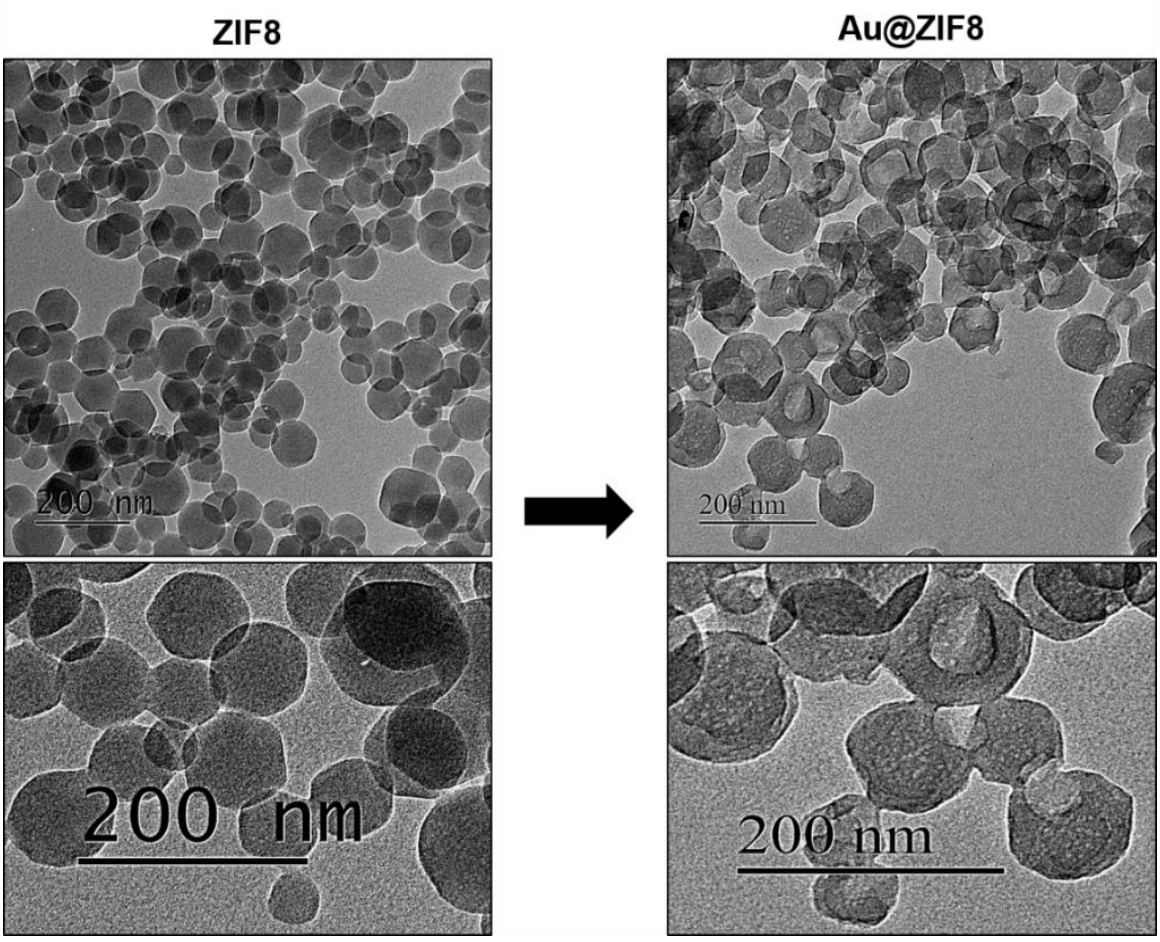

Fig 2.9: TEM images pre (A) and post (B) anisotropic etching of ZIF-8 with chloroauric acid at pH~10.

2.2.3. Lyophilisation and aqueous reconstitution of SS

While PEGylation significantly improved the colloidal stability of the semi shells, long term storage of SS is plausible only with cryopreservation. PEG has been successfully utilized in the past as both stabilizer and cryoprotectant of gold nanorods [30]. Lyophilized SS could be readily reconstituted in double distilled water or 0.9 % (w/v) saline after refrigerated storage up to six months (**Fig 2.10A**). The reconstituted SS retained the plasmonic peak and thermogenic property when irradiated with near infra-red light. Sequential irradiation of freshly reconstituted SS with 750 nm and 808 nm CW lasers at fixed power [**Fig 2.10 (B-D) and Fig 2.11**] and time of 650mW and 300 s respectively yielded ~25.6 % and ~36.2 % photothermal transduction efficiencies (PTE) (**Fig 2.11 and Table 2.2**). The PTE calculations are shown in detail in the next section.

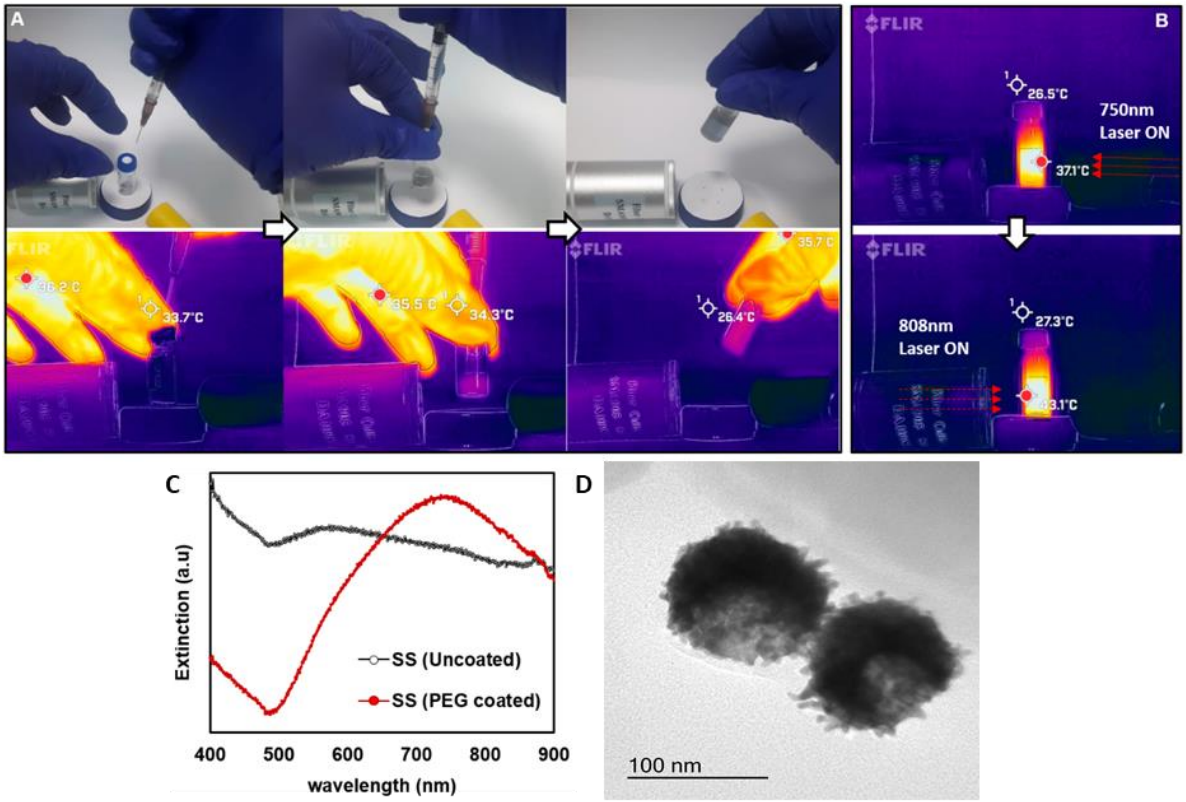

Fig 2.10: A) Ambient light (top) and thermal (bottom) images of the reconstitution of SS (1 mg) in 0.9% saline (1 mL); B) Thermal images of reconstituted SS post irradiation with 750 nm and 808 nm lasers for 300 s; C) Extinction spectra of semi shells (uncoated & stored overnight post synthesis) and freshly reconstituted PEGylated SS; D) TEM analysis of washed lyophilised and reconstituted SS.

2.2.4. Photothermal transduction efficiency of SS

The total energy balance for the system,

$$\sum_i m_i C_{p,i} \frac{dT}{dt} = Q_{NS} + Q_{Dis} - Q_{Surr} \qquad (1)$$

Where m and C_p are the mass and heat capacity of water respectively, T is the solution temperature, Q_{NS} is the energy input by nanoparticle system. Q_{Dis} is the baseline energy input by the sample cell, and Q_{Surr} is heat conduction away from the system surface by air.

$$Q_{NS} = I(1 - 10^{-A808})\eta \qquad (2)$$

where I is incident laser power, η is the conversion efficiency from incident laser energy to thermal energy, and $A808$ is the absorbance of the nanoparticle system at 808 nm.

$$Q_{Surr} = hS(T - T_{Surr}) \qquad (3)$$

where h is heat transfer coefficient, S is the surface area of the container, T is the temperature, and T_{Surr} is ambient temperature of the surroundings.

At a defined power of laser, $Q_{NS} + Q_{Dis}$ is finite. Since the heat output Q_{Surr} would keep on increasing with rise in temperature T, thus, for achieving maximum rise in temperature, heat input would be equal to heat output:

$$Q_{NS} + Q_{Dis} = Q_{Surr-Max} = hS(T_{Max} - T_{Surr}) \qquad (4)$$

Where $Q_{Surr\text{-}Max}$ is heat conduction away from the system when the sample cell reaches the equilibrium temperature, and T_{Max} is the equilibrium temperature. The PTT can be obtained by substituting (2) into (4) giving rise to the following equation:

$$\eta = \frac{[hS(Tmax - Tsurr) - QDis]}{I(1-10^{A808})} \qquad (5)$$

Wherein T_{Max} is the steady-state maximum temperature attained by nanoparticle system, T_{Surr} is the ambient room temperature, Q_{Dis} is the energy input based on the heat generated by the solvent (water) and sample well or baseline energy input, I is the laser power, and A_{808} or A_{750} is the absorbance of nanoparticles at 808 nm or 750 nm respectively. The heat transfer coefficient in the sample well surface area (hS) was determined.

To determine *hS* for eqn 5, a dimensionless driving force temperature, θ, is introduced using the maximum system temperature, Tmax.

$$\theta = \frac{T - T_{Surr}}{T_{Max} - T_{Surr}} \qquad (6)$$

And a sample system time constant τ_s

$$\tau_s = \frac{\sum_i m_i C_{p,i}}{hS} \qquad (7)$$

which is substituted into equation (1) and rearranged to yield

$$\frac{d\theta}{dt} = \frac{1}{\tau_s}\left[\frac{Q_{NS} + Q_{Dis}}{hS(T_{Max} - T_{Surr})} - \theta\right] \qquad (8)$$

When the laser source was turned off at the cooling stage of the nanoparticle system, Q_{NS} + Q_{Dis} = 0, thereby reducing the equation (8) to

$$\frac{d\theta}{dt} = \frac{-\theta}{\tau_s} \qquad (9)$$

and after integration, giving the expression

$$t = -\tau_s ln\theta \qquad (10)$$

The time constant (τ_s) was determined by plotting the time versus the negative logarithm of temperature in cooling period. Here, *m* is 1 g and *C* is 4.2 J/g°C. In addition, the laser power (I = 650 mW), and the absorbance of different nanoparticles at 750 nm and 808 nm (A_{750} or A_{808}) were also determined and substituted in equation (5).

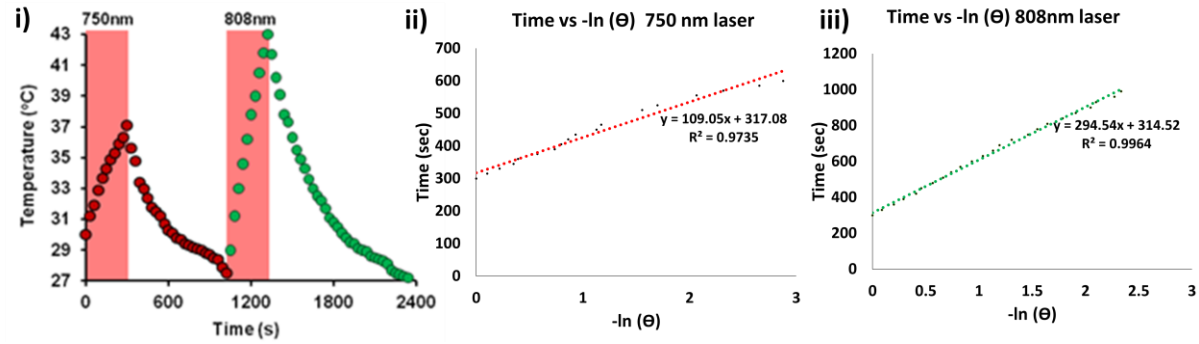

Fig 2.11: i) Heating & cooling cycles after sequential irradiation of SS with 750 nm and 808 nm lasers for 5 mins (laser power 650 mW); ii) Corresponding plots of linear fitting time versus negative natural logarithm with 750 nm (red) and iii) 808 nm (green) laser irradiation simultaneously for 5mins (laser power 650 mW).

Experimental condition for PTE involved reconstitution of 1 mg/mL of SS in a glass vial and sequentially irradiated with 750nm and 808 nm laser for 5 mins each at laser power 650 mW. Both heating and cooling of the samples were measured using a FLIR Pro thermal imaging camera. **Table 2.2** gives a summary of PTE parameters with both lasers at equal laser power 650 mW.

Table 2.2: Photothermal transduction efficiency parameters of semi shells with 750 nm and 808 nm NIR lasers.

Laser	hS (mW/°C)	T_{max} -T_{surr} (°C)	Tau (ζ) (s)	Absorbance at laser wavelength	Η (%)
750 nm	13.75	10.6	305.32	0.898	25.67
808 nm	13.1	15.7	320.59	0.895	36.26

Further, SS was found to have excellent photothermal stability with up to five cycles of intermittent 808 nm laser irradiation (**Fig 2.12**) confirming its potential as a photothermal nanotransducer.

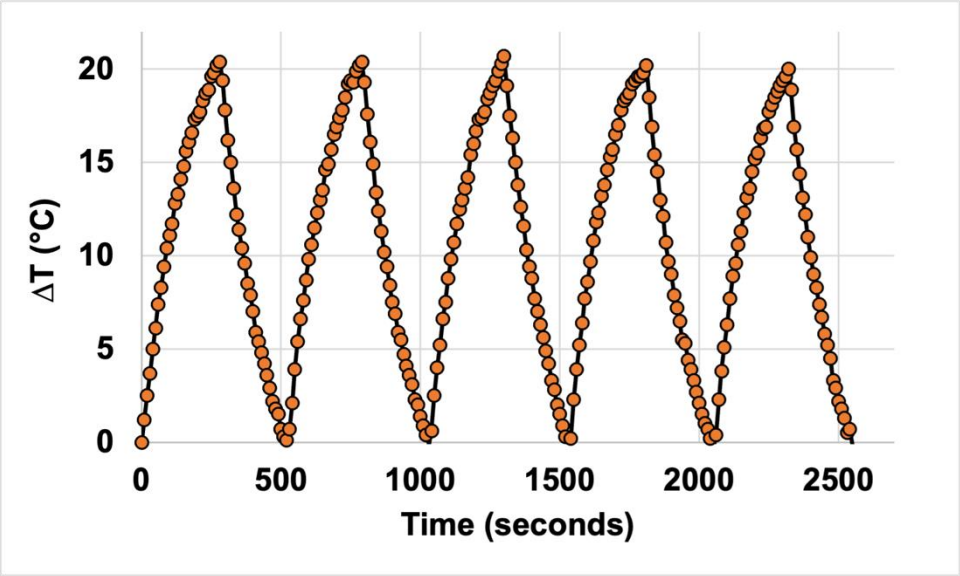

Fig 2.12: Photothermal stability of reconstituted PEGylated SS (1 mg/mL) with 808 nm (laser power: 1 W).

2.3. Conclusions and Future Prospects

A novel and interesting approach is reported for rapid colloidal in-situ synthesis of gold semi shells via a sacrificial pH dependant template ZIF-8 which dissolves with simultaneous synthesis of gold SS. This is a major breakthrough in the synthetic procedure for metallic SS which was considered as a long and tedious multi-step process requiring sophisticated instrumentation, toxic precursors and etching of templates post-synthesis with harsh acids like HF and HCl. The unique anisotropic shape of SS with LSPR in NIR confers it with a high photo thermal transduction efficiency which could be leveraged for various therapeutic applications like photo thermal therapy or a combinatorial photo/chemo therapy after establishing their safety and efficacy in a pre-clinical setup. The unique shape of SS can also be utilised for their SERS applications for bio-analyte detection. Moreover, the synthetic procedure can be extended to other metals like Ag, Cu for developing low cost photo thermal nanotransducers.

References:

[1] J. Choi, Y. Jun, S.-I. Yeon, H. C. Kim, J.-S. Shin, and J. Cheon, “Biocompatible Heterostructured Nanoparticles for Multimodal Biological Detection,” *J. Am. Chem.*

Soc., vol. 128, no. 50, pp. 15982–15983, Dec. 2006.

[2] A. Gao *et al.*, "Controllable Fabrication of Au Nanocups by Confined-Space Thermal Dewetting for OCT Imaging," *Adv. Mater.*, vol. 29, no. 26, p. 1701070, Jul. 2017.

[3] L. Y. Wu, B. M. Ross, S. Hong, and L. P. Lee, "Bioinspired Nanocorals with Decoupled Cellular Targeting and Sensing Functionality," *Small*, vol. 6, no. 4, pp. 503–507, Feb. 2010.

[4] S.-H. Hu and X. Gao, "Nanocomposites with Spatially Separated Functionalities for Combined Imaging and Magnetolytic Therapy," *J. Am. Chem. Soc.*, vol. 132, no. 21, pp. 7234–7237, Jun. 2010.

[5] J. Hu, S. Zhou, Y. Sun, X. Fang, and L. Wu, "Fabrication, properties and applications of Janus particles," *Chem. Soc. Rev.*, vol. 41, no. 11, pp. 4356–4378, 2012.

[6] C. Kaewsaneha, P. Tangboriboonrat, D. Polpanich, M. Eissa, and A. Elaissari, "Janus Colloidal Particles: Preparation, Properties, and Biomedical Applications," *ACS Appl. Mater. Interfaces*, vol. 5, no. 6, pp. 1857–1869, Mar. 2013.

[7] R. D. Averitt, D. Sarkar, and N. J. Halas, "Plasmon Resonance Shifts of Au-Coated ${\mathrm{Au}}_{2}S$ Nanoshells: Insight into Multicomponent Nanoparticle Growth," *Phys. Rev. Lett.*, vol. 78, no. 22, pp. 4217–4220, Jun. 1997.

[8] P. Van Dorpe and J. Ye, "Semishells: Versatile Plasmonic Nanoparticles," *ACS Nano*, vol. 5, no. 9, pp. 6774–6778, Sep. 2011.

[9] J. Ye *et al.*, "Fabrication and Optical Properties of Gold Semishells," *J. Phys. Chem. C*, vol. 113, no. 8, pp. 3110–3115, Feb. 2009.

[10] N. S. King, M. W. Knight, N. Large, A. M. Goodman, P. Nordlander, and N. J. Halas, "Orienting Nanoantennas in Three Dimensions To Control Light Scattering Across a Dielectric Interface," *Nano Lett.*, vol. 13, no. 12, pp. 5997–6001, Dec. 2013.

[11] Y. Lu, G. L. Liu, J. Kim, Y. X. Mejia, and L. P. Lee, "Nanophotonic Crescent Moon Structures with Sharp Edge for Ultrasensitive Biomolecular Detection by Local Electromagnetic Field Enhancement Effect," *Nano Lett.*, vol. 5, no. 1, pp. 119–124, Jan. 2005.

[12] C. Charnay *et al.*, "Reduced Symmetry Metallodielectric Nanoparticles: Chemical Synthesis and Plasmonic Properties," *J. Phys. Chem. B*, vol. 107, no. 30, pp. 7327–7333, Jul. 2003.

[13] J. B. Lassiter, M. W. Knight, N. A. Mirin, and N. J. Halas, "Reshaping the Plasmonic Properties of an Individual Nanoparticle," *Nano Lett.*, vol. 9, no. 12, pp. 4326–4332, Dec. 2009.

[14] D. Mann *et al.*, "Protecting patches in colloidal synthesis of Au semishells," *Chem. Commun.*, vol. 53, no. 27, pp. 3898–3901, 2017.

[15] R. Jiang *et al.*, "Colloidal Gold Nanocups with Orientation-Dependent Plasmonic Properties," *Adv. Mater.*, vol. 28, no. 30, pp. 6322–6331, Aug. 2016.

[16] Y. Ridelman, G. Singh, R. Popovitz-Biro, S. G. Wolf, S. Das, and R. Klajn, "Metallic Nanobowls by Galvanic Replacement Reaction on Heterodimeric Nanoparticles," *Small*, vol. 8, no. 5, pp. 654–660, Mar. 2012.

[17] Z. Ye, S. Wu, C. Zheng, L. Yang, P. Zhang, and Z. Zhang, “Self-Etching of Metal–Organic Framework Templates during Polydopamine Coating: Nonspherical Polydopamine Capsules and Potential Intracellular Trafficking of Metal Ions,” *Langmuir*, vol. 33, no. 45, pp. 12952–12959, Nov. 2017.

[18] C. Avci *et al.*, “Post-Synthetic Anisotropic Wet-Chemical Etching of Colloidal Sodalite ZIF Crystals,” *Angew. Chemie Int. Ed.*, vol. 54, no. 48, pp. 14417–14421, Nov. 2015.

[19] R. Chen, J. Zhang, Y. Wang, X. Chen, J. A. Zapien, and C.-S. Lee, “Graphitic carbon nitride nanosheet@metal–organic framework core–shell nanoparticles for photo-chemo combination therapy,” *Nanoscale*, vol. 7, no. 41, pp. 17299–17305, 2015.

[20] C. D. Walkey, J. B. Olsen, H. Guo, A. Emili, and W. C. W. Chan, “Nanoparticle size and surface chemistry determine serum protein adsorption and macrophage uptake,” *J. Am. Chem. Soc.*, vol. 134, no. 4, pp. 2139–2147, 2012.

[21] M. Bachelet and R. Chen, “Self-assembly of PEGylated gold nanoparticles with satellite structures as seeds,” *Chem. Commun.*, vol. 52, no. 61, pp. 9542–9545, 2016.

[22] D. K. Roper, W. Ahn, and M. Hoepfner, “Microscale Heat Transfer Transduced by Surface Plasmon Resonant Gold Nanoparticles,” *J. Phys. Chem. C*, vol. 111, no. 9, pp. 3636–3641, Mar. 2007.

[23] L. Tang, S. Zhang, Q. Wu, X. Wang, H. Wu, and Z. Jiang, “Heterobimetallic metal–organic framework nanocages as highly efficient catalysts for CO2 conversion under mild conditions,” *J. Mater. Chem. A*, vol. 6, no. 7, pp. 2964–2973, 2018.

[24] T. Kwon *et al.*, “Pt2+-Exchanged ZIF-8 nanocube as a solid-state precursor for L10-PtZn intermetallic nanoparticles embedded in a hollow carbon nanocage,” *Nanoscale*, vol. 12, no. 2, pp. 1118–1127, 2020.

[25] F. Jamali-Sheini, R. Yousefi, and K. R. Patil, “Surface characterization of Au–ZnO nanowire films,” *Ceram. Int.*, vol. 38, no. 8, pp. 6665–6670, 2012.

[26] Y. Cheng, S. Lu, W. Xu, H. Wen, and J. Wang, “Fabrication of superhydrophobic Au–Zn alloy surface on a zinc substrate for roll-down{,} self-cleaning and anti-corrosion properties,” *J. Mater. Chem. A*, vol. 3, no. 32, pp. 16774–16784, 2015.

[27] K. S. Park *et al.*, “Exceptional chemical and thermal stability of zeolitic imidazolate frameworks,” *Proc. Natl. Acad. Sci.*, vol. 103, no. 27, pp. 10186–10191, 2006.

[28] Y. Li *et al.*, “Cryo-EM Structures of Atomic Surfaces and Host-Guest Chemistry in Metal-Organic Frameworks,” *Matter*, vol. 1, no. 2, pp. 428–438, 2019.

[29] D. Esken, S. Turner, O. I. Lebedev, G. Van Tendeloo, and R. A. Fischer, “Au@ZIFs: Stabilization and Encapsulation of Cavity-Size Matching Gold Clusters inside Functionalized Zeolite Imidazolate Frameworks, ZIFs,” *Chem. Mater.*, vol. 22, no. 23, pp. 6393–6401, Dec. 2010.

[30] B. N. Khlebtsov, E. V Panfilova, G. S. Terentyuk, I. L. Maksimova, A. V Ivanov, and N. G. Khlebtsov, “Plasmonic Nanopowders for Photothermal Therapy of Tumors,” *Langmuir*, vol. 28, no. 24, pp. 8994–9002, Jun. 2012.

Chapter 3

Plasmonic Gold Semi Shells for Photothermal Ablation Induced Tumor Regression and Metastatic Inhibition of Breast Cancer

3. INTRODUCTION

Breast cancer is the second-leading cause of death amongst various types of cancers and is highly prevalent in women accounting to about 23% worldwide. It can be broadly categorized based on expression of three receptors: estrogen (ER), progesterone (PR), and HER2. All these subtypes are prone to develop a metastatic relapse with variability in time and site of relapse-including bone marrow, lungs, liver, brain and skeletal muscles[1]–[4] Metastasis is therefore a major challenge in the treatment of cancer and particularly in ~25% patients with breast cancer. Although the dormant metastases have been attempted to be managed clinically by one or combination of various therapeutic approaches like surgery, chemotherapy, radiotherapy and targeted therapy; still the relapse free patient survivability remains a challenge [1].

Photothermal therapy (PTT) has been widely used for treatment of cancer cells by employing photo-responsive nanomaterials that convert the irradiated light into heat energy for causing localised hyperthermia. PTT has been used alone as well as in conjugation with different combinatorial therapies such as chemotherapy, immunotherapy, gene regulation [5]. Gold based nanomaterials have been extensively studied for their role in PTT due to i) biocompatibility, ii) tunability of size for better tumor penetration, iii) high photothermal transduction efficiency i.e. the converting light to heat energy and vi) ease of functionalisation for highly specific and targeted cancer theranostics applications. Many gold nanomaterials such as gold nano shells, nano rods, hollow gold nano spheres, nano cages, and nano bottles have been successfully employed in photothermal ablation of cancer cells *in-vitro* as well as in pre-clinical mice tumor models [5]–[7]. However, their effective clinical translation remains as an impending and daunting challenge. The use of gold nanomaterials in PTT has been gaining popularity in treatment of breast cancer due to various advantages over conventional therapies including low systemic toxicity and minimal invasiveness [7]. However, the clinical effectiveness of PTT depends on various factors like exposure time, light type and dosage.

Hence detailed and in-depth pre-clinical data needs to be statistically validated to enable potential translation in a clinical setup.

In this chapter, we will discuss the potential application of PEGylated gold SS for photothermal ablation of breast cancer. The SS were assessed for any sub-acute toxicity and acute non-inflammatory response in preclinical C57BL/6 in-bred mice model over a period of 28 days. Further, pre-clinical tumor regression and survival rate of SS mediated PTT were assessed in tumored mice models. Effect of SS mediated localized PTT on systemic metastatic inhibition was also evaluated as a critical parameter for determining the translational potential of SS mediated PTT in a clinical setup.

3.1. Experimental Section:

3.1.1. Materials

Gold (III) chloride trihydrate ($HAuCl_4$), 2-Methylimidazole (2-MIM), were obtained from Sigma Aldrich. Zinc nitrate hexahydrate ($Zn(NO_3)_2 \cdot 6H_2O$), and L-ascorbic acid were obtained from TCI chemicals and methanol was obtained from SDFCL. MTT (Thiazolyl blue tetrazolium bromide) dye for cell culture (TC191; Himedia), bovine serum albumin (BSA; Himedia), nuclear staining dye- bisBenzimide H33342 trihydrochloride (Hoechst 33342, B2261; Sigma), cytoskeletal staining dye- Phalloidin Tetramethylrhodamine B isothiocyanate (Phalloidin-TRITC, P1951; Sigma), standard lipopolysaccharide from *E. coli* 0111:B4 strain; TLR4 ligand (TLRL-EBLPS; InvivoGen). All chemicals were of analytical grade and were used as received without any further purification unless mentioned otherwise. Ultrapure water (~18.2 MΩ) was used throughout the study.

3.1.2. Hemocompatibility of SS

Hemolysis assay was performed using human blood collected from a healthy volunteer after obtaining necessary approvals from institute ethics committee of IIT Bombay (IITB-IEC/2019/031). Briefly, PEG coated SS and uncoated SS were re-dispersed in PBS and tested for hemolysis at concentrations of 25, 50, 100, 200, 250 µg/mL. Briefly, 150 µL of RBC fraction were added to 750 µL of PEG coated and uncoated SS solution at different concentrations and the mixture was incubated for 1 hour at 37 °C in an incubator shaker at 180 rpm. After incubation, the mixture was gently centrifuged and the supernatant were analysed for leaked haemoglobin. The absorbance of released haemoglobin was recorded at 577 nm for each sample and subtracted from reference wavelength recorded at 655 nm using multimode plate reader. Double distilled water and PBS were used as positive (PC) and negative controls

(NC) respectively. The experiment was carried out in triplicates [8]. The percentage hemolysis was calculated using the formula:

$$\% \text{ Hemolysis Control} = \frac{\text{Sample absorbance} - \text{NC absorbance}}{\text{PC absorbance} - \text{NC absorbance}} \times 100$$

The RBCs obtained from pellet after the experiment were fixed using 4% paraformaldehyde and stored at 4°C until the SEM analysis was carried out in order to analyse the effect of PEG coated and uncoated SS on the morphology of blood cells.

3.1.3. Cell culture

MTT [3-(4,5-Dimethylthiazol-2-yl)-2,5-Diphenyltetrazolium Bromide] was purchased from HiMedia. Phalloidin-tetramethylrhodamine B isothiocyanate (Phalloidin-TRITC) and bisBenzimide H 33342 trihydrochloride (Hoechst 33342) were purchased from Sigma Aldrich. MDA MB 231 (Triple negative human mammary epithelial adenocarcinoma) were purchased from NCCS, Pune, India and maintained in DMEM supplemented with 10% FBS and 1% antibiotic solution in an incubator at 37 °C , 5% CO_2. HUVEC were procured from Lonza (Cat.No. 2517A) and maintained in endothelial growth medium supplemented with Lonza Bullet kit (Cat. No. 3162). All the cells were maintained by subculturing them 2-3 times per week.

3.1.4. *In-vitro* biocompatibility

The biocompatibility of SS was evaluated using HUVEC cells via MTT assay. HUVEC cells were seeded at a density of 2.5×10^4 cells in a 96 well plate for 24 hours at 37 °C and 5% CO2 in a total volume of 100 µL. Following day, the media was substituted with different concentrations of SS (0, 25, 50, 100 µg/mL) and incubated for 24 hours. The following day, the media containing nanoparticles were removed and the cells were washed with PBS to remove traces of sample. Next, 10 µL MTT (5 mg/mL dissolved in PBS) diluted with 90 µL media was added and incubated for 4 hours. After incubation, the media was carefully removed and 100 µL of DMSO was added to each well and aspirated properly to dissolve the purple formazan crystals. The absorbance was recorded at 595 nm on a multimode plate reader. Cell viability percentage was calculated using the formula:

$$\text{Cell viability \%} = \frac{\text{Absorbance of sample at 595nm}}{\text{Absorbance of control at 595nm}} \times 100$$

3.1.5. Confocal uptake of in HUVEC cells

To study the morphological changes of SS treated HUVEC cells, the bright field images were taken along with confocal images. For confocal analysis, the HUVEC cells were seeded on a coverslip at a density of $5x10^4$ cells per well in a 6 well plate for 24 hours. Next, SS was added at different concentrations. Post 24 hours incubation, the media along with containing nanoparticles were removed the following day. The cells were then washed with 1x PBS thrice to remove any trace amounts of sample left. Next, the cells were fixed with 4% paraformaldehyde for about 15 minutes. The nuclei of fixed cells were stained with nuclear staining dye (Hoechst 33342) for 10 minutes and washed with PBS twice post staining. This was later followed by staining the cytoskeletal F-actin with Phalloidin-TRITC for 20 minutes and washing with PBS twice. The cells were mounted on a glass slide and observed under a LSM 880 confocal microscope (Carl Zeiss, Germany).

3.1.6. Internalization of SS in MDA MB 231 breast cancer cells

To check the internalisation of PEG-SS in breast cancer cells, the MDA MB 231 cells were seeded on a coverslip at a density of $5x10^4$ cells per well in a 6 well plate for 24h. Following adhesion, the PEG-SS NPs were incubated at concentration of 100 µg/mL for 24h. The cells were then washed with PBS thrice and fixed with 4% PFA for 10 mins. Next, the nuclei were stained with 2 µg/mL of Hoechst 33342 for 10 min at 37°C followed by PBS washing thrice. Finally, the cells were stained with 100nM Lysotracker Red and incubated for 2 min at RT followed by multiple PBS washings to remove excess stain from the cells. The treated cells were mounted on top of a glass slide and stored in 4°C till observation under a confocal microscope.

3.1.7. Time dependant Photothermal Ablation of cancer cells

To study the effect of laser timing on the photothermal ablation of breast cancer cells, MDA MB 231 cells in the addition of SS were irradiated for differential time periods (2.5, 5, 10 minutes) at a fixed concentration of 100 µg/mL using 808 nm laser and the cytotoxicity was evaluated via MTT assay. The experiment was carried out in triplicates and the results were recorded as Cell viability (% Control).

3.1.8. Live/Dead Assay

Briefly, $8x10^3$ MDA MB 231 cells were seeded in a 48 well plate and grown till ~70% confluency. Subsequently, the SS mixed with fresh media were added at concentration of 100 µg/mL. The controls along with the sample were treated with 808nm laser for 10 minutes. Next

day, the media was removed and the cells were washed 1x with PBS. Then the cells were stained with FDA (5 mg/mL) and PI (2 mg/mL) and incubated at room temperature for 15 minutes. Next, the staining solution was removed and washed with PBS followed by immediately imaging with confocal microscope.

3.1.9. *In-vivo* biodistribution and acute/sub-acute safety assessment post SS intravenous dosage

All experimentation involving animals were performed in accordance to the IISER Mohali (Approval no: IISERM/SAFE/PRT/2021/023). Throughout the study, the mice were housed at animal house at IISER Mohali in individually ventilated cages at a temperature of 22 ±2 °C and relative humidity of 50-60 % under a 12 hours light and dark cycle. For the biodistribution study, 6 weeks old C57BL/6 mice were divided into three groups, each administered with saline (control), liposaccharide (LPS) and semi shell (SS) (n=3 per group) and were used for studying safety and biodistribution following a repeated dosage at Day 0 and Day 14 over a course of 28 days. SS dosage was 5mg/kg (Au equivalent) through the tail vein. Lipopolysaccharide dosage was 2mg/kg only at Day 0 for serving as positive control to acute inflammatory analysis. At end points, the blood was collected and major vital organs- heart, lungs, kidneys, liver and spleen were harvested. The collected blood was allowed to clot for 30 minutes at room temperature and was centrifuged at 4000 rpm for 10 minutes at 4 °C. The serum was collected as the supernatant and analyzed for markers related to inflammation and organ function. The acute inflammatory analysis was carried out on selected markers using the BioLegend LEGENDplexTM Mouse inflammation Panel kit using Flow Cytometry. For organ specific biomarkers: Serum glutamic oxaloacetic transaminase (SGOT)/aspartate aminotransferase (AST), Serum glutamic pyruvic transaminase (SGPT)/alanine aminotransferase (ALT), Blood Urea Nitrogen (BUN) and Creatinine were assessed for hepatic and renal functioning. To determine the amount of gold present in the major organs post 28 days, ICP-MS analysis was carried out. The harvested organs were weighed and digested with ICP grade HNO3 and further diluted with double distilled water prior to elemental analysis. The standard preparation for ionic gold was carried out in the range of 10-500 ppb. For histopathological evaluation, the organs were fixed in 10% formalin immediately after harvesting and processed for hematoxylin and eosin (H&E) staining. The stained slides were then studied under an optical microscope for any microarchitectural changes.

3.1.10. Pre-clinical bed side reconstitution of SS for intra-tumoral administration, monitoring of photothermal temperature rise and survival analysis post photothermal therapy

A syngeneic tumor mouse model for human breast cancer was developed using the highly metastatic 4T1 breast cancer cells in female Balb/c mice by injecting 1 x 10^6 cells per mice dispersed in serum free media on the right flank of the mice. The mice were observed daily and the tumor size was measured using a vernier caliper until a palpable size of 100-120 mm^3 was developed. The mice were divided into four groups: saline, Laser, SS and SS+Laser with n=4 in each group. For intratumoral injection, SS powder (0.2 mg) was reconstituted in 100 µL of 0.9 % saline and 50 µL was injected directly into the 4T1 tumor grafted on the right flank of female BALB/c mice in the SS groups (SS, SS+L). The saline and Laser groups were intratumorally injected with 0.9% saline. An 808 nm laser was used at 650 mW power to irradiate the tumor region for 5 minutes on day 0 and day 1. The body weight and tumor volume of all the animals were periodically recorded until the day of morbidity related death of mice in the four groups for a period of 3 months. Post death, vital organs in saline (including tumor) and SS+Laser groups were excised for histopathology analysis. The bed-side reconstitution of SS and administration followed by photothermal temperature monitoring of both head and tumor of the mice were recorded simultaneously with FLIR Pro thermal imaging camera.

3.1.11. Bioluminescence imaging of primary tumor and its pulmonary metastasis post photothermal therapy with SS

Preclinical photothermal efficacy for tumor regression analysis and bioluminescence imaging was carried out at ACTREC, Mumbai with prior Institutional Animal Ethics Committee. The photothermal efficacy of SS was carried out in 4T1 xenograft breast tumor model by subcutaneously implanting 1 × 10^6 cells 4T1 FL2 cells on the right flank of CD1 Nude mice. Post injecting the cells, the tumor growth was continuously monitored by bioluminescence imaging using IVIS Lumina II imaging system (Caliper Life Sciences, USA) by intraperitoneally administering D-luciferin as substrate (100 µL of 30 mg/mL per mouse) . The imaging was carried out at intervals of 1 minute between two subsequent images till the maximum bioluminescence signal was observed. Once the desired tumor volume was achieved (80-100 mm^3), mice were randomly segregated into different groups: control (Saline), material control (SS alone), laser control (808 nm laser irradiation alone) and treatment (SS+laser) groups with sample size n = 3 for control groups and n=5 for treatment group. Control group mice were intratumorally injected with 100 µL of PBS while material control and treatment

groups were intratumorally administered with 100 µg of SS powder reconstituted in 100 µL saline. The photothermal treatment was carried out by irradiating the tumors with a 808 nm laser (650 mW) for 5 minutes on Day 0 post-imaging (first treatment) and Day 1 pre-imaging (second treatment). Bioluminescence imaging was carried out for all groups at regular intervals in order to monitor the in vivo efficacy of SS for photothermal therapy. The luminescence signal output was quantified in terms of average radiance (p/s/cm^2/sr) using Living Image v4.4 software and represented by a false color scale as a function of the photons captured by the detector. After sacrificing the mice, the bioluminescence was recorded in order to assess organ metastasis in different groups. Post sacrifice, the serum was collected and stored at -80 °C to carry out serum biochemistry analysis.

3.1.12 Statistical Analysis

All the graphs were plotted using OriginPro software. Student's t-test was performed for statistical significance analysis.

3.2. Results and Discussions

3.2.1. *In-vitro* and preclinical safety assessment of SS

As it is imminent for the SS to come in contact with blood post *in vivo* administration for therapeutic applications, its hemocompatibility was primarily assessed. It was observed that irrespective of the concentration, uncoated SS caused severe haemolysis similar to positive control.

However, SS passivated with PEG at concentrations up to 250 µg/mL did not cause any obvious haemolysis as shown in **Fig 3.1A**. The PEGylated SS also showed excellent dose dependent uptake in HUVEC cells with clear distribution within the cytoplasm and possessed fairly good viability of ~79 % at 100 µg/mL with well retained morphology (**Fig 3.1B** and **Fig 3.2**). Further, acute (1-day post injection) and sub-acute (28 days post injection) toxicity assessment was performed with intravenous injection of SS (5 mg/Kg equivalent of Au) at the tail vein of healthy C57BL/6 mice. ICP-MS analysis of organs indicated predominant accumulation in liver and spleen post 28 days, which is similar to the trend observed for similarly sized gold nanoparticles [26], [27] (**Fig 3.3A**). Serum levels of acute inflammatory cytokines such as MCP-1, TNF-α, IFN-ɤ, IL-6, IL-10, IL-23 remained normal (**Fig 3.1C**). Body weight of SS injected mice remained same as that of saline control (**Fig 3.1B**). Serum biomarkers such as aspartate aminotransferase, alanine aminotransferase, blood urea creatinine and creatinine analysed post day 28 of injection were found to be within the normal reference range for C57BL/6 mice (**Fig 3.1C**). Histopathological analysis with hematoxylin and eosin

staining of vital organs did not indicate any signs of acute or sub-acute tissue damage (**Fig 3.1D**). These observations established preclinical safety for further phototherapeutic assessment of SS.

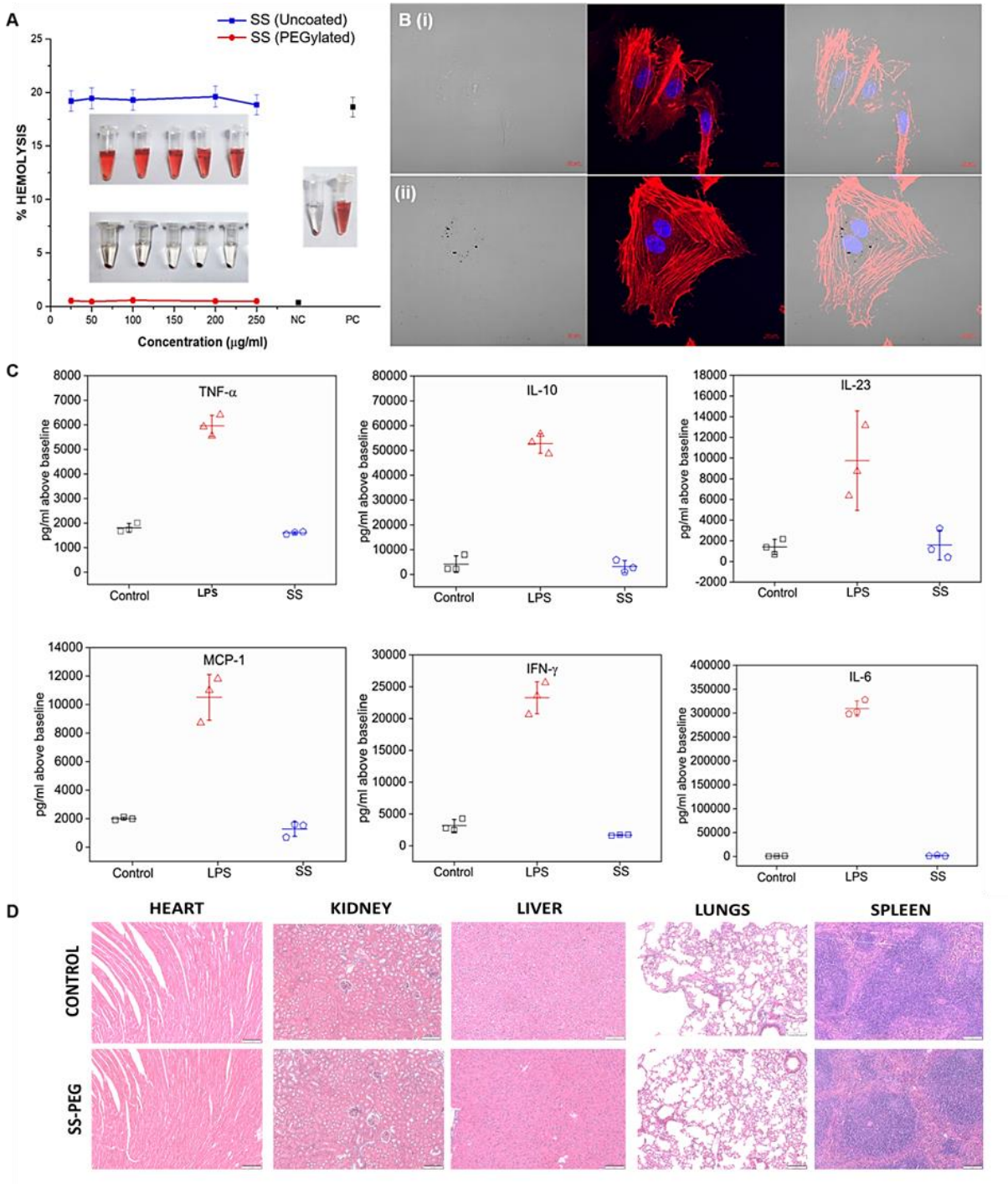

Fig 3.1: A) Hemolysis assessment of SS; B) HUVEC cells treated with blank media (i) & media containing 50 µg/mL SS (ii) and stained for actin (red) and nucleus (blue); C) Levels of serum inflammatory markers 24 hours post intravenous injection with saline (control), lipopolysaccharide (LPS) and SS; D) Hematoxylin & Eosin staining of vital organs post treatment at day-1. Scale bar-100 µm.

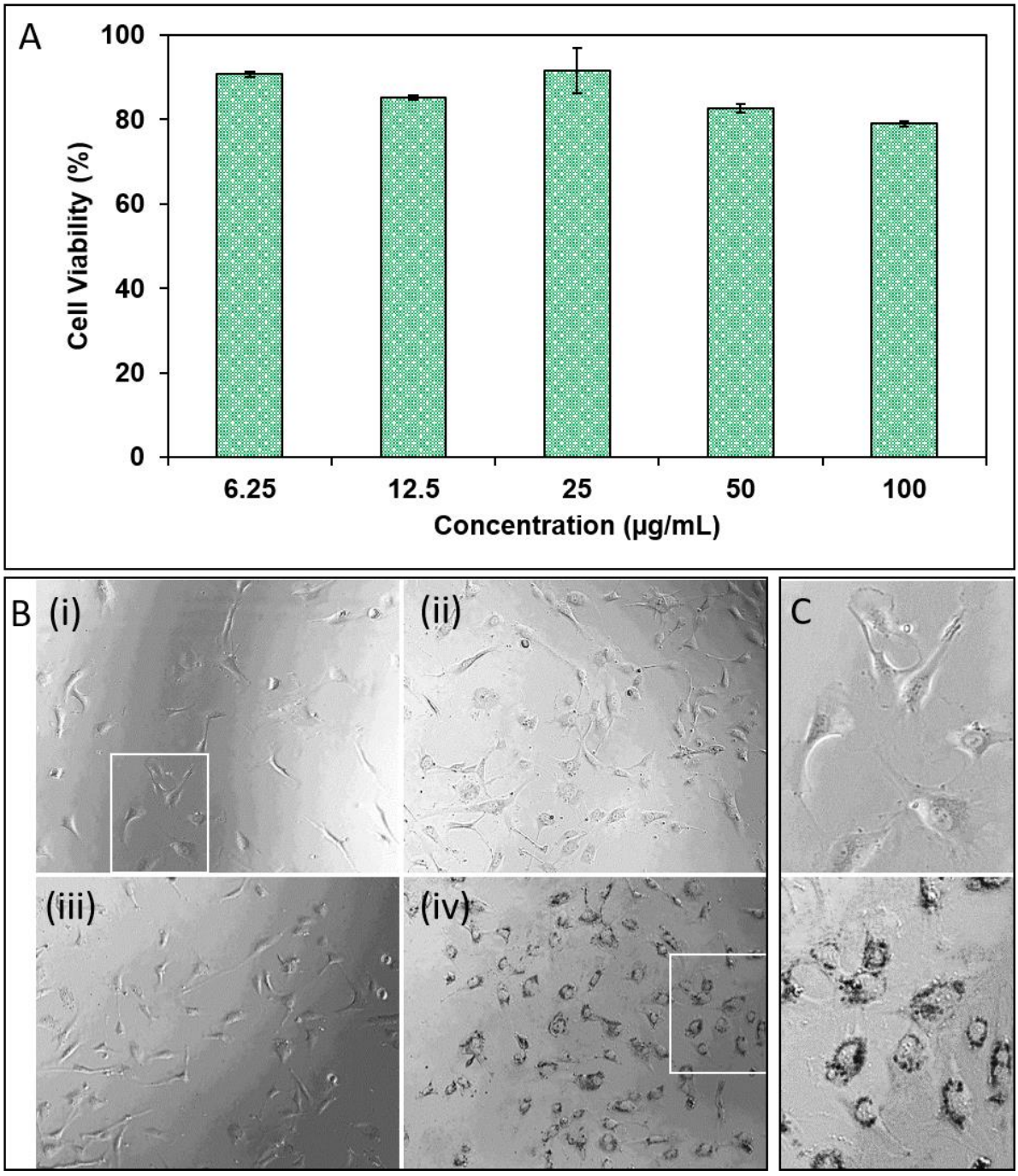

Fig 3.2: (A) Percentage viability of HUVEC cells post treatment with different concentrations of PEGylated SS; (B) Bright field microscopic images of HUVEC cells treated with (i) 0 µg/mL, (ii) 25 µg/mL, (iii) 50 µg/mL and (iv) 100 µg/mL PEGylated SS; (C) Magnified image of the regions highlighted in (i) and (iv).

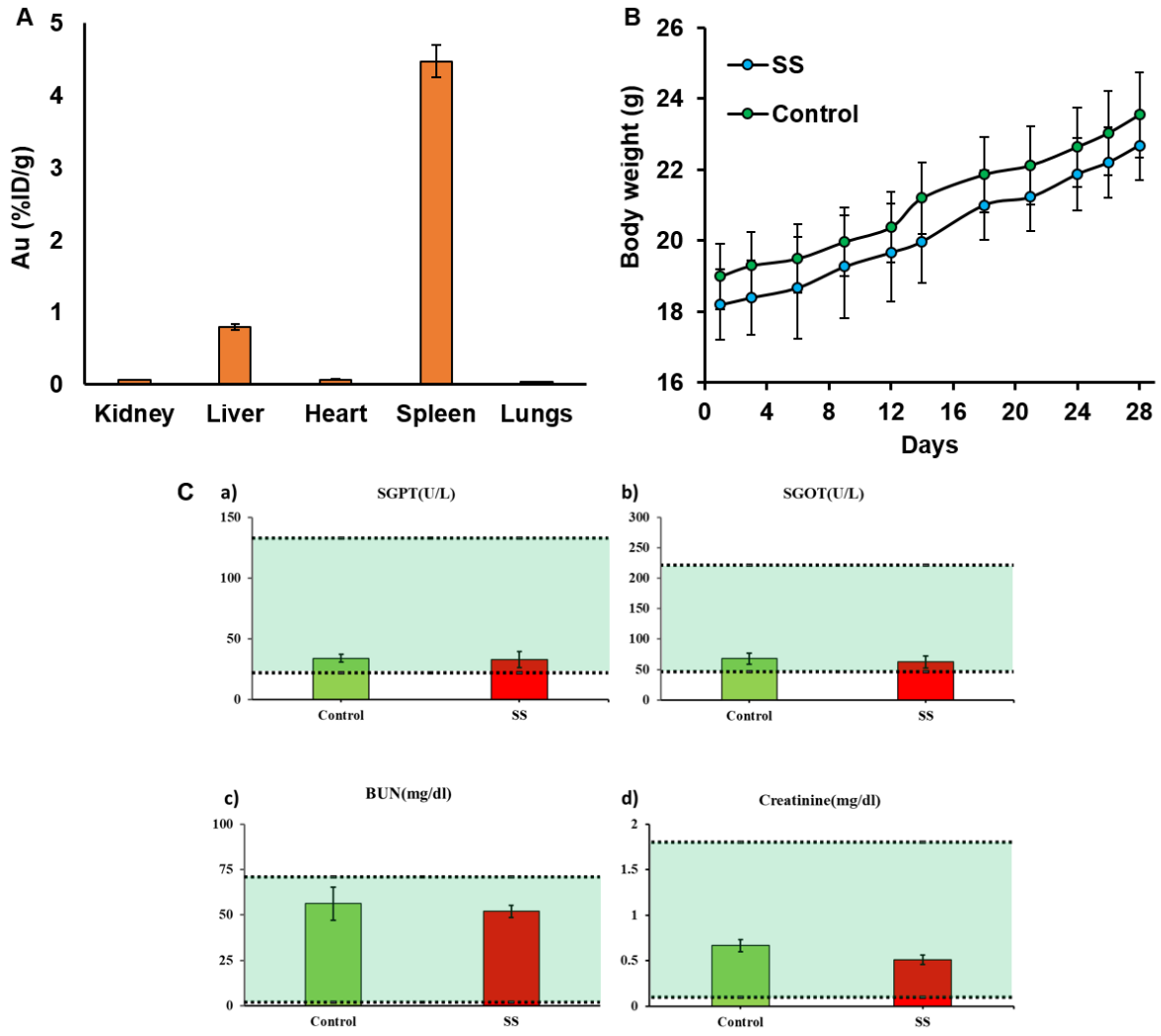

Fig 3.3: (A) *In-vivo* biodistribution of PEGylated SS post intravenous injection at day-28; (B) Body weight (g) of Control and SS injected mice over period of 28 days; (C) Serum biochemical analysis for determining vital organ functioning through a) SGPT b) SGOT c)Blood urea nitrogen (BUN) and d) Creatinine at day-28.

3.2.2. Photothermal therapy of metastatic breast tumors with SS

Preliminary assessment of SS for photothermal therapy was performed against triple negative breast cancer MDA-MB-231 cells at 100 µg/mL concentration and different 808 nm laser irradiation time. While there was irradiation time dependent toxicity of observed, 5 minutes was found to be optimal duration (**Fig 3.4A**). Further, live/dead assay indicated > 95 % non-viable cancer cells when SS is combined with laser, in comparison to the blank and laser controls with > 95 % viable cells. Interestingly, material control (SS alone) caused cellular clumping with > 30 % of dead cells (**Fig 3.4B**).

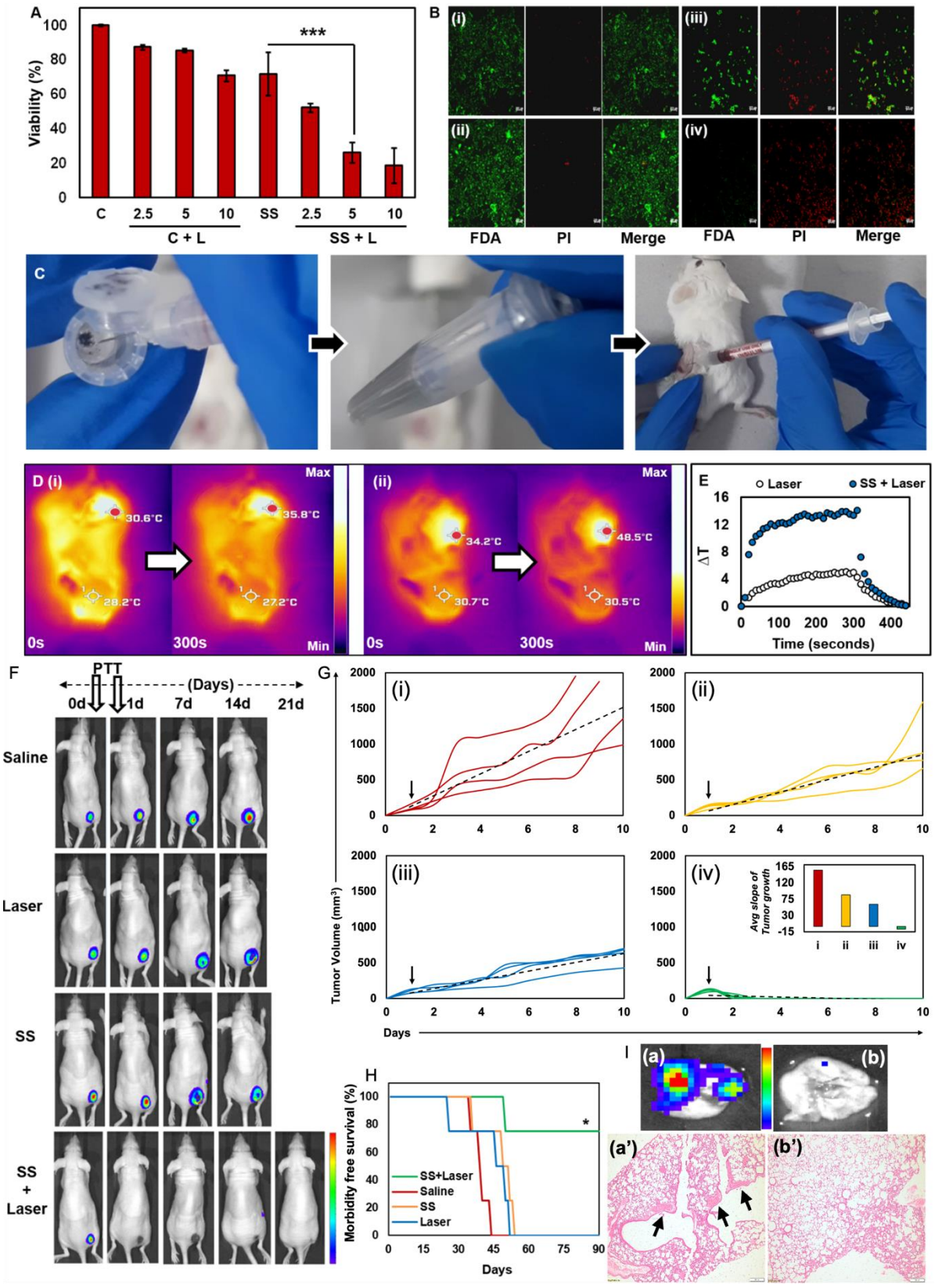

Fig 3.4: A) Irradiation time dependent photothermal toxicity of SS in MDA MB 231 cells (*p<0.001); B) Live/dead staining of cells in control (scale bar-200 µm (i), 5 minutes laser alone (ii), SS alone (iii) & SS + 5 minutes laser (iv) groups; C) Reconstitution & intra-tumoral administration of SS in 4T1 tumor bearing Balb/c mouse; D) Thermal**

images of representative mouse in laser (i) & SS + laser (ii) groups; E) Temperature profile obtained from (D); F) Periodic bioluminescence imaging of representative 4T1 FL2 tumor bearing CD1 nude mice in control groups (n=3) and SS + laser group (n=5); G) Time dependent change in 4T1 tumor volume in saline (i), laser alone (ii), SS alone (iii) & SS + laser (iv) groups of Balb/c mice (Arrow indicate day of treatment; inset in [iv] show tumor growth slopes); H) Kaplan Meier survival analysis of mice in control and treatment groups (n=4) (*p<0.05 for individual control groups Vs SS+Laser); I) Ex vivo bioluminescence imaging of representative lungs in saline (a) and SS + laser (b) groups post autopsy and the micrographs of haematoxylin & eosin stained sections in these two groups post survival analysis (a' & b') (black arrows indicate metastatic tumor lesions).

As this extent of toxicity was not observed at same concentration in highly sensitive normal HUVEC cells, the cancer specific toxicity could be due to the glutathione depleting effect of gold nanoparticles [28]. Proceeding forward for evaluation in preclinical tumor models, the ability of SS for on-demand reconstitution in saline for *in vivo* administration and photothermal ablation was confirmed (**Fig 3.4C**). The combination of SS and 808nm laser irradiation provided ~ 14 ^{o}C rise in temperature as compared to only ~5 ^{o}C with laser control (**Fig 3.4D and Fig 3.4E**). The achieved temperature rise is well within the hyperthermic window for irreversible tissue damage associated with microvascular thrombosis, ischemia, and hypoxia [29].

The phototherapeutic effect of SS was evaluated in 4T1 FL2 tumor bearing CD1 nude mice for up to 21 days. The mice subjected to intra-tumoral injection of SS followed by two independent laser irradiation at day-0 and day-1, showed a drastic drop in the tumor bioluminescence signal within first 24 hours (**Fig 3.4F**).

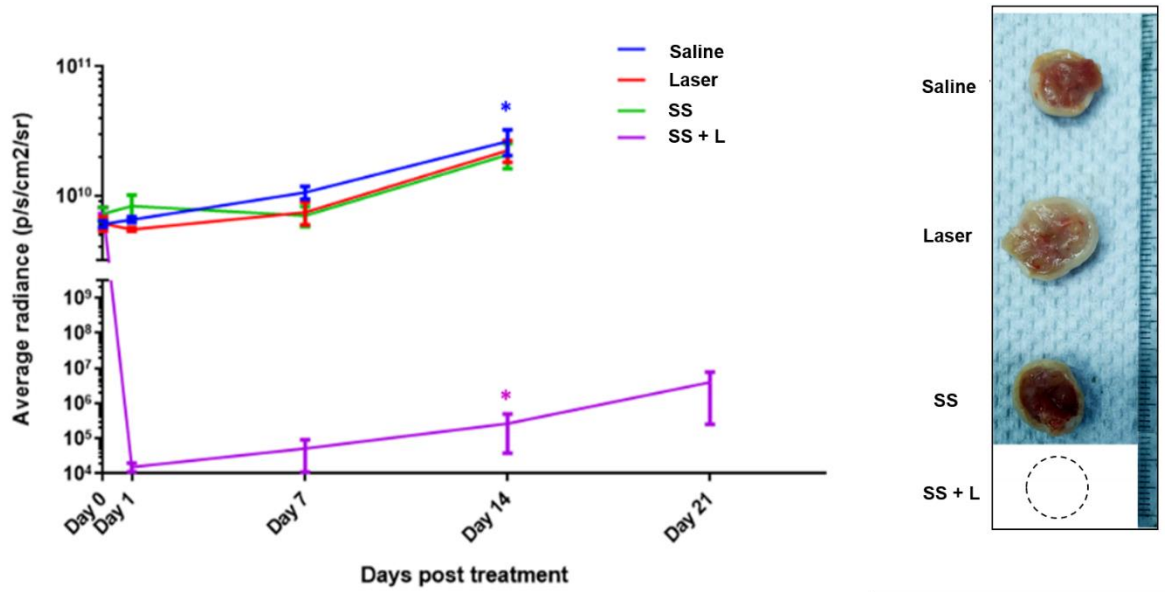

Fig 3.5: Change in bioluminescence signal of 4T1 FL2 tumor grafted on CD1 nude mice post treatment with C (Saline), C+L (Laser), SS and SS+L (SS+Laser) and representative tumors excised from each group post sacrifice. (* p<0.05 using Students' t-test)

However, the control groups continued to show increase in the tumor growth as assessed by the bioluminescence (**Fig 3.5**). While the photothermal treatment group showed complete ablation of the primary tumor, the control groups were sacrificed at day-14 due to their tumor burden. There was no obvious recurrence in the bioluminescence at the primary inoculated site on the mice within the phototherapeutic group for up to 21 days. While peripheral bioluminescence was observed near the inoculated site, possibly arising from sentinel lymph node, the mice were observed to be free from spontaneous metastatic lesions in lung (**Fig 3.4I**

a & b and **Fig 3.6**). Contrastingly, the control groups showed severe metastasis to both lung and chest bone.

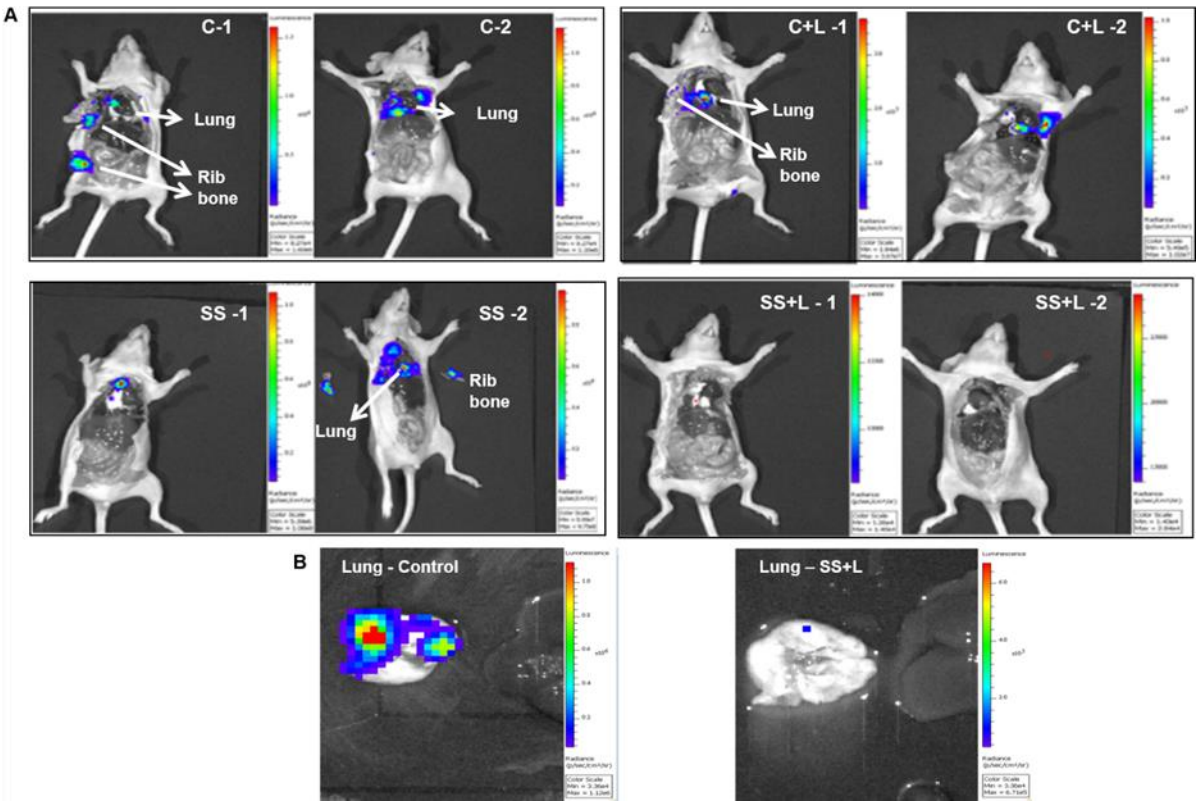

Fig 3.6: (A) Bioluminescence imaging of representative mice from saline (C1 & C2), Saline+Laser (C+L-1 and C+L-2), semi shells (SS-1 & SS-2 and semi shell + Laser (SS+L-1 & SS+L-2) groups with arrows tracing to presence of tumor in lung and rib bone. (B) Bioluminescence imaging of lung from representative mice in saline control and SS+L groups.

The average growth of 4T1 tumor over 10 days post treatment indicated steeper and positive slopes in control groups corresponding to rapid proliferation (**Fig 3.4G i-iii**). Nevertheless, the photothermal therapy group showed deceleration in the tumor growth as observed from the negative slope (**Fig 3.4G iv**). Subsequently, this complete ablation of primary tumor significantly improved the survival of the mice with 75 % mice persisting up to 90 days post treatment without any recurrence event (**Fig 3.4H** and **Fig 3.7**).

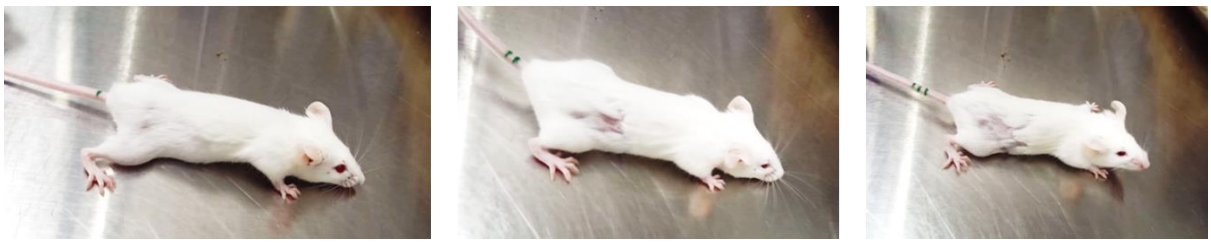

Fig 3.7: Tumor free mice (75% relapse-free survival; n=4) at the end of 3 months post photothermal treatment.

Post 90 days, thee histopathological analysis with hematoxylin & eosin staining of representative lung sections from saline group indicated several metastatic lesions within the pulmonary alveolar space and tumor cell aggregation in the parenchyma in addition to thickening of the pleural lining. However, the obliteration of primary tumor in the PTT group suppressed the spread of tumor cells to lung as seen from its normal morphology (**Fig 3.8**).

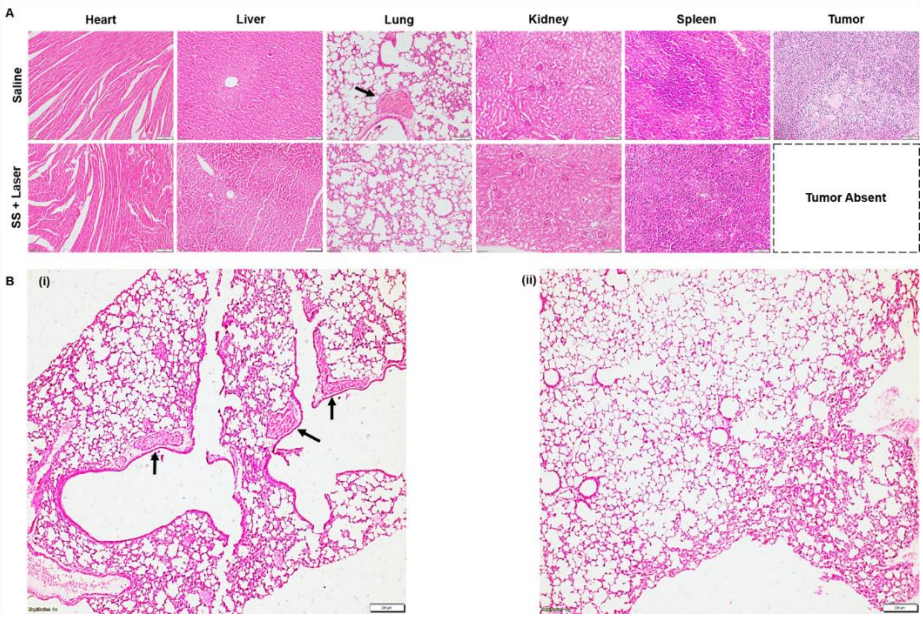

Fig 3.8: A) Microscopic images of haematoxylin & eosin stained sections of vital organs and tumor in saline and SS+Laser treated mice; B) Low magnification microscopic images of haematoxylin & eosin stained lung sections from saline (i) and SS+Laser (ii) groups. Black arrows in A and B indicate metastatic tumor lesions in lung sections.

3.3. Conclusions and Future Prospects

The PEG stabilised SS were found to have profound potential for photothermal therapy of cancer cells. The SS were found to be hemocompatible with excellent *in-vivo* safety. The breast tumor regression studied in CD1 nude mice model indicated efficient inhibition of the primary tumor load along with lung and bone metastasis. This local and systemic anti-tumor effect

allowed 75% relapse-free survival of mice for up to a period of 3 months. The chances of survival are further expected to increase with the use of combinatorial chemo/photothermal therapy. Hence, the SS mediated PTT holds immense potential for translation in a clinical setup due to their high photothermal transduction efficiency, non-inflammatory and safe sub-acute dosage as well as excellent tumor regression and metastasis inhibition with prospects of relapse free survival.

References:

[1] I. E. Elkholi, A. Lalonde, M. Park, and J.-F. Côté, "Breast Cancer Metastatic Dormancy and Relapse: An Enigma of Microenvironment(s).," *Cancer Res.*, vol. 82, no. 24, pp. 4497–4510, Dec. 2022.

[2] H. Kennecke *et al.*, "Metastatic behavior of breast cancer subtypes.," *J. Clin. Oncol. Off. J. Am. Soc. Clin. Oncol.*, vol. 28, no. 20, pp. 3271–3277, Jul. 2010.

[3] Y. Kang *et al.*, "A multigenic program mediating breast cancer metastasis to bone.," *Cancer Cell*, vol. 3, no. 6, pp. 537–549, Jun. 2003.

[4] A. J. Minn *et al.*, "Genes that mediate breast cancer metastasis to lung.," *Nature*, vol. 436, no. 7050, pp. 518–524, Jul. 2005.

[5] R. S. Riley and E. S. Day, "Gold nanoparticle-mediated photothermal therapy: applications and opportunities for multimodal cancer treatment," *WIREs Nanomedicine and Nanobiotechnology*, vol. 9, no. 4, p. e1449, Jul. 2017.

[6] M. A. Dheyab *et al.*, "Gold nanoparticles-based photothermal therapy for breast cancer," *Photodiagnosis Photodyn. Ther.*, vol. 42, p. 103312, 2023.

[7] Y.-C. Chuang, H.-L. Lee, J.-F. Chiou, and L.-W. Lo, "Recent Advances in Gold Nanomaterials for Photothermal Therapy," *Journal of Nanotheranostics*, vol. 3, no. 2. pp. 117–131, 2022.

[8] D. S. Chauhan *et al.*, "Enhanced EPR directed and Imaging guided Photothermal Therapy using Vitamin E Modified Toco-Photoxil," *Sci. Rep.*, vol. 8, no. 1, p. 16673, 2018.

[9] N. Gong *et al.*, "Carbon-dot-supported atomically dispersed gold as a mitochondrial oxidative stress amplifier for cancer treatment," *Nat. Nanotechnol.*, vol. 14, no. 4, pp. 379–387, 2019.

[10] Y.-N. Zhang, W. Poon, A. J. Tavares, I. D. McGilvray, and W. C. W. Chan, "Nanoparticle–liver interactions: Cellular uptake and hepatobiliary elimination," *J. Control. Release*, vol. 240, pp. 332–348, 2016.

[11] C. Brace, "Thermal tumor ablation in clinical use.," *IEEE Pulse*, vol. 2, no. 5, pp. 28–38, 2011.

Chapter 4

Preclinical Safety Assessment of Host-Specific Gold Quantum Clusters Stabilized with Autologous Serum Proteins for Cancer Radiosensitization

4. INTRODUCTION

With the widespread exploration of nanotechnology in the healthcare industry, novel multifunctional nanomaterials have been developed for the simultaneous diagnostic and therapeutic applications. One such class of nanomaterials is photoluminescent protein stabilised noble metal quantum clusters that have recently gained a lot of attention due to their ability to be used for simultaneous theranostic applications as well as their high biocompatibility. The protein stabilised metal quantum clusters are typically packed as core-shell type or metal-ligand type nanostructures wherein the protein shell acts as a scaffolding template as well as capping/stabilising agent for the metallic atoms such as Au, Ag, Cu, Pt. The bonding between the core metal atoms and the protein is usually through thiol containing amino acids like cysteine and is sterically protected due to the bulkiness of the protein [1]. Thus the resulting protein stabilised metal nanoclusters depict smaller sizes (typically less than 3 nm) which in-turn confers them with a unique ability of photoluminescence due to quantum confinement.

Due to their high biocompatibility, high photoluminescence, improved pharmacokinetics and fairly good *in vivo* clearance, AuQCs have been utilised in a wide variety of biological applications like cancer therapeutics including image guided therapeutics[2], [3] , drug delivery[4] [5], and tumor targeting[6], [7]. Radiation therapy is a very cost-effective cancer treatment as well as an efficient means of palliative care and is administered in ~50% of cancer patients [8][9]. Upon irradiation, the cancer cells are attenuated due to oxidative stress leading to cell membrane, protein and DNA damage. However, the healthy surrounding tissues and vital organs are also affected in the process. Hence, in order to enhance the selectivity of killing the cancer cells over the normal healthy cells, radiosensitizers such as AuQCs are being explored during radiation therapy[10]–[15]. The radiotherapy enhancement comes from the strong photoelectric absorption coefficient of gold nanoparticles wherein they receive the incoming high energy γ rays photons and the energy is transferred through scattered photons,

Compton electrons, photoelectrons, electron-positron pairs, and Auger electrons thereby leading to formation of free radicals such as ROS within cellular entities and leading to the killing of cancer cells [16]. Apart from being effective radiosensitisers, atomically precise AuQCs have the advantage of high tumor uptake[13], [17] and well established renal clearance[10], [18], [19].

AuQCs have been previously fabricated using a wide range of proteins such as albumin[1], [20], trypsin[21], horseradish peroxidase[22], chymotrypsin[23], keratin, peptides [24]–[26], insulin[27] as well as small biomolecules like cysteine[28], [29] and glutathione[17], [30]. However, the reports for mixed protein stabilised AuQCs are limited. A mixture of lysozyme and albumin was utilized to enhance photoluminescence quantum yield of AuQCs due to Förster resonance energy transfer (FRET) between both the proteins [31]. AuQC have also been synthesised using inexpensive naturally occurring proteinaceous sources such as chicken egg whites (CEW) [32]–[34]. Chicken egg whites are complex mixed protein systems consisting of about 141 proteins including ovalbumin, ovotransferrin, ovomucoid, and lysozyme. CEW stabilized AuQCs have been utilised for developing an inexpensive H_2O_2 biosensor [32] as well as for selective and sensitive detection of Hg(II) ions [35]. Another such complex multi-protein system is serum, which has not been explored for AuQC synthesis till now. Human serum, essentially without the clotting factors, possesses a rich pool of proteins hypothetically with potential to directly stabilize AuQCs. Serum typically consists of proteins – predominantly albumin (up to 70%), globulins and lipoproteins in addition to small biomolecules such as glucose and creatinine. Recent study utilized host derived serum protein to form nanovesicles for patient specific nanomedicines [36]. Our group recently showed that drug nanocrystals can be directly stabilized with autologously derived serum proteins for cancer therapy [37]. This approach takes advantage of the endogenously derived proteins that are less likely to cause inflammatory response in addition to being eventually metabolized safely by the body. Taking cues from this prior knowledge, we have fabricated AuQCs stabilized with whole serum proteome (Au-QC-NanoSera: QCNS) from bovine, murine and human origins. Acute toxicity, biodistribution and clearance of autologously derived QCNS in in-bred C57BL/6 mice were studied to establish their safety for potential in vivo applications. As a proof of concept, we have also demonstrated the capability of the QCNS to act as radiosensitizers.

4.1. Experimental Section

4.1.1. Materials

Gold (III) chloride trihydrate (520918; Sigma), fetal bovine serum (FBS, RM9955-heat inactivated; Himedia), bicinchoninic acid (BCA) protein assay kit (71285-3; Sigma), MTT (Thiazolyl blue tetrazolium bromide) dye for cell culture (TC191; Himedia), bovine serum albumin (BSA; Himedia), nuclear staining dye- bisBenzimide H33342 trihydrochloride (Hoechst 33342, B2261; Sigma), cytoskeletal staining dye- Phalloidin Tetramethylrhodamine B isothiocyanate (Phalloidin-TRITC, P1951; Sigma), standard lipopolysaccharide from *E. coli* 0111:B4 strain; TLR4 ligand (TLRL-EBLPS; InvivoGen). All other chemicals were of analytical grade and were used without further purification unless mentioned otherwise. Ultrapure water (~18.2 MΩ) was used for AuQC synthesis.

4.1.2. Instrumentation

UV-Visible absorption spectra were recorded on Shimadzu UV-Vis spectrophotometer using 1 mL quartz cuvette. Fluorescence spectroscopy and TCSPC analysis was carried out using Fluorolog 3-221 fluorimeter equipped with 450 W Xenon lamp. Dynamic light scattering (DLS) and Zeta potential measurements were performed on Malvern Zetasizer Nano ZSP instrument. TEM measurements were performed using JEOL JEM-2100 at an accelerating voltage of 120 kV. Circular Dichroism was performed using J-15 model CD Spectrometer. XPS was carried out at CSIR-CECRI. Radiation exposure was carried out using Gamma radiator- Bhabhatron-II (Panacea Engineering Medicine) at INMAS, New Delhi. MALDI-TOF analysis was carried out at IIT-Bombay using Sinapinic acid (SA) and 2,5-Dihydroxybenzoic acid (DHB) matrix at 1:1 ratio.

4.1.3. Synthesis of serum stabilized gold quantum cluster (Au-QC-NanoSera: QCNS)

QCNS synthesis: Quantum clusters stabilized with whole serum proteome from bovine, murine and human origins were synthesized as per previously reported method [1]. Firstly, serum was quantified for total protein content using BCA Kit. Further, 5 mL of 50 mg/mL protein equivalent of serum was aliquoted in a clean glass vial and was allowed to pre-incubate at 37 °C for 15 mins. Aurochloric acid (10 mM, 5 mL) was added drop wise to the serum under high stirring (1000 rpm) and were allowed to incubate for 2-3 mins followed by adjusting the pH to ~11 using 1 M NaOH. The reaction was allowed to proceed for 24 hours in dark and sterile conditions. The QCNS thus formed were dialysed (MW cut off: 2000-14000 kDa) against ultrapure water for about 24 h and were stored at 4 °C for immediate analysis or lyophilized for long term storage. Post synthesis, bovine serum derived QCNS were used for

all characterization including *in vitro* biocompatibility and radiosensitization studies. They were also used for evaluation of photoluminescence and size on a 1.5% agarose gel under UV-transilluminator using albumin stabilized AuQCs as a standard.

Human serum was used to showcase their ability to form H-QCNS. Healthy human serum was utilised after obtaining approval from the institutional ethics committee of PGIMER (PGI/IEC/2020/000787). For collection of human serum samples, 5 mL blood was drawn from a healthy individual with prior informed consent. The blood was allowed to clot for 20-25 mins at room temperature and the samples were centrifuged at 5000 rpm for 10 mins at 4 °C. The serum was obtained as the supernatant and was stored at -20 °C in multiple aliquots until further use.

Murine serum was used to evaluate acute toxicity, biodistribution and clearance of autologously derived M-QCNS in in-bred C57BL/6 mice. Healthy mice serum was utilised after obtaining approval from the institutional ethics committee of IISER Mohali (IISERM/SAFE/PRT/2020/001). Collection and processing is explained in later section.

4.1.4. Hemocompatibility studies

Hemocompatibility is one of the most critical parameters for design and safety evaluation of any nanomaterial, especially those injected intravenously. QCNS was challenged against red blood corpuscles derived from healthy human donor. Briefly, 5 mL blood was collected in a sterile vial pre-treated with trisodium citrate. 150 µL RBCs were incubated for 3 hours with 750 µL QCNS at different concentrations (12.5, 25, 50, 100 µg/mL in PBS) at 37 °C under mid shaking after which the RBCs were centrifuged [5000 rpm, 10mins at 4°C] to separate the lysed cellular component and the supernatant was evaluated for haemolytic activity. Milli-Q water and PBS were used as positive and negative controls for the assay. The experiment was performed in triplicates. The amount of hemoglobin was calculated by the following formula:

$$\text{Amount of plasma Hb (mg/dL)} = 0.076[2(A_{415}) - (A_{380} + A_{450})] * D.F$$

herein the abbreviations: A_{380}, A_{415}, and A_{450} refers to the absorbance values at 380 nm, 415 nm and 450 nm, respectively while D.F is the dilution factor. The hemolysis percent was calculated by the following equation:

$$\% \text{ Hemolysis} = \frac{Plasma\ Hb_{\ (test\ sample)}}{Plasma\ Hb_{\ (whole\ blood)}} * 100$$

where plasma $Hb_{\text{ (test sample)}}$ and plasma $Hb_{\text{ (whole blood)}}$ correspond to the plasma hemoglobin value of test samples and the whole blood respectively.

The treated RBCs were fixed in 4% PFA solution and washed with PBS twice and dropcasted on a Si wafer for assessing their morphological analysis under SEM.

4.1.5. Cellular studies

The cellular uptake and biocompatibility analysis of QCNS were carried out with murine fibroblast L929 cells. The radiosensitization studies were carried out using PLC/PRL/5 hepatoma cells at Institute of Nuclear Medicine and Advanced Science (INMAS), New Delhi. Both L929 and PLC/PRL/5 were cultured in DMEM (10% FBS and 1% antibiotic solution added as supplement) in an incubator at 37 °C and 5% CO_2 with bi-weekly sub-culturing maintenance.

4.1.6. *In-vitro* biocompatibility

For assessing the *in-vitro* biocompatibility of QCNS, normal murine fibroblast L929 cells were seeded at a density of 5.0 $x10^4$ cells in a 96 well plate for 24 h at 37 °C and 5% CO_2. After reaching ~70% confluency, different concentrations of QCNS (0, 25, 50, 100 µg/mL) were incubated with the cells for 24 h. Next day, the cells were washed with 1X PBS. Further, 10 µL of MTT solution (5 mg/mL dissolved in PBS) diluted with 90 µL media was added and allowed to incubate for 4 h. Once the colour changed, the media was carefully removed and 100 µL of DMSO was added to each well and mixed properly until the purple formazan crystals were dissolved. The absorbance was recorded at 595 nm on a multimode plate reader. Cell viability percentage was calculated using the formula:

$$\text{Cell viability } \% = \frac{\text{Absorbance of sample at 595nm} \times 100}{\text{Absorbance of control at 595nm}}$$

4.1.7. Intracellular localisation study

To check the cellular uptake of QCNS, L929 cells were seeded on a cover slip at a density of $5x10^4$ cells per well in a 6 well plate for 24 h. Next day, QCNS was added at concentration of 300 µg/mL and incubated for 24 h. The cells were further washed with 1x PBS thrice and fixed with 4% paraformaldehyde for about 15 mins. Next, the cellular nuclei were stained with nuclear staining dye (Hoechst 33342) for 10 minutes. After washing with PBS twice to remove the excess stain, the cells were mounted on the top of a glass slide and analyzed under CLSM.

4.1.8. *In-vitro* radiosensitization studies

QCNS were investigated as a potent radiotherapy sensitizer on PLC/PRF/5 hepatoma cells. Briefly, $1x10^4$ cells were seeded and allowed to adhere overnight in a 96 well plate. The following day, the cells were treated with QCNS at 100 µg/mL and 50 µg/mL concentrations

and incubated for 24 h. Next day, the cells were exposed to differential γ-radiation doses (0, 0.625, 1.25, 2.5 and 5 Gy) and further checked for cell viability using MTT assay. The experiment was performed in triplicate and the results were plotted as cell viability (percent of control).

4.1.9. Assessment of γ-radiation induced reactive oxygen species

In order to assess the ROS generated due to QCNS catalysed radiosensitization, DCFDA assay was carried out. Dichlorodihydrofluorescein diacetate acetyl ester or H2DCFDA (a cell permeant non-fluorescent dye) is converted into its highly green fluorescent form 2',7'-dichlorofluorescein or DCF form after the removal of acetate groups by intracellular esterases and oxidation in the presence of ROS species. The green fluorescent signal is quantified *in-vitro* and is directly proportional to ROS species produced.

Briefly, PLC/PRF/5 cells were seeded at a density of $1x10^4$ cells/well in a 96 well cell culture plate and after allowing cells to adhere overnight they were treated with 100 µg/mL QCNS. The cells were irradiated with 5Gy γ-rays on the following day. After irradiation, the cells were washed with PBS and were left to incubate with DCFDA (25 µg/mL) in serum free media for around 4 h. The fluorescence intensity of DCF (exc: 485 nm and em: 535 nm) was recorded at the start (0 min) and end point of the experiment (240 mins). The experiment was performed in triplicates and the results were plotted with respect to control.

4.1.10. Assessing cellular damage post-radiation therapy

PLC/PRF/5 cells were seeded at a density of 5×10^4 cells/well in a 6 well plate on cover slips. After adherence, the cells were incubated with 100 µg/mL QCNS for 24 h. This was followed by γ-ray irradiation of cells at a dose of 5 Gy. The cells were then washed in PBS twice to remove any traces of treatment and were fixed with 4% PFA for 10 mins at room temperature. Post-fixing, the cells were washed in PBS once to remove the excess PFA and the cellular nucleus was stained with Hoechst 33342 (2 µg/mL) for 15 min, followed by counterstaining the cytoskeleton with Phalloidin-TRITC for 20 min. The cells were washed twice with PBS to remove excess stain and mounted on to the cover slips. The nuclear and cytoskeletal damage were observed with a confocal laser scanning microscope (Carl Zeiss LSM 880, Germany) at 63x magnification.

4.1.11. Animal experimentation

All the experimental procedures using laboratory animals were conducted with the approval of the Institutional Ethics Committee (IISERM/SAFE/PRT/2020/001) at IISER Mohali. For the biodistribution study, C57BL/6 female mice aged 6-8 weeks were divided in 7 groups with

equal average weights (n=3): Control Day-1, Control Day-28, Untreated autologous serum Day-1 and Untreated autologous serum Day-28, M-QCNS Day-1 and M-QCNS Day-28 and Lipopolysaccharide Day-1. The mice were housed in cages that were located in a well-ventilated, temperature-controlled room with a light and dark period of 12 h each, with free access to water and food. Two weeks (i.e., **D_{-14}**) prior to treatment, blood was collected from all the in-bred mice and serum was pooled (~2 mL) for the synthesis of M-QCNS. On day 0 **(D_0)**, the mice were intravenously injected with single dose of M-QCNS (50mg/kg; Au 5mg/kg) or saline or untreated autologous serum or LPS (2mg/kg; positive control for acute inflammation). On day 14 **(D_{14})**, a second dose of saline, QCNS or untreated autologous serum was administered in the respective group. On day 1**(D_1)** and day 28 **(D_{28})**, mice from each group were sacrificed for assessing acute inflammatory response and sub-acute toxicity respectively. Blood was collected and the serum was stored at -80°C for further biochemical analysis. Vital organs such as liver, spleen, kidneys, lungs and heart were extracted for biodistribution and histopathological analysis.

4.1.12. Assessment of M-QCNS biodistribution

Vital organs including liver, spleen, lung, kidney, heart as well as excretory (faeces) samples were analysed for their Au content by treating them with ICP-MS grade nitric acid and incubated at 60 °C for 12 h. The solutions were then further diluted in deionized water such that an optimum pH 3-5 was obtained and were analysed using inductively coupled plasma mass spectrometer (Agilent 7900) to determine Au concentration against standard calibration curve obtained with solutions of ionic gold from 10 to 500 ppb.

4.1.13. Acute inflammatory analysis

Acute inflammatory analysis was carried out for mice in following groups on day 1 post injection with M-QCNS, LPS and saline. After sacrificing the mice, the serum was separated from the clotted whole blood after 15mins and was analysed for 13 mouse cytokines including IL-1α, IL-1β, IL-6, IL-10, IL-12p70, IL-17A, IL-23, IL-27, MCP-1, IFN-β, IFN-γ, TNF-α, and GM-CSF using a fluorescent bead-based assay (LEGEND plex). These cytokines are majorly expressed by innate immune cells and are critical in understanding acute immune response to a foreign body such as M-QCNS in the systemic circulation.

4.1.14. Biochemical analysis

The serum obtained from blood samples collected at D1 and D28 were analysed for biochemical parameters such as aspartate aminotransferase, alanine transaminase, creatinine and blood urea nitrogen using kits from ERBA Mannheim as per manufacturer's protocol.

4.1.15. Histopathological analysis

Organs were carefully collected, fixed and conserved in 10% buffered formalin solution before paraffin-embedding. 5 µm thick paraffin sections of different organs were then processed manually and stained with haematoxylin and eosin dye. The slides were examined at different magnifications to assess any abnormal tissue microarchitecture under an inverted light microscope.

4.1.16. Statistical Analysis

All graphs were plotted using OriginPro software. ANOVA and Student's t-test were performed for statistical significance analysis and the results were indicated as * $p<0.05$ and ** $p<0.01$ wherever required.

4.2. Results and Discussions:

4.2.1. Characterisation of Au-QCNS

The size of dialyzed bovine derived Au-QCNS (or simply QCNS) was observed to be about 1.9±0.3 nm with a polydispersity index of ~0.2 as characterized using transmission electron microscopy (**Fig 4.1**). High resolution TEM confirmed the d-spacing of ~0.24 nm corresponding to the (111) crystal plane of the face centred cubic (fcc) lattice of metallic gold.

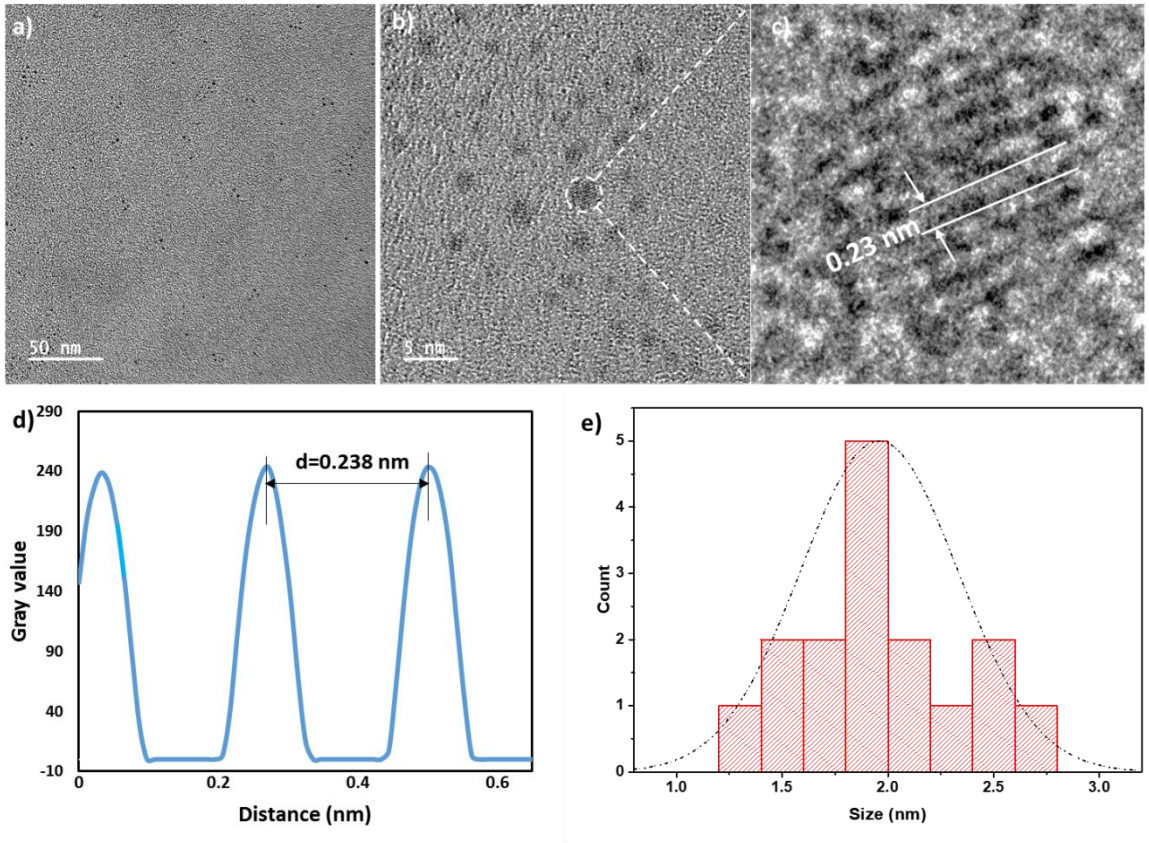

Fig 4.1: TEM micrograph of QCNS in a), b) depicting size distribution; and C) HR-TEM of encircled QC in b) indicating typical Au d-spacing; d) Inverse FFT plot of QCNS and e) Size distribution of QCNSs using data from (a).

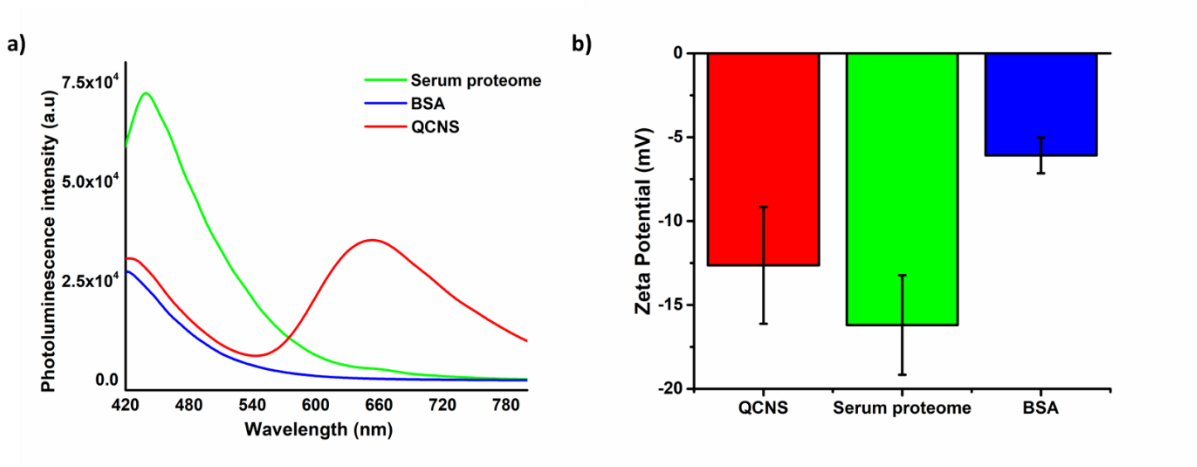

Fig 4.2: a) Photoluminescence spectra (λ_{ex}: 365 nm) and b) Zeta potential of QCNS (red), serum proteome (green) and BSA (blue) respectively.

The absorption spectra of QCNS was devoid any plasmon band typical for larger gold nanoparticles confirming presence of quasi molecular atomic clusters stabilized with serum proteins with a typical peak at ~280 nm due to presence of aromatic amino acid residues- mainly tryptophan and tyrosine (**Fig 4.3 a**). The slight peak in serum proteome at ~ 410 nm is due to haemoglobin that might have been present in the serum sample [38]. There was a time dependant evolution of fluorescence from QCNS with an emission λ_{max} at ~ 660 nm after exciting at 340 nm (**Fig 4.3 b and Fig 4.3 c**) with a quantum yield of ~12.3% as measured with quinine sulphate as reference dye. There was no shift in the excitation dependent emission maxima for QCNS (**Fig 4.3 d**) and the maximum emission intensity was recorded at 330-340 nm. The fluorescence spectra of BSA and serum proteome are also depicted (**Fig 4.2a**). Due to the heterogeneity of the QCNS, agarose gel electrophoresis was carried out where the band pattern was comparable to homogenous albumin stabilized AuQCs (**Fig 4.3 e**). Albumin is the major protein in serum and could possibly dominate reduction of entrapped gold ions to form QCNS at pH~12, over other proteins. The zeta potential for QCNS, serum proteome and BSA were all found to be negative indicating which also indicated similar overall charge (**Fig 4.2 b**).

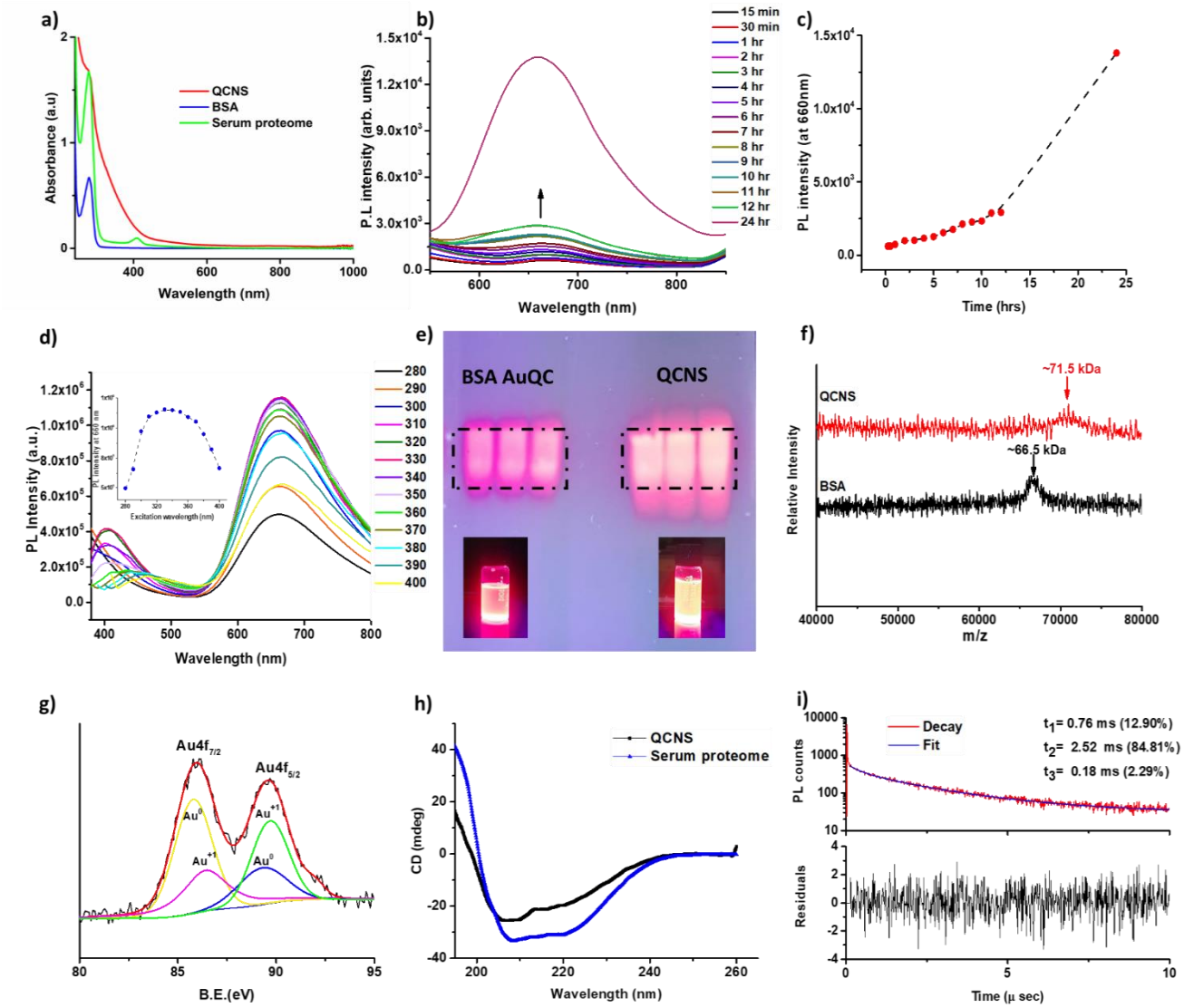

Fig 4.3: Optical characterisation of QCNS: a) UV-Vis absorbance peak in water; b) Time dependant photoluminescence spectra; c) PL intensity at λmax 660 nm as a function of time; d) Excitation dependant emission mapping of QCNS; e) Agarose gel electrophoresis of BSA-AuQCs; f) MALDI-TOF analysis; g) Deconvoluted XPS spectra; h) Circular dichroism analysis; and i) Time-correlated Single photon counting (TCSPC) analysis of QCNS.

The formation of QCNS stabilized predominantly by albumin was further confirmed with MALDI-TOF analysis (**Fig 4.3 f**). QCNS depicted a molecular weight of ~71.5 kDa, which is 5 kDa more than untreated albumin (~66.5 kDa). This difference in the molecular weight corresponds to ~25 atoms of gold present within QCNS, which is similar to the size of BSA-AuQCs [1]. Furthermore, the oxidation state of gold within QCNS was assessed with X-ray photoelectron spectroscopy (**Fig. 4.3 g**). The Au4f spectra was deconvoluted to reveal $Au4f_{7/2}$ peaks centred at 85.81 eV and 86.5 eV corresponding to Au^0 and Au^{+1} which are higher than reported for BSA- AuNCs [1]. This might be attributed to the fact that QCNS contain several

smaller clusters [39] This confirms that QCNS possess the classical core & shell architecture of Au & Au-thiol which is typical of AuQCs. The CD spectra of untreated serum proteome indicated an overall alpha helical conformation (**Fig 4.3 h**). However, with the formation of QCNS, the peaks at ~209 nm descended and peak at ~222 nm ascended, signifying the partial unfolding of conformation due to the newly emerged protein-gold bond and the associated structural rearrangements. These CD peaks at ~209 nm and ~222 nm corresponding to $\pi \rightarrow \pi^*$ and $n \rightarrow \pi^*$ electronic transition respectively are characteristic peaks of BSA [40]. Photoluminescence lifetime of a fluorophore is a measure of the time that it remains in excited state (S_1 or T_1) before emitting the energy in the form of a photon and relaxing back to its ground state (S_0). The fluorescence decay curves for QCNS at ~340 nm revealed the average lifetime to be ~2.24 µs by integrating three components of ζ_1 =0.76 µs (12.9%), ζ_2 =2.52 µs (84.81%) and ζ_3 =0.18 µs (2.29%) (**Fig 4.3 i**). The TCSPC analysis was carried out after dispersing them in ultrapure water. Since the lifetimes were observed to be on the microsecond scale, the emission was predominantly due to phosphorescence[39]. The basic optical properties of both Human derived QCNS (H-QCNS) and Murine derived QCNS (M-QCNS) were comparable (**Fig 4.4** and **Fig 4.7**).

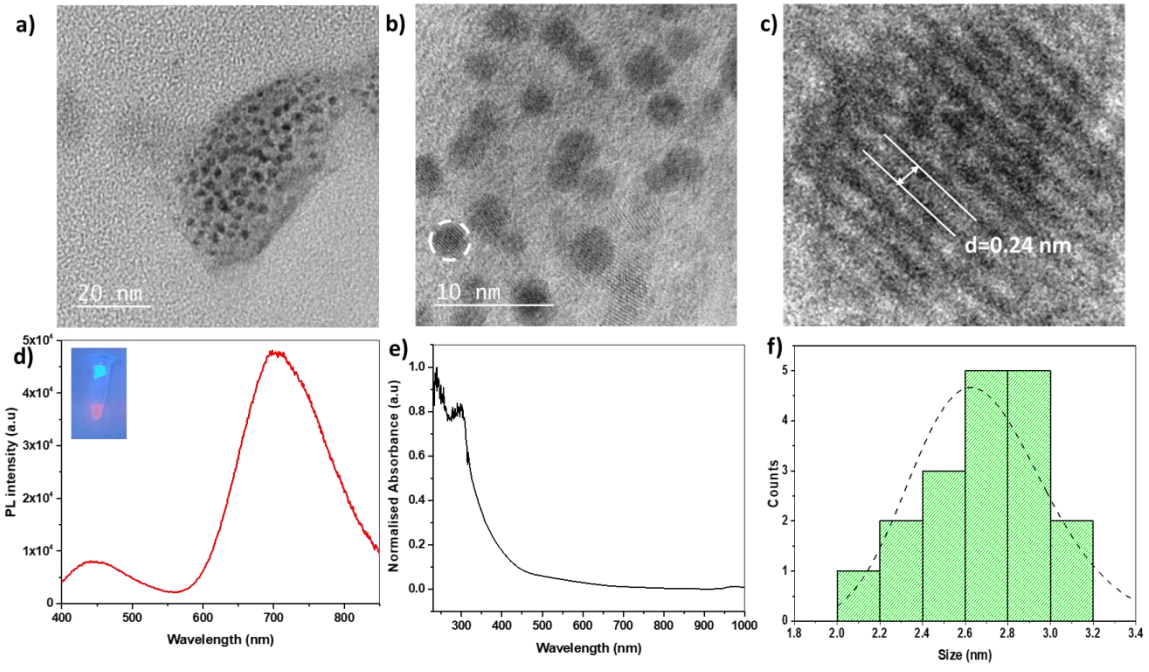

Fig 4.4: H-QCNS characterisation panel: a-b) TEM micrograph of as synthesised H-QCNS at different magnifications c) Magnified view of encircled QC in b) HR-TEM depicting d spacing=0.24 nm Emission spectra of H-QCNS at λex=365 nm (inset) Red fluorescent H-QCNS under UV-chamber d) UV-Vis absorbance f)Size distribution histogram obtained from TEM images depicting H-QCNS size ~2.68±0.3 nm.

4.2.2. Cellular studies

The QCNS were tested up to a concentration of 100 µg/mL against RBCs and found to be highly hemocompatible with <0.3% lysis as opposed to the hemolytic positive control (>5%) (**Fig 4.5a**). The RBCs were also observed to have the QCNS adsorbed onto their surface with no obvious changes in the cellular structure (**Fig 4.5 b**). The toxicity assessment of QCNS against normal fibroblast L929 cells up to a concentration of 200 µg/mL revealed >80% cell viability, indicating their biocompatible nature (**Fig 4.5c**). The cellular uptake of QCNS could be traced through their red emission within the cytoplasm (**Fig 4.5 d**).

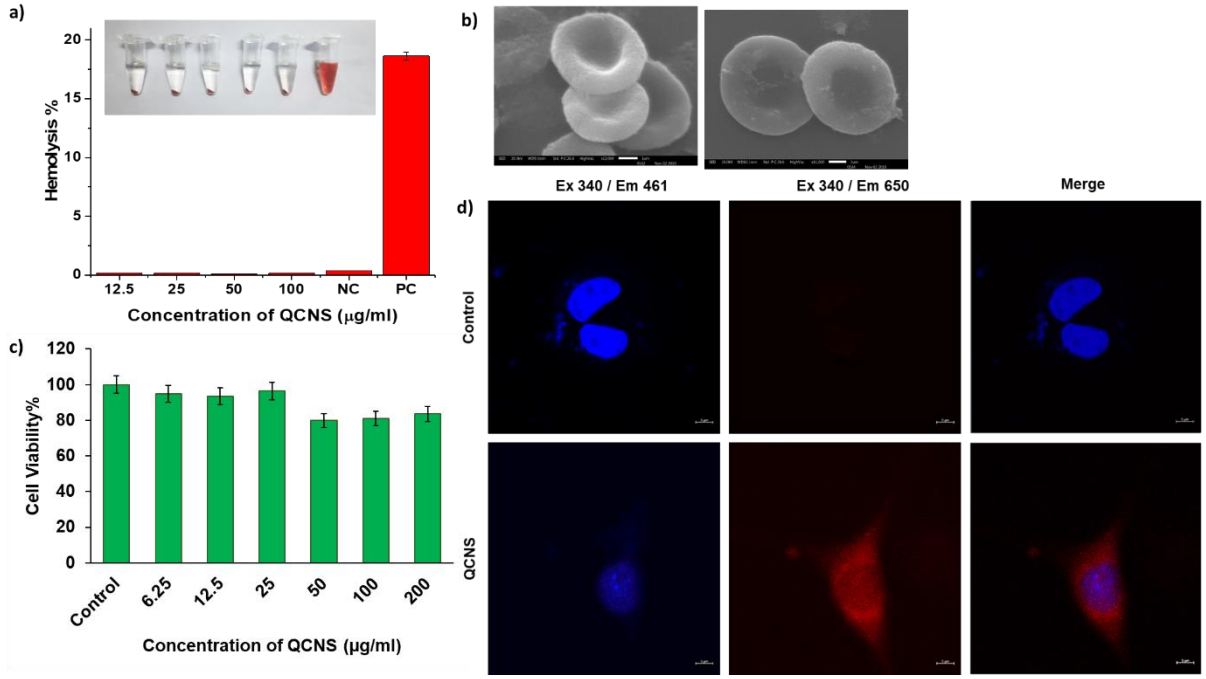

Fig 4.5: a) Hemocompatibility at different QCNS concentration [NC:Negative control; PC: Positive control]; Inset: Photograph showing hemolysis after incubation with different QCNS concentrations b) RBCs after interaction with QCNSs at 12.5 µg/mL and 100 µg/mL respectively c) Biocompatibility at different QCNS concentrations with normal L929 cells d) Red emissive QCNS as observed with confocal uptake (magnification-63x).

We further investigated QCNS as radiosensitizers against PLC/PRF/5 hepatoma cells. **Fig 4.6a** shows a concentration dependant radiosensitisation effect of QCNS at differential γ-radiation doses. At the highest radiation dose of 5Gy for 5mins, less than 10 % cancer cells survived. The IC-50 value was found to be ~ 58µg/mL at 5Gy radiation dose. Further, DCF-DA assay indicated increase in the formation of reactive oxygen species up to 2 folds post radiosensitization with QCNS, in comparison to control (**Fig 4.6 b**). To visualise the effect

caused by QCNS in conjunction with 5Gy radiation on the cellular morphology, we carried out confocal microscopic imaging of treated hepatoma cells stained with Hoechst-33342 and phalloidin-TRITC to analyse DNA and cytoskeleton respectively. As observed in **Fig 4.6c**, the radiosensitized hepatoma cells showed complete destruction of cellular morphology with nuclear shrinkage and condensation in addition to disintegration of actin filaments leading to complete loss of cellular integrity. However, hepatoma cells treated with radiation alone showed minimal nuclear damage with no prominent cytoskeletal damage. These results signify high biocompatibility and significantly enhanced radiosensitization of the QCNS.

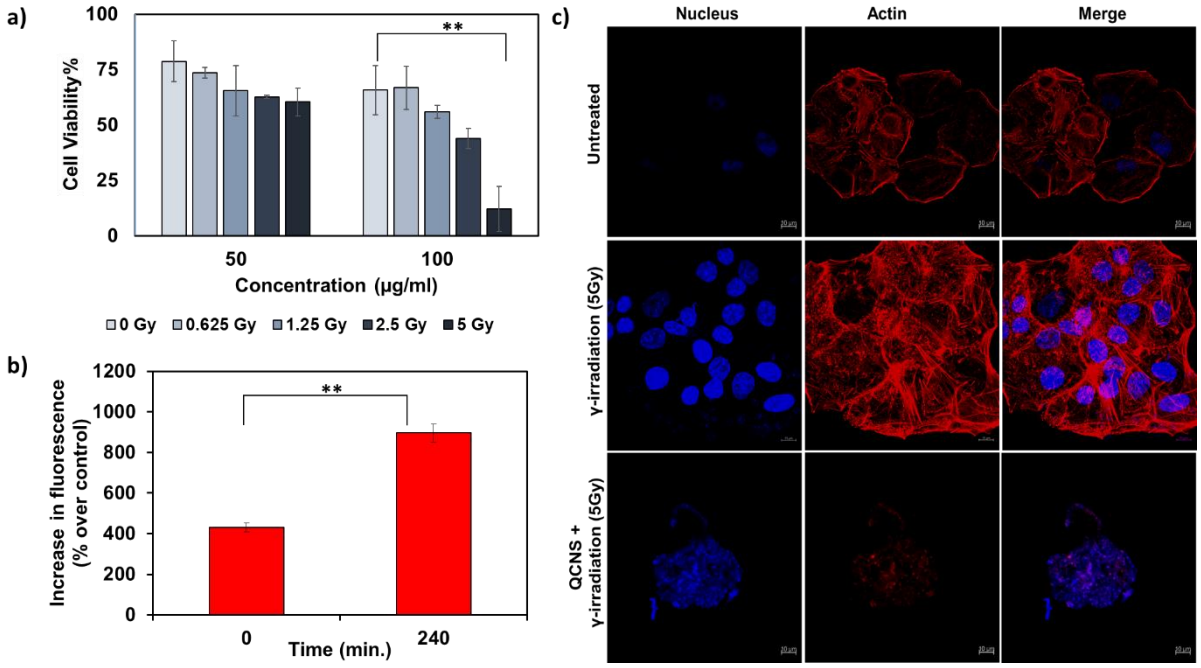

Fig 4.6: *In-vitro* radiation therapy a) Cytotoxicity observed at different radiation doses with 50 and 100 µg/mL QCNS and b) Increase in ROS percentage post radiation treatment c) Confocal images of PP5 hepatoma cells treated with 5 Gy radiation and QCNS+5Gy radiation. ** p <0.01.

4.2.3. Pre-clinical safety assessment and biodistribution of MQCNS

For all animal experimentation, murine derived QCNS (M-QCNS) were prepared as indicated in the methods section. The schedule of treatment is depicted in **Fig 4.8 a**. The characterisation panel of M-QCNS is depicted in **Fig 4.7**.

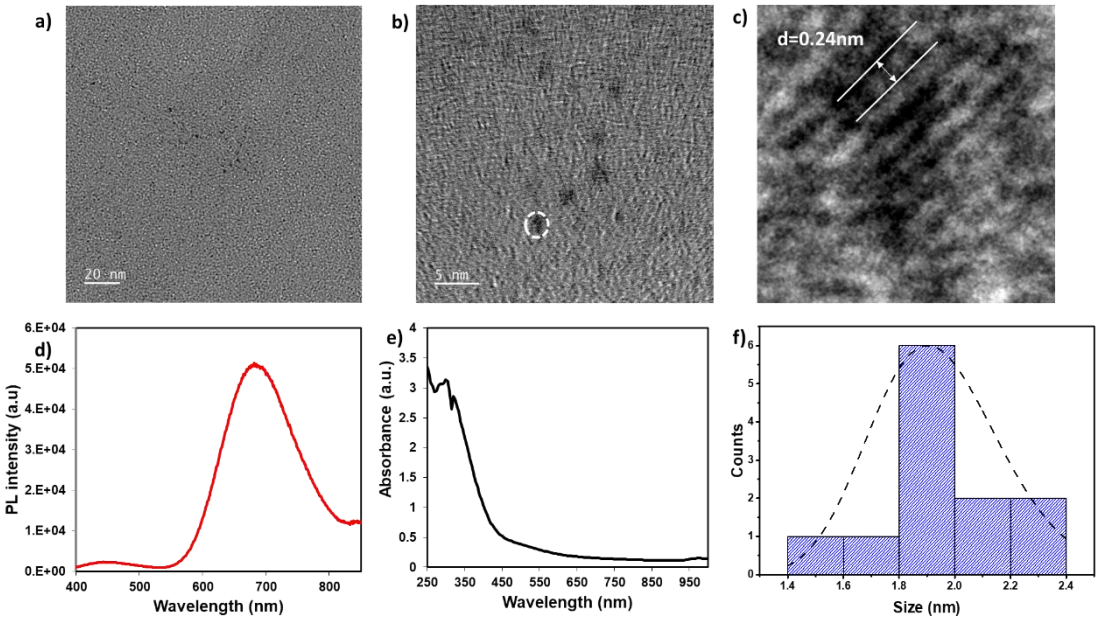

Fig 4.7: M-QCNS characterisation panel: a) and b) TEM micrograph of M-QCNS after negative staining with 1% uranyl acetate at different magnifications c) HR-TEM depicting d-spacing=0.24nm of Au for encircled QC in b) image. d) Emission spectra of as synthesised M-QCNS at λex=365 nm and e) UV-vis absorption spectra depicting no SPR of gold nanoparticles indicating formation of only gold nanoclusters. f) Size distribution histogram obtained from TEM images depicting M-QCNS size ~ 1.94±0.23 nm.

The Biodistribution analysis of M-QCNS post 24 hours of intravenous injection showed predominant accumulation in the liver followed by spleen, kidney and lungs. However, on Day 28, all the organs including liver possessed only marginal quantity (0.08% ID/g for liver and spleen) of MQCNS (**Fig 4.8 b**). While prior reports show that kidney is the most preferred route of excretion for nanoparticles with size less than 6-8nm [41]–[43], albumin stabilized AuQCs is an exception due to its retention from passing through healthy glomerular basal membrane [44]. While there is no single pathway of albumin degradation, most studies have reported that GI tract is a significant site of albumin catabolism (~ 40-70%) in normal individuals [45]. Kidneys also plays a minor role contributing < 15% *in vivo* albumin excretion in healthy individuals even in the absence of a renal disease. Renal catabolism of albumin consists of glomerular filtration and tubular reabsorption. Possible ways of further catabolism of this protein are lysosomal proteolysis to amino acids and short peptides, recycling of degradation products into the bloodstream and tubular lumen or transcytosis of whole molecules[46]. Involvement of liver is also reported contributing <10-15% of albumin catabolism in the body. Hence, no organ can be held majorly responsible for albumin

catabolism. Prior research suggests the possibility of the albumin catabolism to be diffused process which can occur through RES (reticulo endothelial system). These immune cells have the ability to catabolize various proteins and are widely present as residential macrophages in all organs [47]. Damaged protein including albumin are rapidly cleared from the serum via this pathway and blockade of the RES significantly slows the elimination of such altered albumin molecules. Presence of Au in faeces (**Fig 4.8 c**) revealed that QCNS were getting excreted out from body cumulatively estimating to 0.43 % ID/g over a period of first two weeks (Day 1-14) and after second dosage, 0.53% ID/g Au cumulatively over the period of the following two weeks (Day 15-28). Body weight of saline and MQCNS injected mice showed no significant changes and was found to show increase with time depicting normal growth of mice (**Fig 4.8 d**).

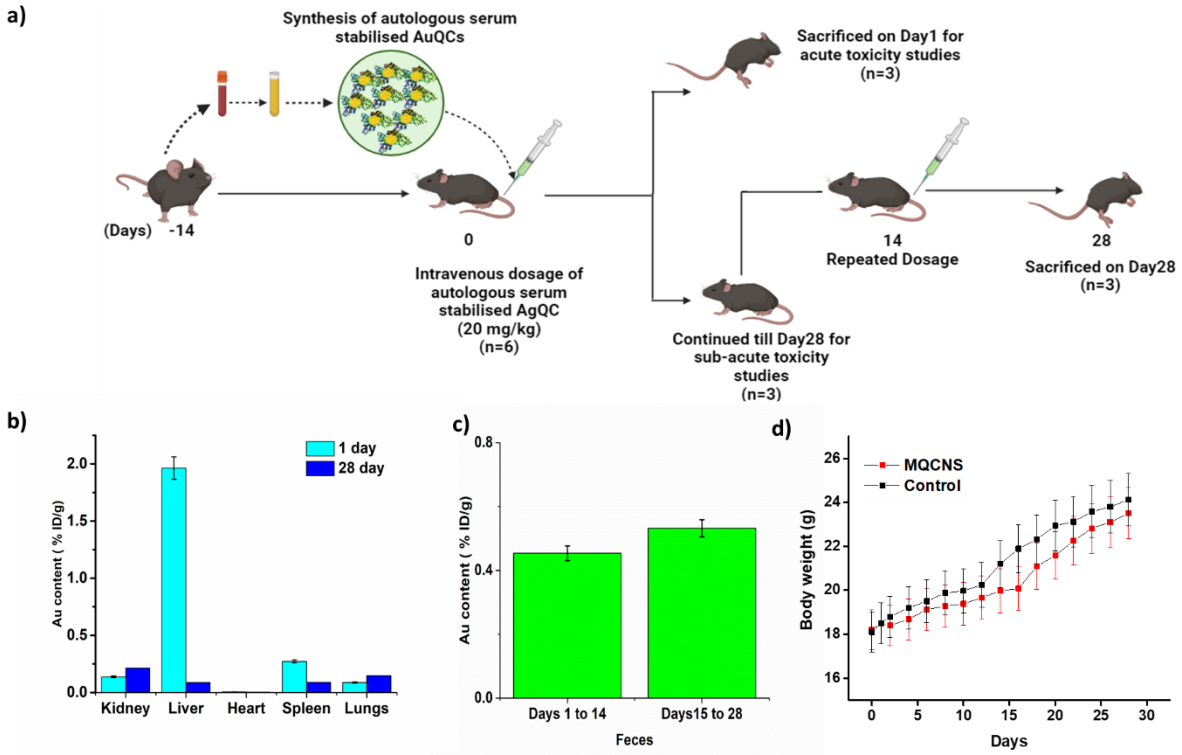

Fig 4.8: Schematic for *in-vivo* dosing for pre-clinical safety and biodistribution analysis; b) - c) Au biodistribution in vital organs and faeces; d) change in body weight vs days.

Acute inflammatory cytokine markers (**Table T1**) that are expressed due to immune responses were assessed on day-1. The results revealed no significant changes in the major inflammatory cytokine levels including TNF-α, IFN-β, IFN-ɤ, IL-6, IL-10, IL-12(p70), IL-1β, MCP-1, IL-23, IL-1α, IL-27, GM-CSF and IL-17A in comparison to positive control (LPS) group as shown in (**Fig 4.9)**. **Table 4.1** depicts the role of these 13 major cytokines in inflammation.

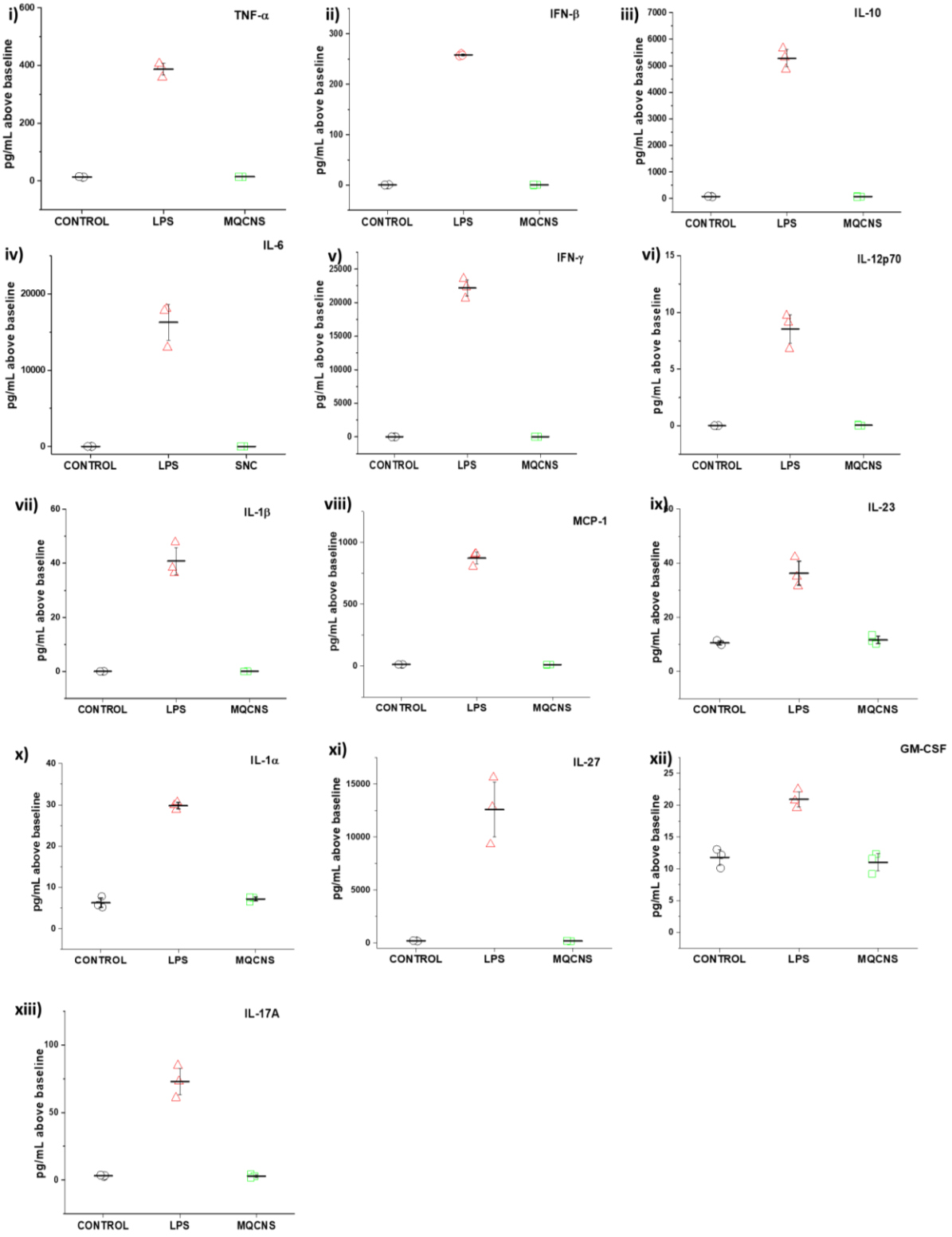

Fig 4.9: Mouse Inflammatory cytokine analysis on Day 1 post injection for 13 major cytokines. All values are given as pg/mL above baseline.

Table 4.1 Table depicting inflammatory cytokines analysed during the study and their role in inflammation.

Sr. No	Name of inflammatory Cytokine	Status	Immune response	Function
1.	IL-1α	Pro-inflammatory	innate	stimulates the activity of genes involved in inflammation and immunity
2.	IL-1β	Pro-inflammatory	innate	activated in pain, inflammation, autoimmune reaction
3.	IL-6	Both pro- and anti-inflammatory	Innate and adaptive	Pivotal cytokine in host immune response, induce acute phase response
4.	IL-10	anti-inflammatory	Innate and adaptive	inhibits the production of proinflammatory cytokines
5.	IL-12(p70)	Pro-inflammatory	adaptive	Promotes induction of TH_1 cells and cytotoxic T cell responses, enhances IFN- γ production
6.	IL-17A	Pro-inflammatory	Innate and adaptive	promoting recruitment of neutrophils to sites of inflammation
7.	IL-23	Pro-inflammatory	Innate and adaptive	Enhancing differentiation of TH1 cells and promoting inflammatory response in various organs
8.	IL-27	Both pro- and anti-inflammatory	Innate and adaptive	involved in T cell differentiation, inflammation and infection
9.	MCP-1	Chemokine	innate	directs the migration of monocytes and macrophages into inflammatory sites
10.	IFN-β	Both pro- and anti-inflammatory	innate	Induction and activation of transcription proteins to regulate inflammation
11.	IFN-γ	Pro-inflammatory	Innate and adaptive	triggers immune response activation and stimulation for pathogen clearance
12.	TNF-α	Pro-inflammatory	innate	Pivotal role in vasodilation and edema formation, signalling cascade leading to apoptosis/ necrosis
13.	GM-CSF	Pro-inflammatory	innate	Promotes growth and differentiation of granulocytes and macrophage cells

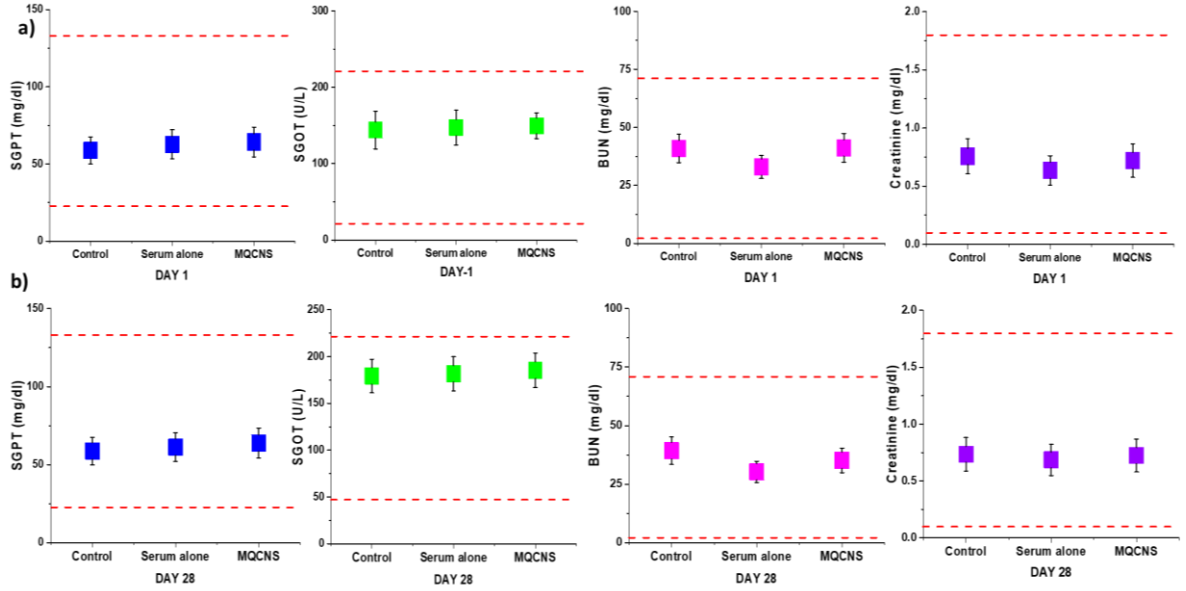

Fig 4.10: Vital organ functioning tests: SGPT, SGOT, BUN, Creatinine on a) Day 1 post injection and b) Day 28 post injection.

The serum biomarkers for proper functioning of vital organs were also analysed. Aspartate aminotransferase (Reference range: 46-221 U/L), alanine aminotransferase (Reference range: 22-133 U/L), blood urea creatinine (Reference range: 2-71 mg/dl) and creatinine (Reference range: 0.1-1.8 mg/dl) were analysed post Day 1 and Day 28 of treatment. The test results were found to be within the normal reference range for C57BL/6 mice and therefore did not affect the vital organ functioning on Day 1 and Day 28 (**Fig 4.10a** & **Fig 4.10b)** respectively.

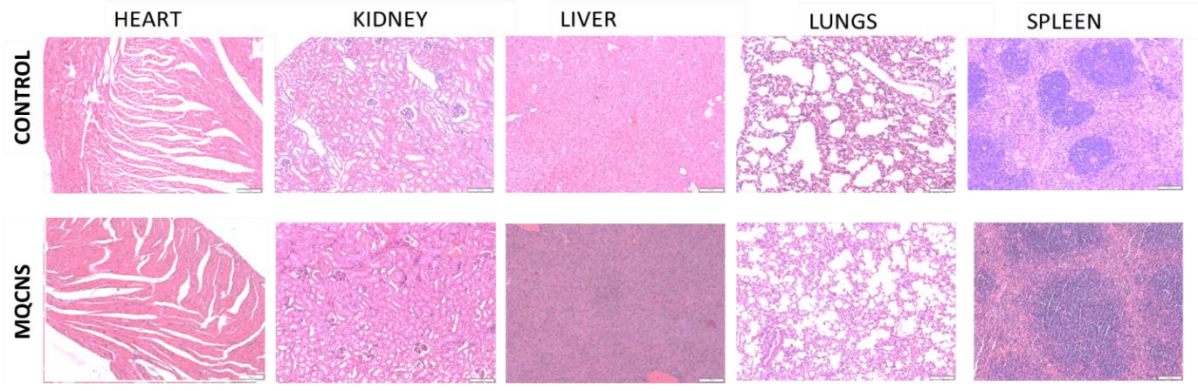

Fig 4.11: Histopathological analysis of vital organs on Day 28 post injection. Scale bar- 100 µm.

Histopathological analysis of the organ with haematoxylin and eosin staining depicted no signs of infiltrating inflammatory cells, or tissue damage 28 days p.i. **(Fig 4.11)**. Hence, the dual dosage regimen of QCNS (50mg/kg; Au 5mg/kg per dose) was observed to be safe for further preclinical and clinical applications.

4.3. Conclusion and Future Prospects

Host specific serum protein stabilised gold quantum clusters with ultra-small size, good aqueous solubility and photostability have been observed to act as radiosensitisers *in-vitro*. Preliminary examination indicated that albumin is predominantly involved in the formation of quantum clusters. However, the other major serum proteins such as globulins and lipoproteins also have the basic chemical composition required to form AuQCs. Future directions may include identification of the right synthetic environment to activate these proteins for QC stabilization and eventual utilization for targeted theranostics. In general, the QCNS seem to be safe after double dosage intravenous administration indicating their potential for clinical translation. Considering their host specific nature, QCNS could be utilized in a heterogenous population that fail to tolerate generic medicinal approaches. Further evaluation of QCNS for long term biodistribution and simultaneous validation of their excretory pathway would pave way for their application in personalized theranostics.

References:

[1] J. Xie, Y. Zheng, and J. Y. Ying, "Protein-Directed Synthesis of Highly Fluorescent Gold Nanoclusters," *J. Am. Chem. Soc.*, vol. 131, no. 3, pp. 888–889, Jan. 2009.

[2] D.-H. Hu *et al.*, "Hybrid gold-gadolinium nanoclusters for tumor-targeted NIRF/CT/MRI triple-modal imaging in vivo.," *Nanoscale*, vol. 5, no. 4, pp. 1624–1628, Feb. 2013.

[3] K. Sood and A. Shanavas, "The Role of Gold Nanoclusters as Emerging Theranostic Agents for Cancer Management," *Curr. Pathobiol. Rep.*, vol. 9, no. 2, pp. 33–42, 2021.

[4] R. Khandelia, S. Bhandari, U. N. Pan, S. S. Ghosh, and A. Chattopadhyay, "Gold Nanocluster Embedded Albumin Nanoparticles for Two-Photon Imaging of Cancer Cells Accompanying Drug Delivery," *Small*, vol. 11, no. 33, pp. 4075–4081, Sep. 2015.

[5] D. Chen, Z. Luo, N. Li, J. Y. Lee, J. Xie, and J. Lu, "Amphiphilic Polymeric Nanocarriers with Luminescent Gold Nanoclusters for Concurrent Bioimaging and Controlled Drug Release," *Adv. Funct. Mater.*, vol. 23, no. 35, pp. 4324–4331, Sep.

2013.

[6] S. Tang *et al.*, “Tailoring Renal Clearance and Tumor Targeting of Ultrasmall Metal Nanoparticles with Particle Density,” *Angew. Chem. Int. Ed. Engl.*, vol. 55, no. 52, pp. 16039–16043, Dec. 2016.

[7] P. Zhang, X. X. Yang, Y. Wang, N. W. Zhao, Z. H. Xiong, and C. Z. Huang, “Rapid synthesis of highly luminescent and stable Au20 nanoclusters for active tumor-targeted imaging in vitro and in vivo,” *Nanoscale*, vol. 6, no. 4, pp. 2261–2269, 2014.

[8] R. Atun *et al.*, “Expanding global access to radiotherapy,” *Lancet Oncol.*, vol. 16, no. 10, pp. 1153–1186, 2015.

[9] M. Abdel-Wahab *et al.*, “Global Radiotherapy: Current Status and Future Directions—White Paper,” *JCO Glob. Oncol.*, no. 7, pp. 827–842, 2021.

[10] D. Luo, X. Wang, S. Zeng, G. Ramamurthy, C. Burda, and J. P. Basilion, “Targeted Gold Nanocluster-Enhanced Radiotherapy of Prostate Cancer,” *Small*, vol. 15, no. 34, p. 1900968, Aug. 2019.

[11] F. Ghahremani, A. Kefayat, D. Shahbazi-Gahrouei, H. Motaghi, M. A. Mehrgardi, and S. Haghjooy-Javanmard, “AS1411 aptamer-targeted gold nanoclusters effect on the enhancement of radiation therapy efficacy in breast tumor-bearing mice,” *Nanomedicine*, vol. 13, no. 20, pp. 2563–2578, Oct. 2018.

[12] G. Liang, X. Jin, S. Zhang, and D. Xing, “RGD peptide-modified fluorescent gold nanoclusters as highly efficient tumor-targeted radiotherapy sensitizers,” *Biomaterials*, vol. 144, pp. 95–104, 2017.

[13] X.-D. Zhang *et al.*, “Ultrasmall Au10−12(SG)10−12 Nanomolecules for High Tumor Specificity and Cancer Radiotherapy,” *Adv. Mater.*, vol. 26, no. 26, pp. 4565–4568, Jul. 2014.

[14] R. K. Samani, M. B. Tavakoli, F. Maghsoudinia, H. Motaghi, S. H. Hejazi, and M. A. Mehrgardi, “Trastuzumab and folic acid functionalized gold nanoclusters as a dual-targeted radiosensitizer for megavoltage radiation therapy of human breast cancer,” *Eur. J. Pharm. Sci.*, vol. 153, p. 105487, 2020.

[15] T.-T. Jia *et al.*, “Atomically Precise Gold–Levonorgestrel Nanocluster as a Radiosensitizer for Enhanced Cancer Therapy,” *ACS Nano*, vol. 13, no. 7, pp. 8320–8328, Jul. 2019.

[16] K. T. Butterworth, S. J. McMahon, F. J. Currell, and K. M. Prise, “Physical basis and biological mechanisms of gold nanoparticle radiosensitization,” *Nanoscale*, vol. 4, no. 16, pp. 4830–4838, 2012.

[17] X.-D. Zhang *et al.*, “Ultrasmall Glutathione-Protected Gold Nanoclusters as Next Generation Radiotherapy Sensitizers with High Tumor Uptake and High Renal Clearance,” *Sci. Rep.*, vol. 5, no. 1, p. 8669, 2015.

[18] X.-D. Zhang *et al.*, “Enhanced Tumor Accumulation of Sub-2 nm Gold Nanoclusters for Cancer Radiation Therapy,” *Adv. Healthc. Mater.*, vol. 3, no. 1, pp. 133–141, Jan. 2014.

[19] G. Liang *et al.*, “One-pot synthesis of Gd3+-functionalized gold nanoclusters for dual model (fluorescence/magnetic resonance) imaging,” *J. Mater. Chem. B*, vol. 1, no. 29,

pp. 3545–3552, 2013.

[20] R. Rajamanikandan and M. Ilanchelian, “Red emitting human serum albumin templated copper nanoclusters as effective candidates for highly specific biosensing of bilirubin,” *Mater. Sci. Eng. C*, p. #pagerange#, 2019.

[21] J.-M. Liu, J.-T. Chen, and X.-P. Yan, “Near Infrared Fluorescent Trypsin Stabilized Gold Nanoclusters as Surface Plasmon Enhanced Energy Transfer Biosensor and in Vivo Cancer Imaging Bioprobe,” *Anal. Chem.*, vol. 85, no. 6, pp. 3238–3245, Mar. 2013.

[22] F. Wen, Y. Dong, L. Feng, S. Wang, S. Zhang, and X. Zhang, “Horseradish Peroxidase Functionalized Fluorescent Gold Nanoclusters for Hydrogen Peroxide Sensing,” *Anal. Chem.*, vol. 83, no. 4, pp. 1193–1196, Feb. 2011.

[23] P. Liu *et al.*, “Synthesis of fluorescent α-chymotrypsin A-functionalized gold nanoclusters and their application to blot-based technology for Hg2+ detection,” *RSC Adv.*, vol. 4, no. 60, pp. 31536–31543, 2014.

[24] Q. Li *et al.*, “Design and mechanistic study of a novel gold nanocluster-based drug delivery system,” *Nanoscale*, vol. 10, no. 21, pp. 10166–10172, 2018.

[25] R. Vankayala, C.-L. Kuo, K. Nuthalapati, C.-S. Chiang, and K. C. Hwang, “Nucleus-Targeting Gold Nanoclusters for Simultaneous In Vivo Fluorescence Imaging, Gene Delivery, and NIR-Light Activated Photodynamic Therapy,” *Adv. Funct. Mater.*, vol. 25, no. 37, pp. 5934–5945, Oct. 2015.

[26] Y. Li, M. Yuan, A. J. Khan, L. Wang, and F. Zhang, “Peptide-gold nanocluster synthesis and intracellular Hg2+ sensing,” *Colloids Surfaces A Physicochem. Eng. Asp.*, vol. 579, p. 123666, 2019.

[27] C.-L. Liu *et al.*, “Insulin-Directed Synthesis of Fluorescent Gold Nanoclusters: Preservation of Insulin Bioactivity and Versatility in Cell Imaging,” *Angew. Chemie Int. Ed.*, vol. 50, no. 31, pp. 7056–7060, Jul. 2011.

[28] H.-H. Deng *et al.*, “Fenton reaction-mediated fluorescence quenching of N-acetyl-l-cysteine-protected gold nanoclusters: analytical applications of hydrogen peroxide, glucose, and catalase detection,” *Analyst*, vol. 140, no. 22, pp. 7650–7656, 2015.

[29] G. Gao *et al.*, “Gold nanoclusters for Parkinson’s disease treatment,” *Biomaterials*, vol. 194, pp. 36–46, 2019.

[30] J.-Y. Wang *et al.*, “Effects of surface charges of gold nanoclusters on long-term in vivo biodistribution, toxicity, and cancer radiation therapy.,” *Int. J. Nanomedicine*, vol. 11, pp. 3475–3485, 2016.

[31] J. S. Mohanty, A. Baksi, H. Lee, and T. Pradeep, “Noble metal clusters protected with mixed proteins exhibit intense photoluminescence,” *RSC Adv.*, vol. 5, no. 59, pp. 48039–48045, 2015.

[32] M. Li, D.-P. Yang, X. Wang, J. Lu, and D. Cui, “Mixed protein-templated luminescent metal clusters (Au and Pt) for H2O2 sensing,” *Nanoscale Res. Lett.*, vol. 8, no. 1, p. 182, 2013.

[33] J. Tian, L. Yan, A. Sang, H. Yuan, B. Zheng, and D. Xiao, “Microwave-Assisted Synthesis of Red-Light Emitting Au Nanoclusters with the Use of Egg White,” *J.*

Chem. Educ., vol. 91, no. 10, pp. 1715–1719, Oct. 2014.

[34] D. Joseph and K. E. Geckeler, "Synthesis of highly fluorescent gold nanoclusters using egg white proteins," *Colloids Surfaces B Biointerfaces*, vol. 115, pp. 46–50, 2014.

[35] X.-J. Li, J. Ling, C.-L. Han, L.-Q. Chen, Q.-E. Cao, and Z.-T. Ding, "Chicken Egg White-stabilized Au Nanoclusters for Selective and Sensitive Detection of Hg(II)," *Anal. Sci.*, vol. 33, no. 6, pp. 671–675, 2017.

[36] J. Lazarovits *et al.*, "Synthesis of Patient-Specific Nanomaterials," *Nano Lett.*, vol. 19, no. 1, pp. 116–123, Jan. 2019.

[37] Mimansa, M. Jamwal, R. Das, and A. Shanavas, "High Drug Loading Nanoparticles Stabilized with Autologous Serum Proteins Passively Inhibits Tumor Growth.," *Biomacromolecules*, vol. 23, no. 12, pp. 5065–5073, Dec. 2022.

[38] C.-J. L. Farrell and A. C. Carter, "Serum indices: managing assay interference.," *Ann. Clin. Biochem.*, vol. 53, no. Pt 5, pp. 527–538, Sep. 2016.

[39] Z. Tang *et al.*, "Fabrication of avidin-stabilized gold nanoclusters with dual emissions and their application in biosensing," *J. Nanobiotechnology*, vol. 20, no. 1, p. 306, 2022.

[40] D. Li, M. Zhu, C. Xu, and B. Ji, "Characterization of the baicalein–bovine serum albumin complex without or with Cu2+or Fe3+ by spectroscopic approaches," *Eur. J. Med. Chem.*, vol. 46, no. 2, pp. 588–599, 2011.

[41] M. Longmire, P. L. Choyke, and H. Kobayashi, "Clearance properties of nano-sized particles and molecules as imaging agents: considerations and caveats.," *Nanomedicine (Lond).*, vol. 3, no. 5, pp. 703–717, Oct. 2008.

[42] A. K. Rengan *et al.*, "In Vivo Analysis of Biodegradable Liposome Gold Nanoparticles as Efficient Agents for Photothermal Therapy of Cancer," *Nano Lett.*, vol. 15, no. 2, pp. 842–848, Feb. 2015.

[43] P. Yadav *et al.*, "Nontoxic In Vivo Clearable Nanoparticle Clusters for Theranostic Applications," *ACS Biomater. Sci. Eng.*, vol. 8, no. 5, pp. 2053–2065, May 2022.

[44] M. KOLTUN and W. D. COMPER, "Retention of Albumin in the Circulation is Governed by Saturable Renal Cell-Mediated Processes," *Microcirculation*, vol. 11, no. 4, pp. 351–360, 2004.

[45] T. A. WALDMANN, "ALBUMIN CATABOLISM," V. M. ROSENOER, M. ORATZ, and M. A. B. T.-A. S. ROTHSCHILD Function and Uses, Eds. Pergamon, 1977, pp. 255–273.

[46] J. Gburek, K. Gołąb, and K. Juszczyńska, "[Renal catabolism of albumin - current views and controversies].," *Postepy Hig. Med. Dosw. (Online)*, vol. 65, pp. 668–677, Oct. 2011.

[47] J. KATZ, S. ROSENFELD, and A. L. SELLERS, "Sites of plasma albumin catabolism in the rat.," *Am. J. Physiol.*, vol. 200, pp. 1301–1306, Jun. 1961.

Chapter 5

Preclinical Safety Assessment of Host-Specific Silver Quantum Clusters Stabilized with Autologous Serum Proteins for Antibacterial Applications

5. INTRODUCTION

The antimicrobial resistance arising from suboptimal use of antibiotics is a major threat looming on mankind with a predicted overtake on cancer death toll in the coming decades [1]. About 40% of recurrent infections gain resistance to initial antibiotic treatment for common urinary tract infections caused by *E.coli* strains [2]. Moreover amongst the bacterial species causing wound infections, Gram-negative *P. aeruginosa* (40.2%), *E.coli* (20.7%), and Gram-positive *S. aureus* (79.4%) were identified to be the most common [3]. At least one antibiotic resistant strain was detected in 88.2% of isolates from infected wound, while multi-drug resistance was observed in up to 6 antimicrobial drugs in 29.2% of isolates raising alarm worldwide [3]. Hence, there is an urgent need to develop an alternative class of antibacterial agents with the ability to overcome resistance. The emerging class of photoluminescent silver quantum clusters (AgQCs) demonstrate significant potential for biomedical applications owing to their ultra-small size and aqueous solubility. The pronounced antimicrobial activity of QCs compared to their nanoparticle counterparts due to enhanced interaction with the organism as they possess larger surface area/volume ratio. This is facilitated by the availability of more Ag atoms, which can be released towards the generation of higher levels of reactive oxygen species (ROS) [4]–[6].

AgQCs are synthesized mainly through two methods: either bottom-up approach including direct reduction of Ag ions using strong reducing agents or using a top-down approach involving chemical etching of larger AgNPs [7]. Typically, AgQCs consist of a core-shell structure, comprising a metallic Ag core and an organic ligand shell with different chain length, and functional groups that can alter the overall size, structure, and optical properties of QCs, thus affecting their biological applications. Both the core and shell can be tailored independently by altering reaction parameters such as ligand to precursor metal ratio, reaction time, pH, temperature, and concentration of reducing agent [7],[8]. Stabilization of AgQCs is commonly achieved by utilizing biomolecules such as DNA[9], peptides [10], proteins,

dendrimers [11] and polymers [12], [13] for various biomedical applications including cellular tracking and bioimaging.

The most crucial prerequisite for utilizing QCs with biological systems is their biocompatibility and effective clearance from the body. Therefore, to optimize their utility for antimicrobial applications, it becomes imperative to stabilize AgQCs with biocompatible agents such as proteins due to their biological inertness, aqueous solubility, photostability, and ease of synthesis under mild reducing conditions. The use of serum albumin for synthesizing QCs has been demonstrated to be a fairly robust and facile synthetic procedure in a one-pot reaction [14], [15]. QCs have also been reported to exert a size dependant bactericidal effect. Proteins such as lysozyme, hydrophobic monodentate-thiolate molecules and peptides such as glutathione have been utilized for QC formation for antimicrobial applications[16],[17],[18]. The antimicrobial activity of GSH capped AgQCs has been explored by conjugating it with antiobiotic daptomycin for enhanced antibacterial efficiency against *S. aureus* [19]. Similarly, AgQCs stabilised with Poly(methacrylic acid) have been embedded into zein films to develop food packaging materials for high efficacious antimicrobial applications with low cytotoxicity [20]. A pH-sensitive charge reversal ligand poly(ethylene glycol)-poly(aminopropyl imidazole-aspartate)-polyalanine stabilised AgQCs have been utilised as biofilm-responsive nanoantibiotics for multi-drug resistant bacterial infections [21]. Apart from antimicrobial applications, bovine and human serum albumin capped AgQCs have been comingled with graphene oxide sheets for synergistic drug delivery and enhanced bioimaging applications [22] However, the full potential of protein-protected AgQCs remains largely untapped in terms of their antimicrobial applications.

Amidst various protein stabilizers being explored, the quest for the most compatible and effective ligand for AgQCs persists that ensures optimal antimicrobial activity without compromising the patient safety during therapies. In this pursuit, the utilisation of autologous serum proteins presents a compelling solution for stabilizing silver quantum clusters, addressing any concerns regarding immunogenicity and compatibility. Autologous serum proteins offer a personalized approach, as being derived from the patient's own blood serum, they are expected to minimize the risk of adverse reactions and promote biocompatibility. Moreover, there have been reports suggesting that the host-directed personalised antimicrobial strategies might help augment the host-immune response to increase microbial clearance from the body. This can be achieved by either enhancing microbial phagocytosis and/or by modulating the damage inflicted by the microbe on the host’s immune system especially in the

elderly and therefore can be leveraged over conventional antimicrobial agents to overcome antimicrobial resistance [23].

With this perspective, we have developed host-specific autologous serum protein-stabilized photoluminescent Ag Quantum Cluster Nano Sera (termed as Ag-QCNS) to combat bacterial infections with enhanced host safety. Our group has previously demonstrated the non-immunogenicity of autologous serum protein-stabilized drug crystals and quantum clusters for therapeutic applications [24],[25]. Leveraging endogenously derived proteins minimizes the likelihood of causing inflammatory responses and ensures eventual safe metabolism by the body. This strategy embraces a synergistic antimicrobial approach, employing Ag to effectively combat bacteria alongside the non-immunogenic autologous serum protein scaffold, resulting in the development of Ag-QCNS. We have effectively established their antibacterial effect on Gram-positive and Gram-negative bacteria. Further, we have established the preclinical safety of host-specific autologous serum protein-stabilized Ag QCNS in a Balb/c mice model. Short-term *in-vivo* biodistribution and hemocompatibility of host-specific Ag-QCNS were performed to understand the pharmacokinetic profile. Given the well-known wound-healing properties of Ag nanomaterials, we investigated the effect of Ag-QCNS on wound healing in normal murine fibroblast L929 cells. Our findings highlight the importance of strategic design in personalized nanomedicine and biocompatible nanotherapeutics, which is integral to combating antimicrobial resistance and promoting personalized nanotherapeutic approaches.

5.1. Experimental Section:

5.1.1. Materials

Silver nitrate (209139; Sigma), Fetal bovine serum (FBS, RM9955-heat inactivated; Himedia), bicinchoninic acid (BCA) protein assay kit (71285-3; Sigma), MTT (Thiazolyl blue tetrazolium bromide) dye for cell culture (TC191; Himedia), bovine serum albumin (BSA; Himedia), nuclear staining dye- bisBenzimide H33342 trihydrochloride (Hoechst 33342, B2261; Sigma), live cell staining dye- fluorescein diacetate (F7378; Sigma), dead cell staining dye- propidium iodide (P4170; Sigma), Luria Bertani (M1245;HiMedia). All other chemicals were of analytical grade and were used without further purification unless mentioned otherwise. Autoclaved ultrapure water (~18 MΩ) was used for AgQC synthesis.

5.1.2. Instrumentation

Dynamic light scattering (DLS) and Zeta potential measurements were performed with Malvern Zetasizer Nano ZSP instrument. Transmission electron microscopy (TEM) and High

resolution transmission electron microscopy (HR-TEM) measurements were performed at an accelerating voltage of 120 and 200 kV respectively using JEOL JEM-2100. Morphological analysis of treated and untreated fixed bacterial cells was performed by sputter coating the fixed bacterial samples with gold and visualized using a scanning electron microscope (JSM-IT300: JEOL, Japan). TCSPC analysis was carried out using Fluorolog 3-221 fluorimeter equipped with 450 W Xenon lamp. UV-Visible absorption spectra and Fluorescence spectra were recorded in multimode reader (Synergy H1, BioTek). X-ray photoelectron spectrometry analysis (XPS) experiments were performed using an ESCALAB 250 xi (Thermo Scientific) spectrometer using monochromatic Al Kα radiation. Confocal Laser Scanning Microscopy (CLSM) was carried out using LSM 880 Confocal microscope (manufactured by Carl Zeiss, Germany). *Ex vivo* imaging was carried out using PerkinElmer IVIS Lumina series II.

5.1.3. Synthesis of silver quantum clusters stabilized with serum proteins (Ag-QC-NanoSera: Ag-QCNS)

Silver quantum clusters stabilized with whole serum proteome were synthesized as per previously reported [14], [15] serum was used as a proof of concept for synthesis and the study was extended to utilising human serum proteome stabilised QCs for antibacterial applications and their pre-clinical safety was established in autologous Balb/c mice.

Ag-QCNS synthesis: Firstly, serum was quantified for total protein content using BCA assay. Next, serum protein (50 mg/mL equivalent, 1 mL) was added in a clean glass vial and $AgNO_3$ (10 mM, 1 mL) was added dropwise to the solution under high stirring at room temperature. The solution was allowed to incubate for 2 minutes followed by addition of NaOH (1 M, 100 µL) to adjust the pH ~12. Next, $NaBH_4$ (10 mM) was added dropwise in steps of 5 µL. The reaction was allowed to proceed for 1 h in dark and sterile conditions. The Ag-QCNS thus formed were dialysed (MW cut off: 2000-14000 kDa) overnight against ultrapure water and were stored at 4 °C for immediate analysis or lyophilized for long-term storage.

Human serum Ag-QCNS were synthesised using the same protocol utilised for making Ag-QCNS after obtaining necessary approval from the institutional ethics committee of PGIMER (PGI/IEC/2020/000787). 5 mL of human whole blood samples were collected from healthy blood donors with informed prior consent. The blood was allowed to clot for 30 minutes at room temperature, the samples were centrifuged at 5000 rpm for 10 minutes at 4 °C, and the supernatant was collected. The human serum was stored at -20 °C in multiple aliquots until further use and was quantified for total protein content at the time of usage. The synthesis process is exactly similar to synthesis of Ag-QCNS made from bovine serum. Dialysis was

carried out post synthesis, and the samples were lyophilised and stored at -20 °C for further analysis.

Mouse serum Ag-QCNS were synthesised to establish preclinical safety, hemocompatibility, biodistribution and clearance of autologously derived M-Ag-QCNS in in-bred Balb/c mice with necessary approvals from institutional animal ethics committee of IISER Mohali (IISERM/SAFE/PRT/2020/001). The mice serum collection and processing is explained in later section. After synthesis, the samples were dialysed and stored at -20 °C for animal experimentation.

5.1.4. Cellular Studies

The biocompatibility analysis, cellular localisation and wound healing studies of Ag-QCNS were carried out with murine fibroblast L929 cells cultured in DMEM (10% (v/v) FBS and 1% (v/v) antibiotic-antimycotic solution were added for media supplementation) in a humidified incubator containing 5% CO_2 at 37 °C with sub-culturing around 2-3 times per week.

5.1.5. *In-vitro* biocompatibility

For biocompatibility analysis, L929 cells were seeded at a density of 8.0 x10^3 cells in a 96 well plate for 24 h at 37 °C and 5% CO_2. The cells were left to adhere overnight. The following day, different concentrations of Ag-QCNS (0, 50, 100, 200, 300, 400, 500, 1000 µg/mL) were incubated with the cells for 24 h. Next day, the cells were washed twice with PBS to remove any unbound Ag-QCNS and each well was added with 10% MTT solution (5 mg/mL dissolved in PBS) diluted in media and was incubated for 3 h. Thereafter, the media was pipetted out carefully so that the purple formazan crystals formed are not disturbed and 100 µL of DMSO was added to each well and mixed properly until they were dissolved. The absorbance was recorded at 595 nm on a multimode plate reader. The experiment was carried out in triplicates. Cell viability was calculated using the formula:

$$\text{Cell viability } \% = \frac{\text{Absorbance of sample at 595nm} \times 100}{\text{Absorbance of control at 595nm}}$$

5.1.6. Biocompatibilty and hemocompatibility of Ag QCNS

i) Dosage dependant confocal uptake in mammalian cells

To check the cellular uptake of Ag-QCNS, L929 cells were seeded on a cover slip at a density of 1x105 cells per well in a 6 well plate and were grown to reach ~ 70% confluency. Thereafter, Ag-QCNS was added at different concentrations (0, 100, 200, 400 µg/mL) and incubated for 24 h. The treated cells were further washed twice with PBS to remove any unbound sample

and fixed with 4% paraformaldehyde for about 10 minutes at room temperature. Next, the nuclei were counter stained with Hoechst 33342 for 10 minutes at 37 °C. The L929 cells were then washed thrice with PBS to remove any excess stain and coverslip containing the fixed cells was mounted on a glass slide and analysed under CLSM.

ii) Time dependant confocal uptake in mammalian cells

To check the time dependence of cellular uptake of Ag-QCNS in normal L929 were seeded on a cover slip at a density of $1x10^5$ cells per well in a 6 well plate till ~ 70% confluency was achieved. Thereafter, Ag-QCNS was added at final concentration of 250 µg/mL and incubated for different time periods (0, 0.5, 3, 6 h). After the designated time periods, the treated cells were similarly washed with PBS and fixed with 4% paraformaldehyde followed by subsequent staining of the cellular nuclei with Hoechst 33342 and were analysed under CLSM.

iii) *In-vivo* hemocompatibility of autologous Ag-QCNS

After intravenous dosing the mice for hemolysis assay, (0.44 mg/kg Ag equivalent) for pre-determined time periods, the mice whole blood was collected in clean vial pre-treated with 3.8% (w/v) trisodium citrate. The RBCs were centrifuged (5000 rpm, 10 minutes at 4 °C) to separate the lysed cellular component and the absorbance of the cell-free supernatant was measured at 545 nm in triplicates. Milli-Q water and PBS were used as positive and negative controls for the assay. Hemolysis percentage was calculated using the formula:

$$\% \text{ Hemolysis} = \frac{\text{Abs of test sample} - \text{Abs of negative control}}{\text{Abs of positive control} - \text{Abs of negative control}}$$

5.1.7. *In-vitro* scratch assay

Silver nanomaterials have been widely used in wound dressings due to the release of silver ions onto the wound surface and their subsequent bactericidal activity[26][27]. Henceforth, scratch assay was performed to determine the wound healing capability of Ag-QCNS. Briefly, L929 cells were seeded in a 48 well plate at a density of $2x10^4$ cells and were allowed to form a consistent monolayer. Thereafter, a sterile 1 mL tip was utilised to make a scratch in each well, the media was carefully pipetted out, and the wells were washed with PBS. Subsequently, Ag-QCNS solution (final concentration 0, 250 µg/mL) was added in each well and the cell migration was monitored at different time points and the bright field images were captured at 10x using Leica bright-field microscope. The experiment was performed in triplicates and the images were analysed using ImageJ software.

5.1.8. Antibacterial activity of Ag-QCNS

Preliminary antibacterial activity of Ag-QCNS samples were performed against Escherichia coli (*E. coli*, MTCC- 452). Later on, the antimicrobial activity testing was extended on Staphylococcus aureus (*S. aureus*, MTCC- 96) and Pseudomonas aeruginosa (*P. aeruginosa*, MTCC- 3541) and an antibiotic resistant strain of *E.coli* with pET 41A vector carrying Kanamycin resistance gene (denoted as *E.coli* ^{KRes}) was received as a kind gift from Dr. Sharmistha Sinha (INST Mohali). All the other microbial cultures were procured from IMTECH Chandigarh. The necessary approvals required from institutional biosafety committee of INST Mohali were procured**.** All the experiments were carried out in triplicates, unless stated otherwise.

i. Bacterial inhibition kinetics

The effect of Ag-QCNS on the bacterial inhibition was monitored through overnight kinetic cycle. Briefly; log-phase bacteria were diluted for an OD~0.1 and 100 µL of cell suspension was incubated for overnight with 100 µL Ag-QCNS at different final concentrations in a 96 well plate at 37 °C under constant shaking conditions and the kinetic OD_{600} readings were recorded at an interval of 30 minutes. The experiment was carried out in triplicates and the results were plotted as OD_{600} vs time (minutes) graph. Ciprofloxacin was used as positive control for bacterial cultures and untreated bacterial samples were treated as negative control.

ii. Colony Formation Unit Assay

The antimicrobial susceptibility of Ag-QCNS was established using CFU assay with different bacterial strains. Briefly, the log-phase bacteria were diluted with media such that OD_{600} ~0.1.Thereafter, Ag-QCNS were incubated with bacteria at different final concentrations at 37°C for 12 h. Post treatment, the bacterial cultures were diluted (DF: 10^3-10^4) and finally 10 µL of bacterial suspension and spread on Mueller Hinton Agar (MHA) agar plates using sterile spreader and incubated at 37°C for 24 h. The images of plates were acquired with G-box: Chemi XRQ (Syngene) and number of CFUs/mL were counted using ImageJ software. The IC_{50} values were calculated and compared for different bacteria using this data. Ciprofloxacin (2 mg/mL) was used as positive control. All samples were carried out in triplicates.

iii. Confocal uptake of Ag-QCNS in bacteria

The uptake of bacteria was analysed through confocal microscopy. Briefly, fresh bacterial culture in log-phase (OD_{600} ~0.1) were incubated with Ag-QCNS (final concentration: 0 and

250 µg/mL) for 12 h at 37 °C under constant shaking at 180 rpm. After treatment, the bacterial suspension was washed thrice with PBS and fixed with 4% PFA solution. Thereafter, the bacterial nucleus was counter-stained with Hoechst 33342 and the cell suspension was mounted onto clean glass slides and analysed under CLSM.

iv. Bacterial Viability Assay (Live/Dead)

The live/dead assay was performed by differential staining using fluorescein diacetate (FDA) and propidium iodide (PI) to detect live and dead bacteria, respectively. The log-phase bacterial cells (OD_{600}~0.1, 500 µL) were incubated with Ag-QCNS (500 µL) to yield final sample concentrations - 0, 250 µg/mL at 37 °C for 12 h. Following treatment, the cells were centrifuge washed thrice with sterile PBS and the bacterial pellet was re-dispersed in 200 µL PBS. The cell suspension was then incubated with 200 µL of the dye-containing solution, which was prepared by adding 10 µL of FDA (5 mg/mL) and 50 µL of propidium iodide (2 mg/mL) to 5 mL of PBS buffer, at RT (dark conditions) for 20 minutes, following which the bacterial cells were washed thrice with sterile PBS to remove any excess stain. Finally, the stained live bacterial cell suspension was mounted on a glass slide and examined under CLSM immediately.

v. Detection of Reactive Oxygen Species (ROS)

The antimicrobial activity of silver nanomaterials is reportedly due to the formation of reactive oxygen species and lead to oxidative stress that cause damage to the membrane permeability and subsequently the bacterial DNA and proteins that are crucial for survival of bacteria. For studying the concentration dependant ROS production of Ag-QCNS, fresh log-cultures of bacteria (OD~0.1) were incubated with Ag-QCNS (250, 500 µg/mL) in a shaker for 6 h at 37 °C at 180 rpm in triplicates for predetermined time points. Subsequently, after each time point, the set of bacterial suspension was washed thrice with PBS and 90 µM DCFDA was added to the sample solution and incubated at 37 °C for 15 mins under constant shaking in dark conditions. The presence of ROS is detected spectrophotometrically by H_2DCFDA (Dichlorodihydrofluorescein diacetate acetyl ester), a cell-permeable non-florescent dye, that is oxidized to its green flourescent form DCF (2', 7'-dichlorofluorescein) by intracellular esterases in presence of ROS species. The green fluorescence is recorded (λ_{ex} 488 nm and λ_{em} 525 nm) and is directly proportional to the amount of ROS produced. H_2O_2 was used as positive control and untreated samples are treated as negative controls for the analysis.

vi. Cellular morphological assessment of damaged bacteria through FESEM and TEM

The morphological assessment of damage in treated bacteria was carried out using FESEM analysis, fresh bacterial cultures in log-phase (OD_{600} ~0.1) were incubated with Ag-QCNS (at final concentration: 250 µg/mL) for 12 h at 37 °C under 180rpm. After treatment, the bacterial cells were washed thrice with PBS and fixed with 2.5% glutaraldehyde (v/v) (in 0.1 M sodium cacodylate solution) and kept in 4 °C for 2 h under constant shaking conditions followed by sequential dehydration in series of ethanol solutions (30%, 50%, 70%, 90%, 100%). The dehydrated samples were re-dispersed in 100% ethanol and drop casted on clean silicon wafers or TEM grids for FESEM and TEM analysis respectively. The TEM samples were counter-stained with 1% (w/v) uranyl acetate for negative staining. Both TEM and FESEM samples were stored in vacuum for drying and the later were sputter coated with gold before analysis.

5.1.9. Animal Experimentation

All the animal experimentation were conducted in accordance with the guidelines approved by the Institutional Animal Ethics Committee at IISER Mohali (IISERM/SAFE/PRT/2020/001). For the safety analysis study, Balb/c female mice aged 6-8 weeks were divided in 4 groups with equal average weights (n=4): Control Day-1, Control Day-28, M-Ag-QCNS treated Day-1 and M-Ag-QCNS treated Day-28. The mice were housed in cages that were located in a well-ventilated, temperature-controlled room 21 ± 2 °C with relative humidity ranging from 40% to 60%, with a light and dark period of 12 h each, and free access to food and water.

5.1.10. Autologous murine serum derived Ag-QCNS synthesis and re-administration:

Two weeks (i.e., D-14) prior to treatment, blood was collected from all the in-bred mice and allowed to clot for 30 minutes at room temperature. Subsequently, the serum was collected as supernatant after centrifuging the blood samples at 5000 rpm for 10 minutes at 4 °C and was pooled together and quantified for total protein content using the BCA assay. The procedure followed for synthesis of M-Ag-QCNS was exactly similar to Ag-QCNS explained in earlier sections. After synthesis, they were dialysed and filtered with 0.2 µm sterile filter, lyophilised and stored at -20 °C before injection. On day 0 (D0), the mice were intravenously injected with single dose (0.1 mL) of M-Ag-QCNS (~0.44 mg/kg Ag content) or saline for treatment and control groups respectively. On day 1 (D1) and day 28 (D28), mice from each group were sacrificed for assessing their sub-acute toxicity. Blood was collected and the serum was stored at -80 °C for further biochemical analysis. Vital organs such as liver, spleen, kidneys, lungs

and heart were extracted for biodistribution analysis using *in vivo* imaging system followed by histopathological analysis.

5.1.11. *In-vivo* biodistribution and preclinical safety assessment

Short term in-vivo biodistribution and hemocompatibility was assessed for intravenously injected ICG-tagged M-Ag-QCNS (~0.44 mg/kg Ag); for different time periods (5 minutes, 30 minutes, 1 h) and the biodistribution was recorded by capturing ex-vivo images of vital organs (Heart, Lungs, Liver, Kidney, Spleen, Gastrointestinal tract or GIT) as well as whole blood and plasma with G-box: Chemi XRQ (Syngene) under excitation with blue LED light and emission collected with bandpass filter covering 700 to 720 nm.

For Ag biodistribution analysis, the vital organs including liver, spleen, lung, kidney and heart were digested with ICP-MS grade nitric acid and incubated at 60 °C for 12 h. The solutions were then further diluted in deionized water such that an optimum pH 3-5 was obtained and were analysed using inductively coupled plasma mass spectrometer (Agilent 7900) to determine Ag concentration against standard calibration curve obtained with solutions of ionic silver from 10 to 500 ppb.

5.1.12. Biochemical analysis

The serum obtained from blood samples collected at Day-1 and Day-28 was quantitatively analysed for biochemical parameters such as aspartate aminotransferase (AST or SGPT), alanine transaminase (ALT or SGOT), creatinine and blood urea nitrogen using ERBA Mannheim kits as per manufacturer's protocol. Cardiotoxicity was assessed qualitatively using a lateral flow test kit for serum troponin I with a single band (≤0.5 ng/mL) indicating negative or double band (>0.5 ng/mL) indicating positive results as per manufacturer's protocol (Standard diagnostics, Inc.).

5.1.13. Histopathological analysis

Vital organs were carefully collected after sacrificing the animal and washed in sterile PBS before storing in 10% buffered formalin solution for fixing and embedding in paraffin. Next, 5µm thick paraffin sections of different organs were processed manually and stained with haematoxylin and eosin dye. The slides were examined at different magnifications to assess any changes in tissue morphology under inverted light microscope.

5.1.14. Statistical Analysis

All the experiments were performed in triplicates unless indicated and the graphs were plotted using OriginPro software. Student's t-test was performed for statistical significance analysis.

5.2. Results and Discussions:

5.2.1. Characterisation of Ag-QCNS

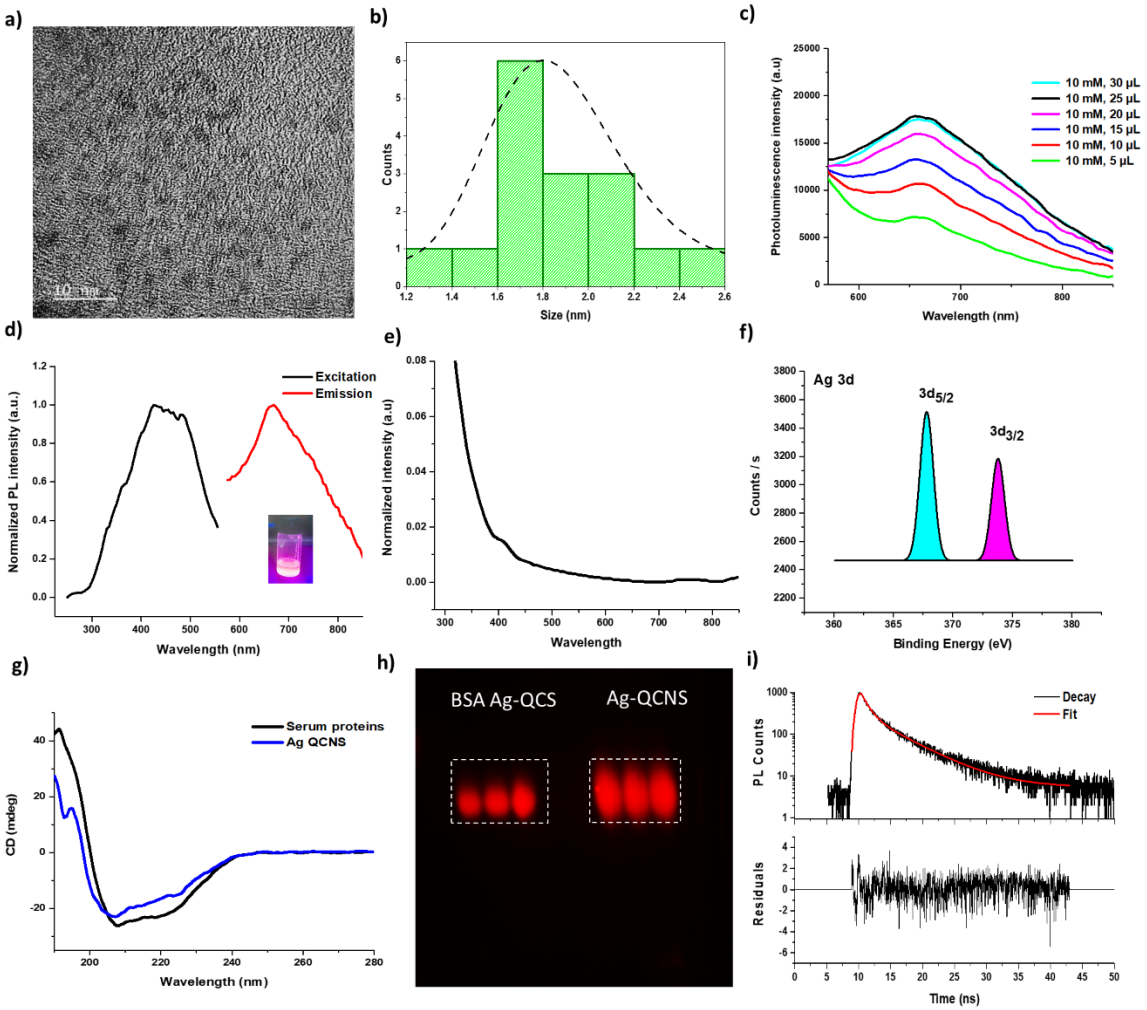

Fig 5.1: Characterisation panel for Ag-QCNS: (a-b) TEM images for Ag-QCNS formed and b) Size distribution histogram of Ag-QCNS c)Optimisation of PL intensity of Ag-QCNS using $NaBH_4$ volume variation d) Excitation and emission spectra e) UV-Vis Absorption spectra f) High resolution Ag 3d XPS spectra g) Circular dichroism spectra (BSA-QCs, Ag-QCNS and serum proteins) h) Agarose gel electrophoresis depicting size similarity of BSA Ag QCs and Ag-QCNS (pseudo color: red) and i) Time-correlated single photon counting (TCSPC) analysis of aqueous Ag-QCNS.

Silver quantum clusters stabilized with whole serum proteome were synthesized based on prior reported method [14], [15]**.** Fetal bovine serum was used for initial optimization. The size of bovine serum derived Ag-QCNS was around 1.96±0.4 nm as confirmed through transmission

electron microscopy **[Fig 5.1a, 5.1b]**. The hydrodynamic size and zeta potential of Ag-QCNS were measured to be 4.4 ±1.1 nm and ~ -16 mV respectively with high colloidal stability due to the presence of stabilising serum protein [**Fig 5.2a**].

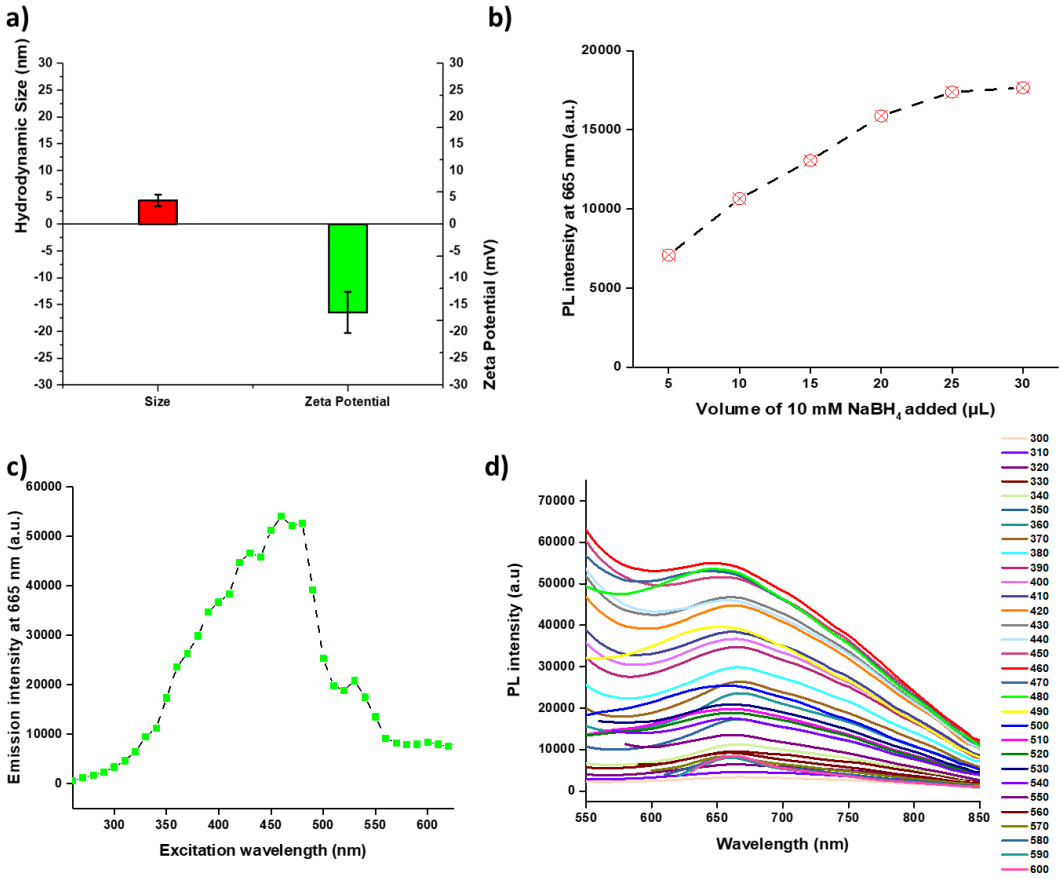

Fig 5.2: a) DLS and Zeta potential measurements of Ag-QCNS post synthesis. b) PL intensity at 665 nm as a function of volume of $NaBH_4$ added for PL intensity optimisation of Ag-QCNS during synthesis (λex 365 nm). c) Emission intensity recorded at λ_{max} (665 nm) for different excitation wavelengths and d) Excitation dependant emission mapping of Ag-QCNS.

The amount of reducing agent ($NaBH_4$) played a crucial role in deriving at optimal red photoluminescent clusters [**Fig 5.1c**, **and Fig 5.2b**]. The optimised red fluorescent Ag-QCNS recorded maximum emission intensity at 665 nm at an excitation wavelength of 460 nm **[Fig 5.1d, inset: under UV lamp & Fig 5.2c].** There was no obvious shift in the emission peak with different excitation wavelengths [**Fig 5.2 d]** indicating the photostability of fluorescent Ag-QCNS. The quantum yield was recorded with respect to rhodamine 6G (λ_{ex} ~488 nm) and was found to be ~ 6.63 %. The absorption spectra of Ag-QCNS depicted a shoulder peak ~ 410 nm and an onset peak at ~760nm, characteristic of the QCs so formed **[Fig 5.1e]**.

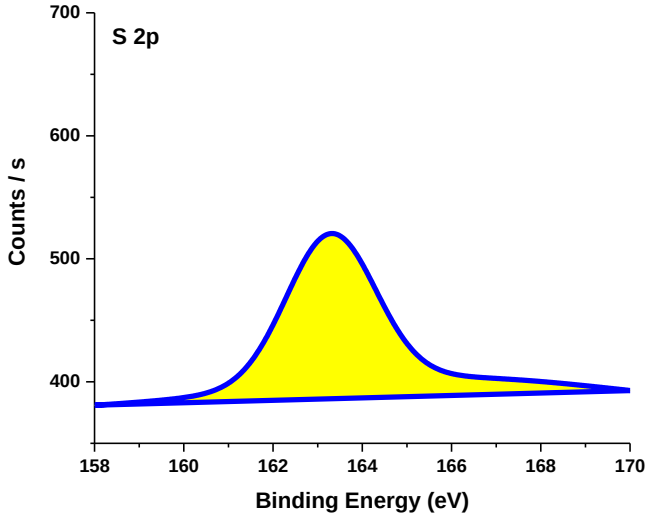

Fig 5.3: High-resolution S 2p XPS spectra for Ag-QCNS.

High resolution X-ray photoelectron spectroscopy of Ag-QCNS revealed Ag 3d spectra consists of two peaks Ag $3d_{5/2}$ (367.8 eV) and Ag $3d_{3/2}$ (373.8 eV) with a spin couple splitting difference of 6 eV as expected for Ag [**Fig 5.1f**]. The expanded spectra reveals that the peak is positioned closer to Ag (0) however, it should be noted that there is not much difference in the binding energy of Ag (0) and Ag (I), unlike in case of Au [28]. However, the absence of Ag(I) may be attributed to the use of a strong reducing agent that caused complete reduction of silver ions to metallic Ag [29]. The S 2p peak exists at 163.3 eV corresponding to metal-thiolate bond [**Fig 5.3**].

Further, circular dichroism spectroscopy was utilized to understand conformation changes of proteins post formation of QCNS. Native serum proteins depict a collective alpha helical conformation exhibited by two negative bands in the far UV region at 209 nm (π-π*) and 222 nm (n–π*) [**Fig 5.1g**]. However, in case of Ag QCNS, a partial unfolding of the proteins' alpha helical conformation is required to accommodate the Ag-thiol bonds. This is signified by descend in the peak at ~209 nm and ascend in peak at ~222 nm. Agarose gel electrophoresis was carried [**Fig 5.1h**] out in order to assess the heterogeneity of Ag-QCNS so formed, where a single band with similar running distance was observed as that of homogenous albumin stabilized BSA Ag_{15} QCs [15]. Since albumin is the major component of serum proteins (~ 60-70 %), hence the stabilisation of QCs predominantly with albumin protein is a major possibility. This is similar in pattern to the Au-QCNS formed using serum proteins when compared with BSA Au25 QCs [25]. TCSPC analysis indicated that Ag-QCNS undergoes a

bi-exponential decay [**Fig 5.1i**] and a shorter decay lifetime ζ_1=1.06 ns (41.74%) and ζ_2= 5.19 ns (58.26%) similar to earlier reports for albumin stabilised AgQCs [29]. The average lifetime (ζ_{avg}) was calculated to be ~ 4.67 ns. The dominant fast component on the nanosecond scale confirmed that the emission of Ag-QCNS is due to fluorescence, and not phosphorescence.

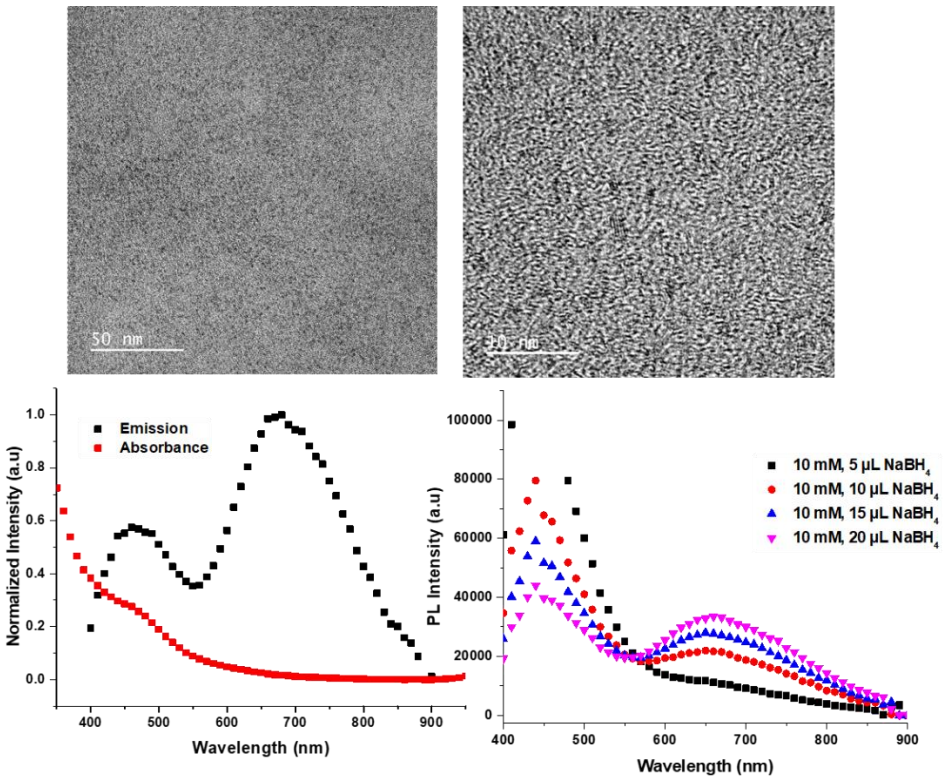

Fig 5.4: Characterisation panel for Human Ag-QCNS depicting TEM micrographs, optical (FL and Absorbance) spectroscopy and Optimisation of $NaBH_4$ for H Ag-QCNS.

Further, human serum stabilised Ag-QCNS were synthesized with a size distribution of 2.2± 0.3 nm with λ_{em} ~665 nm [**Fig 5.4**]. The absorbance peak at ~480 nm is similar to shoulder peak observed in albumin stabilised Ag_{15} QCs [15]. Here, the stepwise addition of $NaBH_4$ was optimised at 20 µL to give maximum emission intensity at 665 nm, due to variations in the serum components and protein content as compared to FBS used for Ag-QCNS synthesis.

5.2.2. Cellular Studies

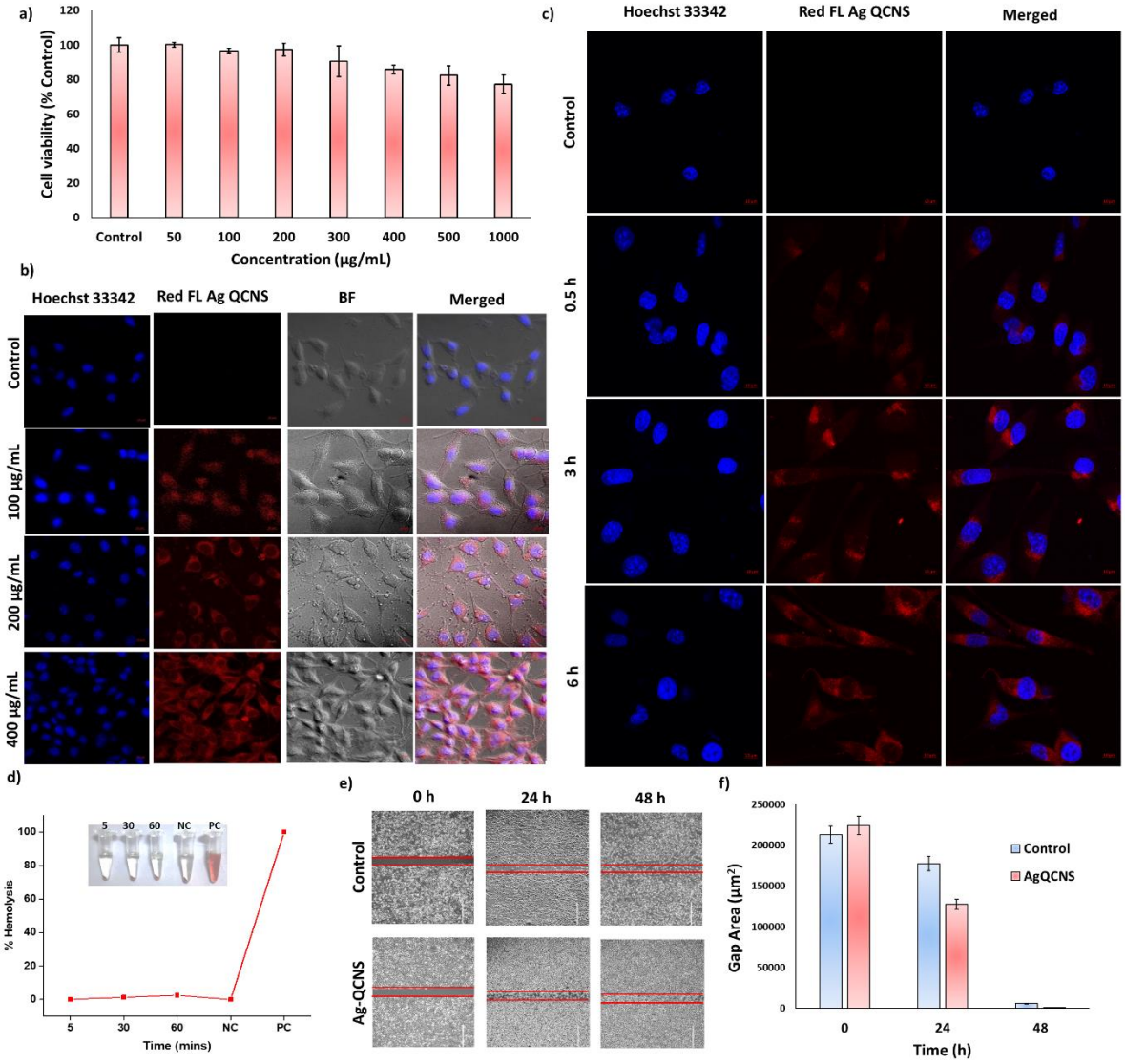

Fig 5.5: a) Biocompatibility of Ag-QCNS on murine fibroblast L929 cells at different concentrations after 24 h of treatment. CLSM images for b) concentration dependant uptake of Ag-QCNS on L929 cells after 24 h of treatment and c) time dependant uptake of Ag-QCNS (250 µg/mL: 12.7 µg/mL Ag equivalent) with L929 cells (scale bar-10 µm). d) *In-vivo* hemolysis assay for autologous murine Ag-QCNS after different exposure time periods. e) Bright field images of scratch area: Control and Ag-QCNS treated fibroblast cells at different time periods (magnification: 10x; Scale bar-100 µm). f) Migration assay depicting gap area coverage after treatment with Ag-QCNS (12.7 µg/mL Ag equivalent) at different time points.

The Ag-QCNS were found to be highly biocompatible in normal murine fibroblast L929 cells [**Fig 5.5a**]. The bright field images showed no changes in morphology of the cells after 24 hours of treatment [**Fig 5.6**]. The cellular internalisation of red photoluminescent Ag-QCNS in

normal L929 fibroblast cells was observed through confocal microscopy. The cellular nucleus was counter-stained in order to understand the localisation of Ag-QCNS. It was observed that the Ag-QCNS were preferentially accumulated in the cytoplasm in a concentration and time-dependant manner [**Fig 5.5b** and **Fig 5.5c**]. Moreover, Ag-QCNS did not cause any *in vivo* hemolysis [**Fig 5.5d**] as assessed at different time periods (5, 30, 60 mins) post intravenous dosage. The migratory effect of Ag-QCNS was studied in normal murine fibroblast cells using *in vitro* scratch assay and the gap area was plotted for different time periods from the images obtained under bright field microscope at pre-defined time intervals of 0, 24, 48 h [**Fig 5.5e** and **Fig 5.5f**]. It was observed that the gap area at the scratch site was ~ 28 % lesser (as compared to control) after treatment with Ag-QCNS for 24 h and completely healed within period of 48 h similar to control. Silver is known to play an active role in wound healing due to the effect of Ag^{+} ions towards differentiation of fibroblasts to myofibroblasts, which promote wound contraction and stimulation of proliferation and relocation of keratinocytes [26], [30], [31].

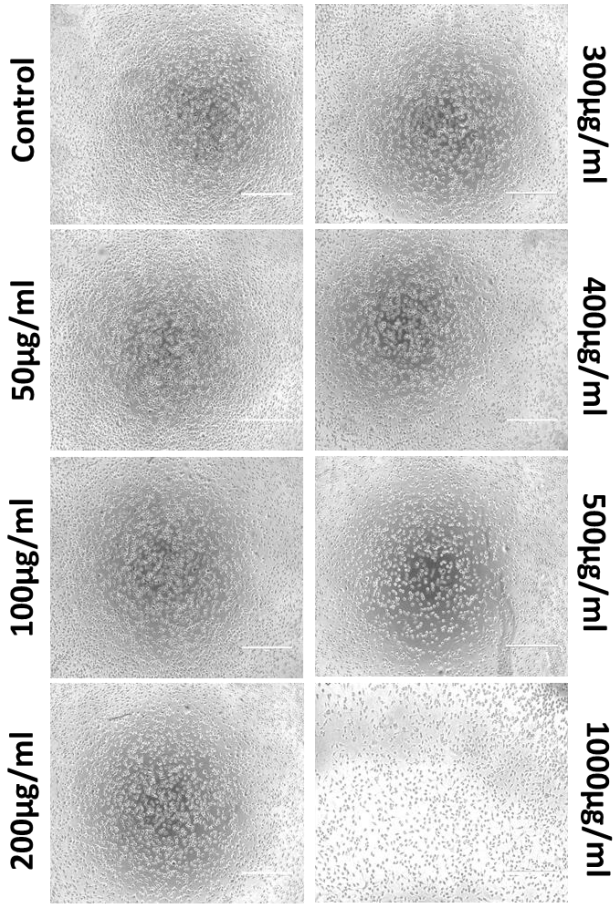

Fig 5.6: Bright field microscopic images of L929 cells after 24 h treatment with different Ag-QCNS concentrations. Scale Bar-200 µm.

5.2.3. Antibacterial activity of Ag QCNS

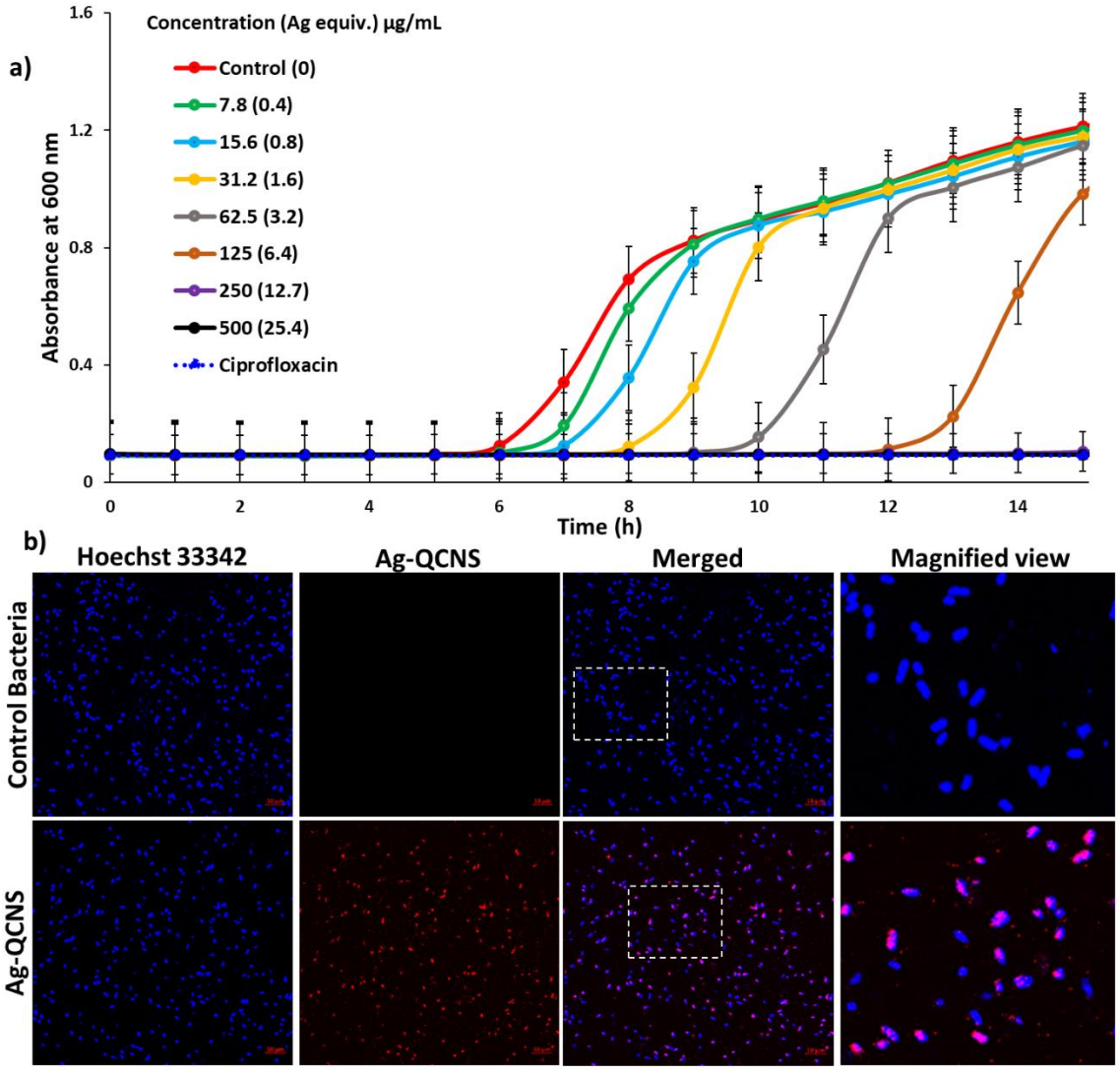

Fig 5.7:a) Bacterial overnight growth kinetics for *E.coli* at different Ag-QCNS concentrations with their corresponding Ag equivalent. Ciprofloxacin (2 mg/mL) was used as Positive control. b) Uptake of red photoluminescent Ag-QCNS (250 µg/mL: 12.7 µg/mL Ag equivalent) in bacteria post 12 h of treatment (counter-stained with Hoechst) analysed through CLSM at 63x magnification (scale bar-10 µm) and the magnified view of merged region depicting sufficient bacterial internalization of Ag-QCNS in 12 h.

Preliminary antibacterial activity was established by using *E.coli* as a model organism. Ag-QCNS inflicted a concentration dependant delay in the growth of bacteria with the silver concentration equivalence of 25.4 µg/mL imparting complete neutralization as that of the antibiotic, ciprofloxacin [**Fig 5.7a**]. Confocal microscopy confirmed strong interaction of Ag-QCNS with bacterial cells as a function of its bright fluorescence **[Fig 5.7b].** This association was further quantified with ICP-MS wherein bacteria treated with 12.7 µg/mL and 25.4 µg/mL.

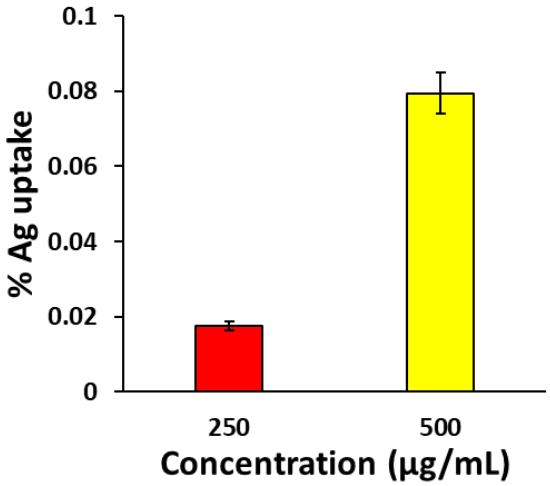

Fig 5.8: ICP-MS analysis for determining uptake of different concentrations of Ag-QCNS post 12 h of treatment with *E.coli* bacteria.

Ag equivalence yielded ~ 0.02 % and ~ 0.07 % Ag uptake at 12th hour of incubation with Ag-QCNS **[Fig 5.8]** indicating ~ 18 ng/mL to provide comparable anti-bacterial efficacy as that of ciprofloxacin.

Further, the presence of silver over the bacteria and concurrent structural damage it caused was clearly visualised with electron microscopic analysis. Both FESEM and TEM images confirmed that the bacteria treated with Ag-QCNS show a shrunk and shrivelled morphology [**Fig 5.9a**]. The bacterial cell membrane had significant perforations alongside evident fragmentation. Elemental mapping confirmed Ag to be predominantly associated with the bacteria [**Fig 5.9b & Fig 5.10**]. The loss of membrane integrity and the overall damage incurred by Ag-QCNS on the bacteria was quantified with live/dead differential staining [**Fig 5.9c**]. The damaged or dead bacteria with a compromised cell membrane allow the red florescent PI to diffuse into the damaged bacterial cells whereas the green FDA stained live and the metabolically active bacteria. After 12 hours of treatment with Ag-QCNS (250 µg/mL), ~ 90 % of bacterial cells were found to be dead while the untreated control recorded ~ 92 % live cells [**Fig 5.9d**].

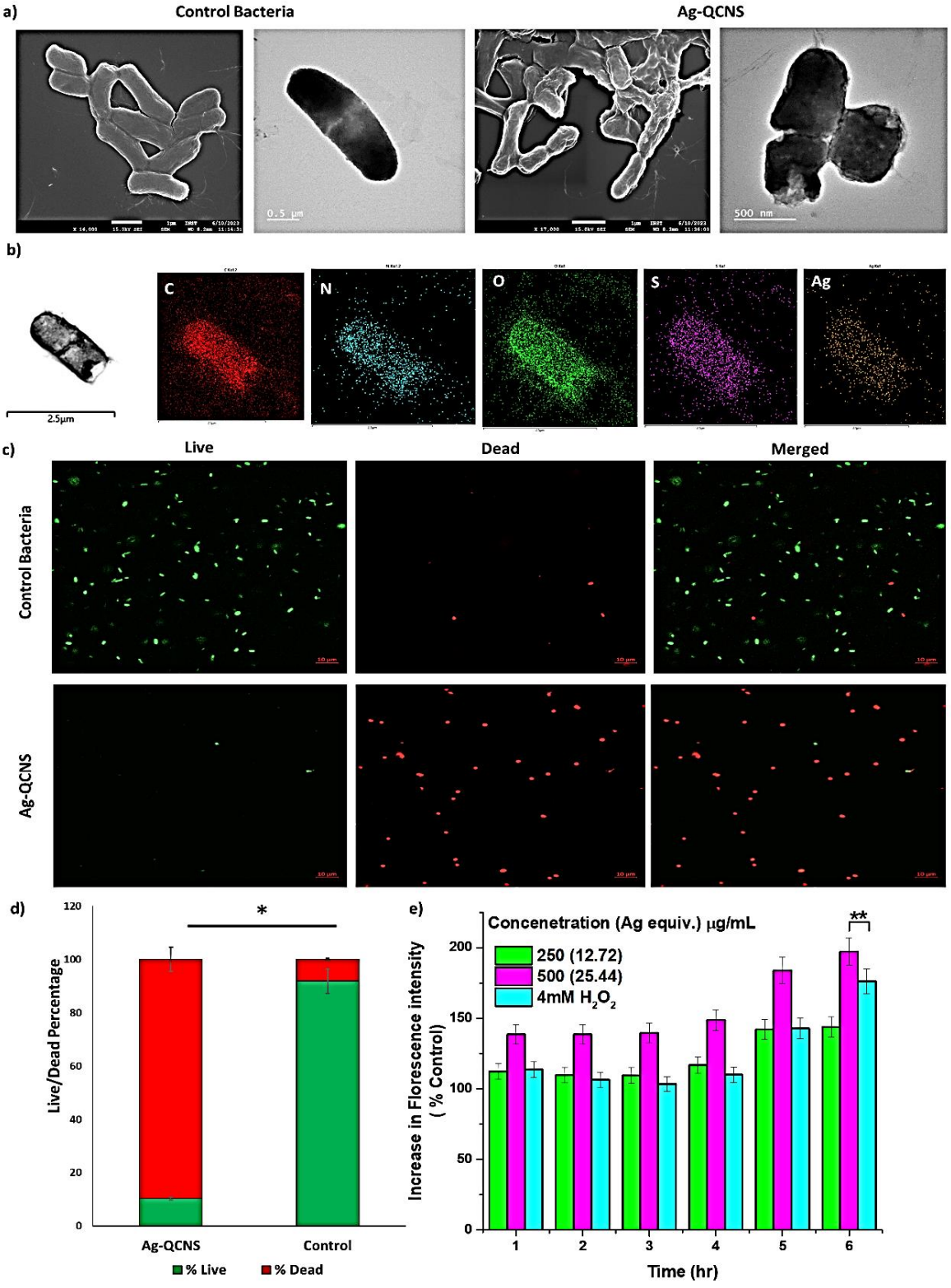

Fig 5.9: a) Electron microscopic analysis of control and Ag-QCNS (250 µg/mL: 12.7 µg/mL Ag equivalent) treated bacteria after 12 h of treatment and b) corresponding elemental analysis of Ag-QCNS treated bacteria. c) Live/Dead assay of control and Ag-QCNS (250 µg/mL) treated bacteria after 12 h of incubation (scale bar-10 µm) d) Live/Dead (%) calculated from fluorescent intensities using ImageJ software. e) Time dependant ROS estimation of bacteria after treatment with different Ag-QCNS concentrations. ** $p<0.01$ using Student's t test. 4 mM H_2O_2 was used as Positive control for ROS generation.

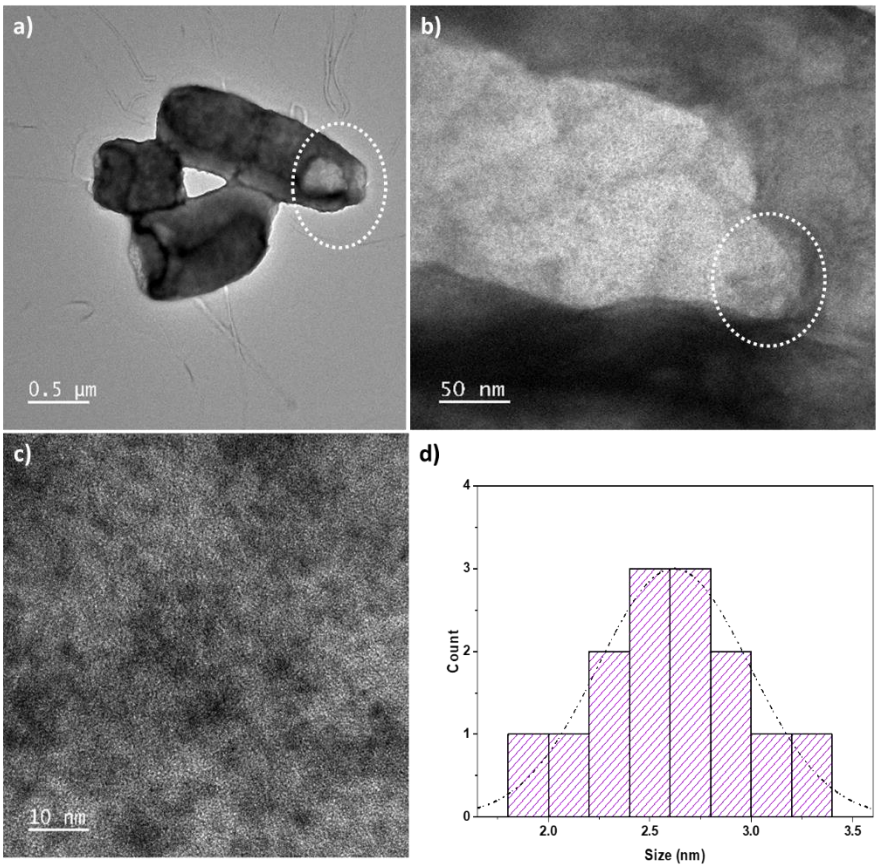

Fig 5.10: Ag-QCNS (250 µg/mL: 12.7 µg/mL Ag equivalent) treated *E.coli* revealed their bacterial internalisation through TEM imaging.

In order to probe the mechanism of antibacterial activity, the effect of acute oxidative stress was analysed post Ag-QCNS treatment up to 6 hours [**Fig 5.9e**]. The levels of intracellular reactive oxygen species was found to increase in a concentration and time-dependant manner. While QCNS at 12.7 µg/mL Ag equivalence induced similar oxidative stress as the positive control (4 mM hydrogen peroxide) in the earlier time points, at higher concentration of 25.4 µg/mL Ag equivalence ~ 200 % and ~ 12.5 % increase in oxidized DCF was measured as compared to negative control and positive control respectively. Ag-QCNS treated bacterial cells were evidently found to produce ROS at lower concentrations as well in a time-dependant manner [**Fig 5.11**]. This confirmed that oxidative stress is a key mechanism for the antibacterial activity of Ag-QCNS similar to other silver nanoparticles and quantum clusters [19], [32], [33]

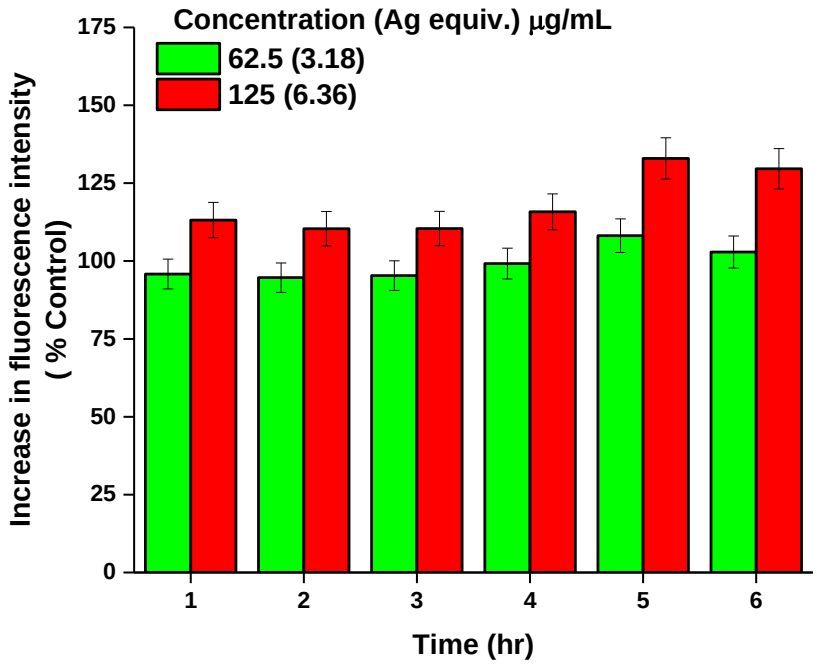

Fig 5.11: Time dependant ROS estimation with *E.coli* bacteria after treatment with lower concentrations of Ag-QCNS.

In order to assess the antimicrobial susceptibility of Ag-QCNS over a broad range of bacteria, the colony forming unit estimation assay was carried out with different Ag-QCNS concentrations on *E.coli*, *P. aeruginosa* and *S. aureus.* Percentage growth with respect to untreated control was plotted as shown in **Fig 5.12a, Fig 5.12b** and **Fig 5.12c** respectively. The representative bacterial colonies are depicted in **Fig 5.13**. The IC_{50} values were calculated and depicted as shown in **Table 5.1**. It was observed that QCNS showed an intermediate IC_{50} concentration against *E. coli* and slightly higher IC_{50} values against *S. aureus*. The lowest IC_{50} value for *P. aeruginosa* further strengthens the role of Ag-QCNS for faster wound healing applications as it is the most common bacterial pathogen found at any chronic infected wound site [35],[36]. In general, IC_{50} Ag-QCNS ~ 1.5-3.2 times lesser than IC_{50} AgNPs of different sizes (5-100 nm). The FESEM analysis of the gram-positive bacteria, *S. aureus* was carried out post Ag-QCNS treatment in order to assess any morphological changes. Significant cellular distortions and shrinkage were observed in *S. aureus* post treatment as seen in **Fig 5.12d**.

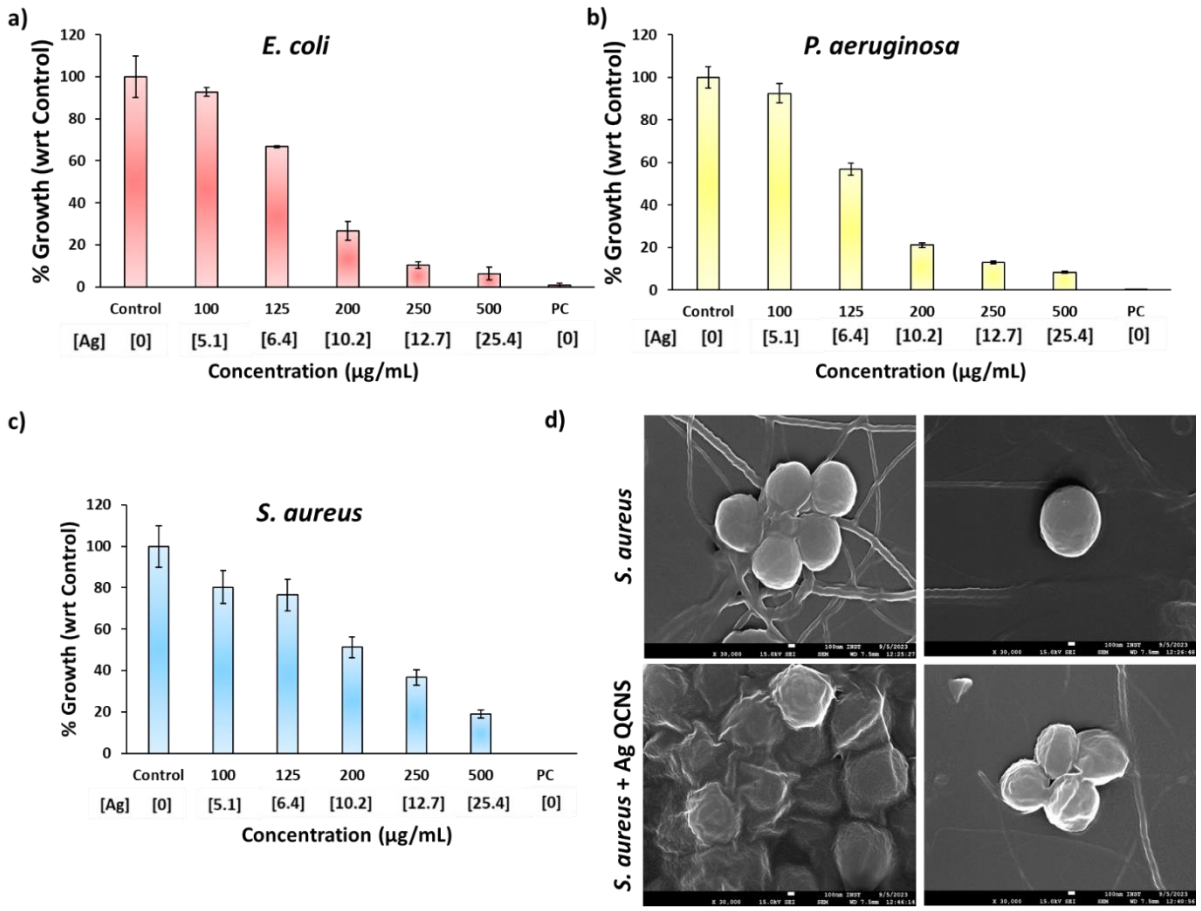

Fig 5.12:Percentage growth (wrt respective controls) post treatment with different Ag-QCNS concentrations depicting reduction in bacterial viability for a) *E. coli*; b) *P. aeruginosa* and c) *S. aureus*. d) FESEM analysis of *S. aureus* control and post 12 h of treatment with Ag-QCNS (250 µg/mL: 12.72 µg/mL Ag equivalent). Scale bar- 100 nm.

Table 5.1 Comparison of IC_{50} concentration values of Ag-QCNS (µg/mL) for different bacteria and their corresponding equivalent Ag content.

Bacterial samples	Half- maximal inhibitory concentration (IC_{50}) of Ag-QCNS (µg/mL)	Equivalent Ag content (approx. µg/mL)
E. coli	197.71 ± 4	10.06 ± 0.2
P. aeruginosa	190.87 ± 3	9.71 ± 0.15
S. aureus	253.08 ± 8	12.87 ± 0.41

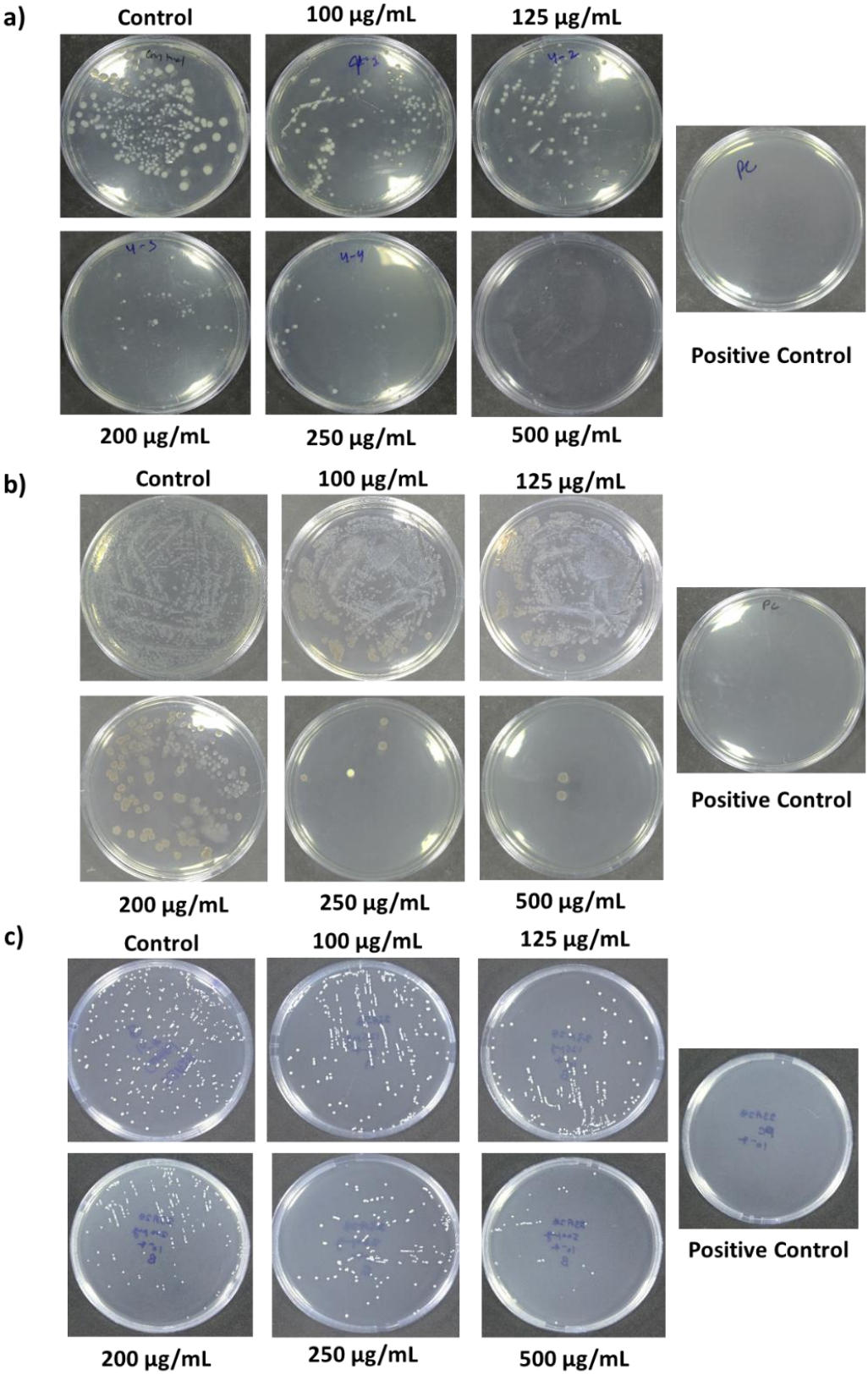

Fig 5.13: Representative colonies of: a) *E.coli* b) *P. aeruginosa* and c) *S. aureus* post 24 h treatment with different Ag-QCNS concentrations.

Furthermore, the effect of Ag-QCNS on antibiotic resistant bacteria was assessed using *E.coli* transfected with plasmid expressing Kanamycin resistance gene (*E.coli* ^{KRes}). The overnight

growth kinetics and subsequent agar plate streaking confirmed Ag-QCNS concentration dependence for effective inhibition of *E.coli* ^{KRes} growth [**Fig 5.15a** & **Fig 5.14a respectively**]. Morphological assessment through FESEM further confirmed these results wherein there was no significant damage post treatment with QCNS at 12.7 µg/mL Ag equivalence in comparison to control irrespective of its strong association as confirmed with elemental mapping [**Fig 5.15b ii, Fig 5.15c** and **Fig 5.14b**]. However, higher Ag-QCNS concentration (25.4 µg/mL Ag equivalence) inflicted complete bacterial fragmentation [**Fig 5.15b iii**].

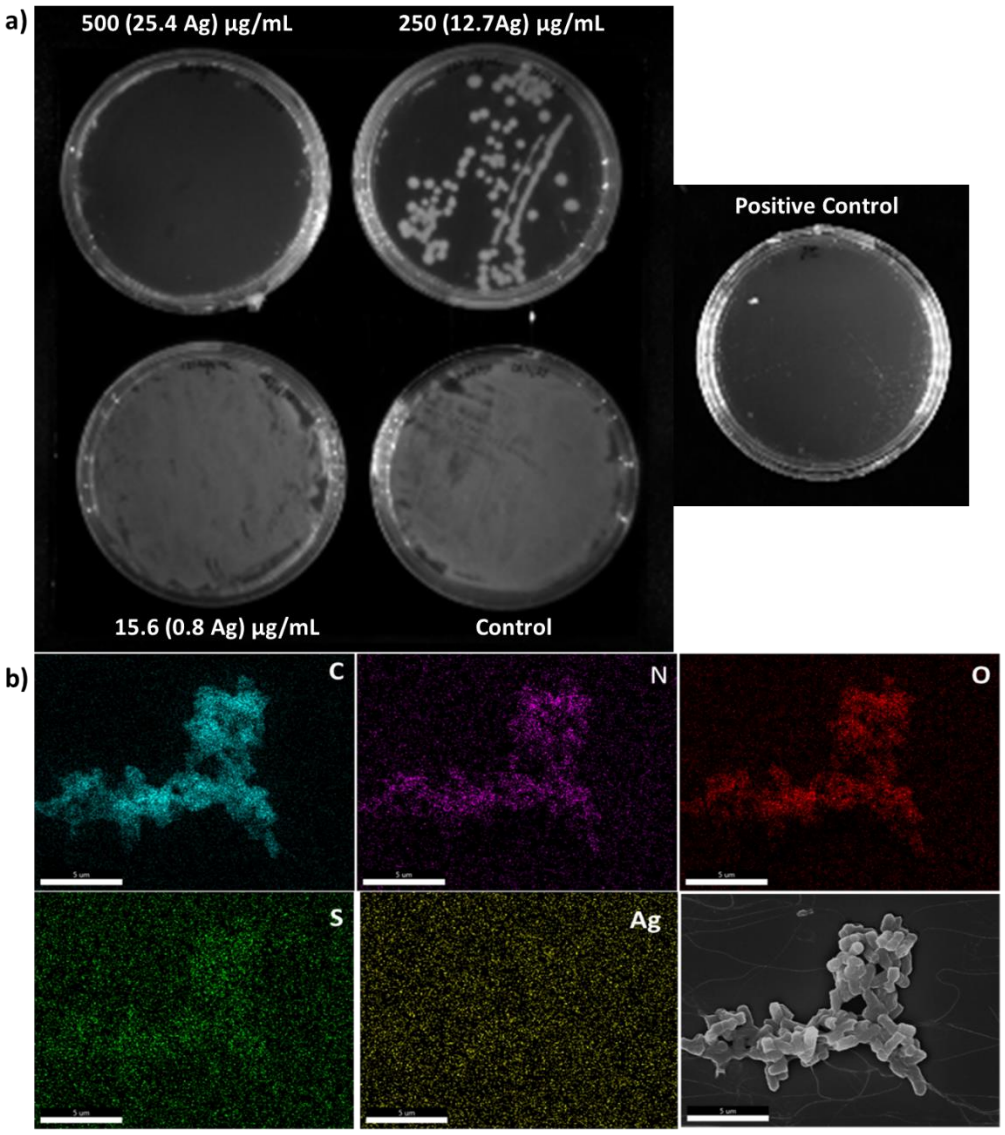

Fig 5.14: Image depicting growth of *E.coli* ^{KRes} bacteria post 24 h treatment of Ag-QCNS at lowest (0, 15.6 µg/mL) and highest (250, 500 µg/mL) concentrations. b) Elemental mapping of control *E.coli* ^{KRes} bacteria. Scale Bar- 5 µm.

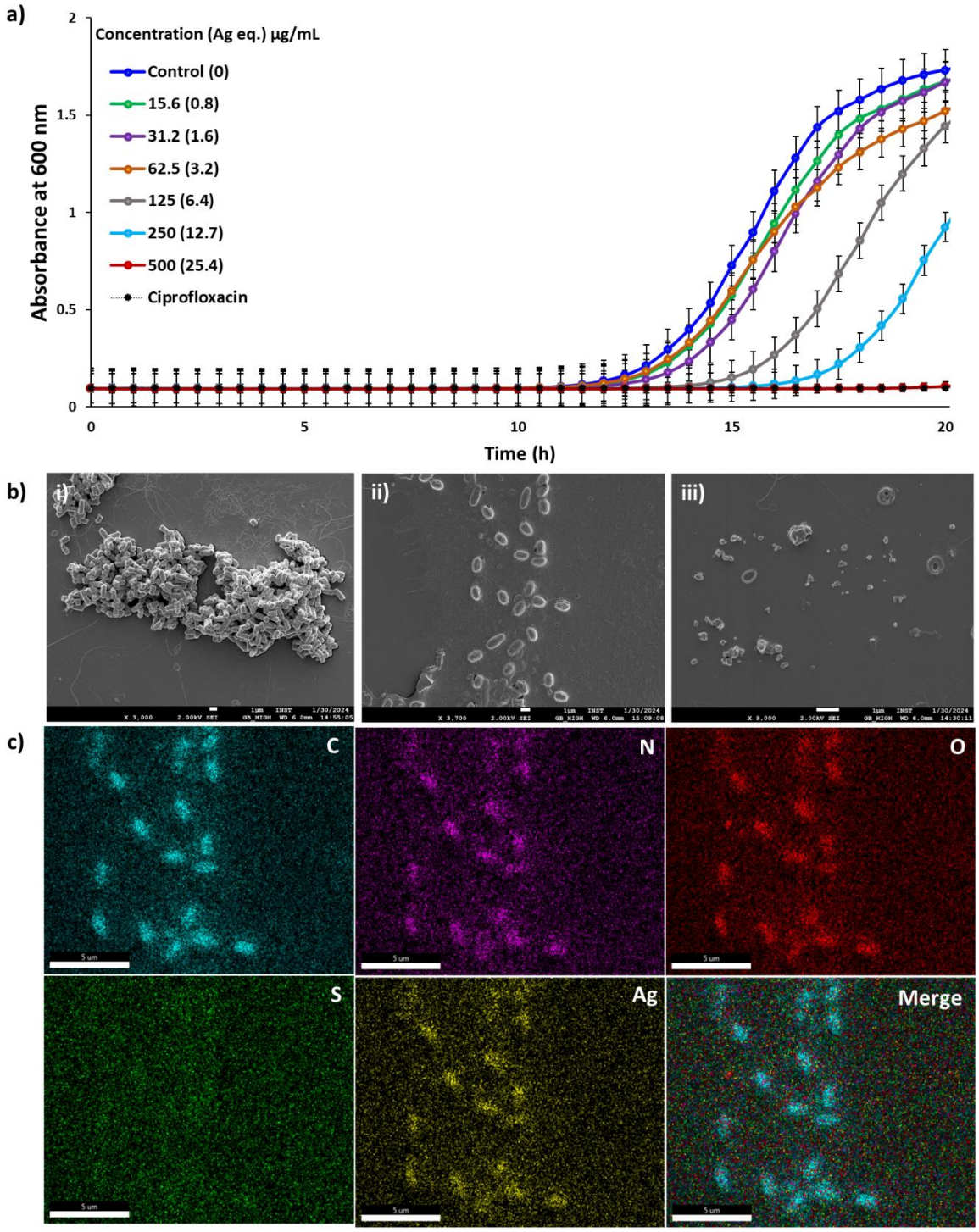

Fig 5.15: a) Growth kinetics for antibiotic resistant *E.coli* ^{KRes} at different Ag-QCNS concentrations with their corresponding Ag equivalent. Ciprofloxacin (2 mg/mL) was used as Positive control. b) FESEM images of i) Control and ii) 250 µg/mL (12.72 µg/mL Ag equivalent) and iii) 500 µg/mL (25.44 µg/mL Ag equivalent) Ag-QCNS treated *E.coli* ^{KRes} bacteria post 12 h of treatment and c) corresponding elemental mapping of bacteria from b (ii) depicting Ag uptake at 12 h. Scale Bar- 5 µm.

Even though the growth was not completely inhibited at lower concentrations, Ag-QCNS prolonged the lag phase by several hours for both antibiotic sensitive and resistant strains of

E.coli as shown in **Fig 5.16,** which is often due to oxidative stress. This data is in consistence with **Fig 5.11** wherein lower concentrations of drug sensitive *E.coli* had depicted ROS formation post treatment. Henceforth, an optimum working concentration of Ag-QCNS was required to effectively inhibit the growth and complete destruction of different bacterial strains.

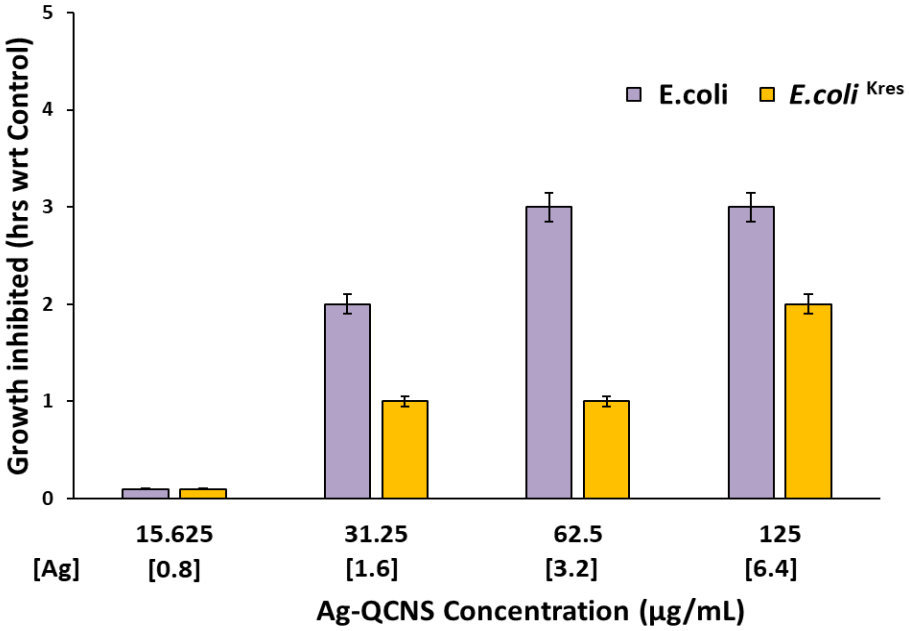

Fig 5.16: Prolonged lag-phase of *E.coli* and *E.coli* ^{KRes} strains after treatment with lower concentrations of Ag-QCNS.

5.2.4. Preclinical Safety Assessment of autologous mice serum stabilised silver nanoclusters

For preclinical assessment, murine autologous serum stabilised Ag-QCNS were utilized [**Fig 5.17**] with a single intravenous dosing of ~0.44 mg/kg Ag equivalent for acute & sub-acute toxicity determination on day-1 and day-28 days [**Fig 5.18a**].

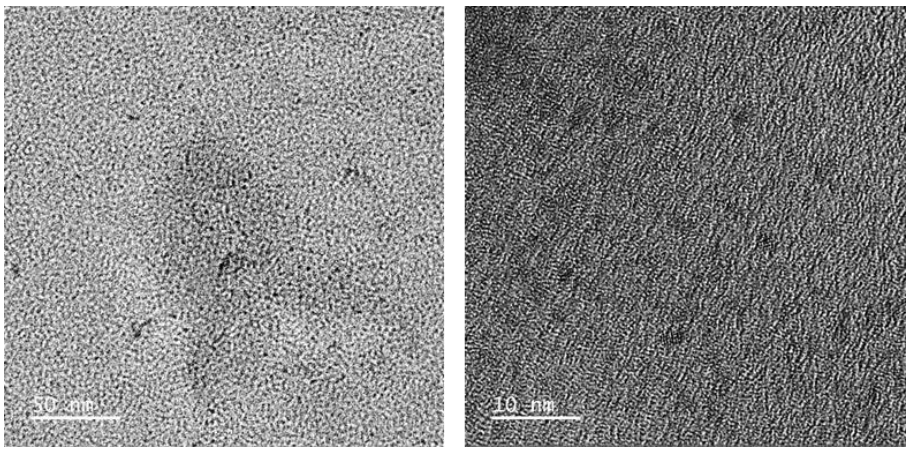

Fig 5.17: TEM analysis of Murine Ag-QCNS.

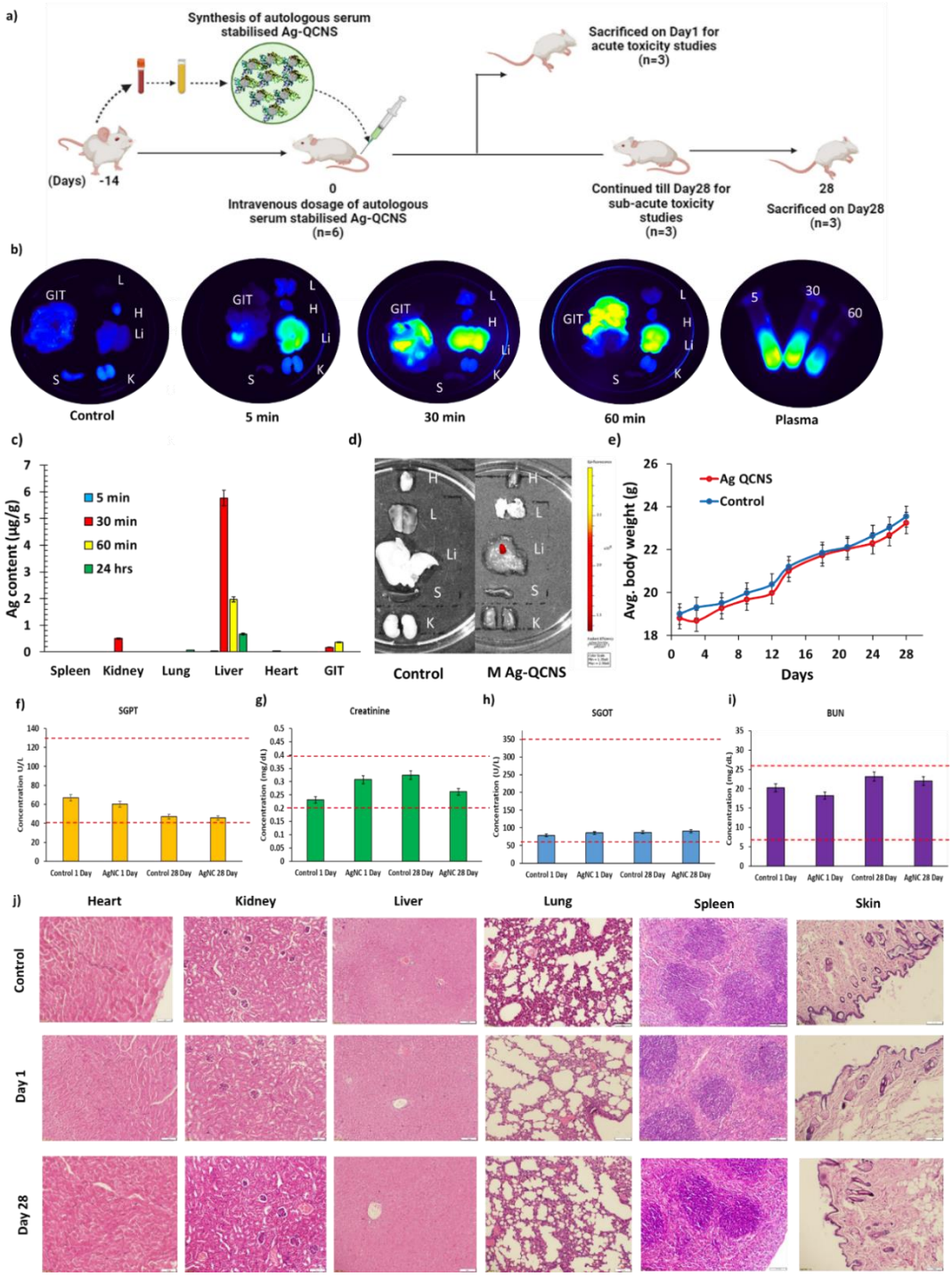

Fig 5.18: a) Schematic depicting analysis schedule for preclinical safety assessment in Balb/c mice for acute and sub-acute toxicity assessment. b) Short-term *ex-vivo* pharmacokinetic biodistribution of autologous ICG-tagged M Ag-QCNS at different time periods. Labelling indicates lungs (L), heart (H), Liver (Li), kidney (K), spleen (S) and gastrointestinal tract (GIT). c) ICP-MS analysis for Ag content in vital organs. d) *Ex-vivo* IVIS imaging post 24 h of ICG-tagged autologous M Ag-QCNS injection. e) Body weight of mice (Control and Ag-QCNS treated) over treatment schedule f) Acute and sub-acute vital organ functioning tests for SGPT, g) Creatinine, h) SGOT, and i) BUN. j) Histopathological analysis of vital organs on Day 1 and Day 28 post injection. Scale bar-100 µm.

Short-term biodistribution was carried out in Balb/c mice post intravenous injection of ICG tagged Ag-QCNS at different time points (i.e., 5 minutes, 30 minutes, 1 hour) and the vital

organs were imaged *ex-vivo* [**Fig 5.18b**]. While Ag-QCNS were in systemic circulation for up to 60 minutes, they started to localise predominantly in the liver within 30 minutes followed by biliary secretion into the gastrointestinal tract. This observation was confirmed with quantification of silver in the organs using ICP-MS, where Ag-QCNS were predominantly present in liver (i.e. ~0.03 µg/g in 5 minutes to 5.76 µg/g in 30 minutes) and gradually increased their localisation in GIT from 0.17 µg/g to 0.36 µg/g within next 30 minutes[**Fig 5.18c**]. However, the liver showed a gradual decline in Ag-QCNS localisation (~1.96 µg/g at 60 mins). Post 24 hours, both fluorescence imaging and ICP-MS analysis indicated significant decrease in silver content in the liver (~0.67 µg/g) possibly due to re-circulation and re-absorption of the albumin proteins [**Fig 5.18d** & **Fig 5.18c**]. This is consistent to our previously reported findings for autologous Au-QCNS wherein they were localised in liver predominantly [25]. Since albumin is a major component of serum and plays a significant role in stabilising of Ag-QCNS, hence the *in vivo* fate might be similar to Au-QCNS.

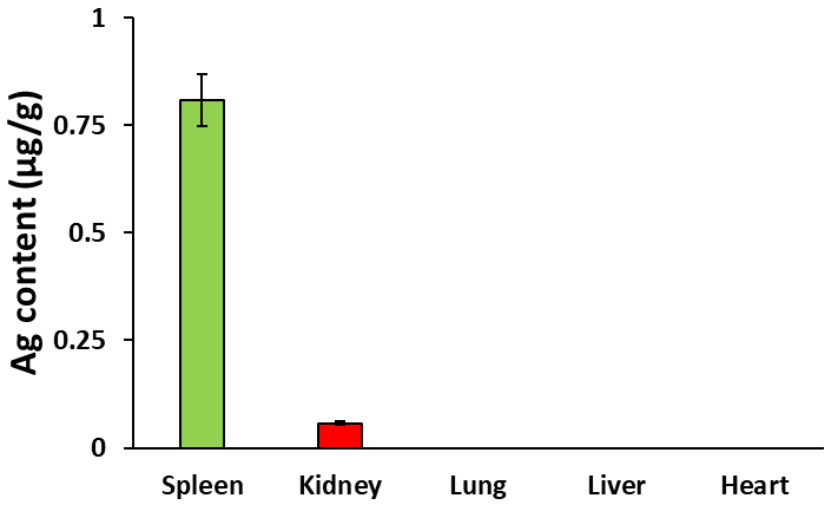

Fig 5.19: ICP-MS analysis of Ag content in vital organs on Day-28 p.i.

At the end of Day 28, only marginal quantities of Ag-QCNS were present in spleen (~0.8 µg/g) and in kidney (~0.05 µg/g) [**Fig 5.19**]. This is in consistence with the albumin stabilised QCs that have been reported to accumulate in spleen with possible clearance of Ag-QCNS through a combination of renal and hepatobiliary clearance routes considering their size is less than 6-8nm [36][37]. Over the duration of study, there was no significant change in the body weight of Ag-QCNS injected mice **[Fig 5.19e]** and underwent growth rate similar to a healthy mice.

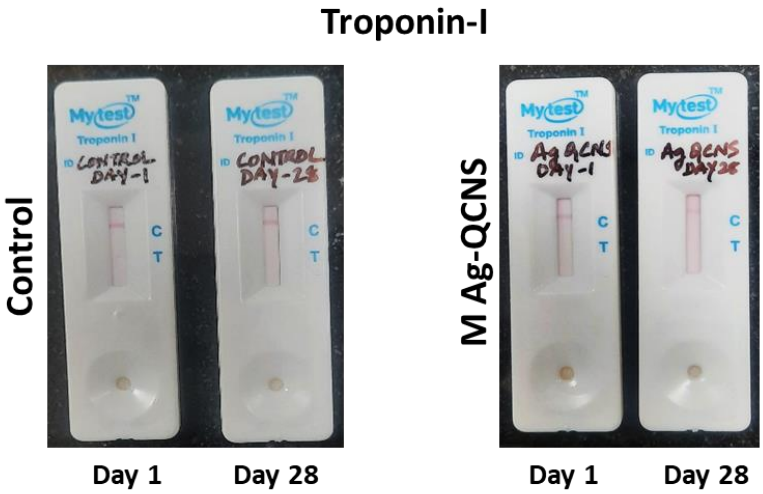

Fig 5.20: Troponin-I analysis depicting no cardiotoxicity for saline and M Ag-QCNS dosed mice on Day 1 and Day 28 p.i.

The proper functioning of vital organs such as liver, kidney and heart were quantified for serum biomarkers such as aspartate aminotransferase, alanine aminotransferase, blood urea nitrogen, creatinine and qualitatively for Troponin-I at Day-1 and Day-28 post treatment. All vital markers were found to be well within the normal reference range for Balb/c mice and comparable to control animals depicting no obvious signs of acute and sub-acute toxicity from Ag-QCNS [**Fig 5.19 (f-i)** & **Fig 5.20]**.

The histopathological analysis of vital organs including skin was carried out with hematoxylin and eosin staining [**Fig 5.19 k]**. There were no changes observed in tissue microarchitecture as well as no signs of infiltrating inflammatory cells confirming absence of any toxicity. Hence, autologous Ag-QCNS was observed to be safe for further preclinical and clinical applications.

5.3. Conclusions and Future Prospects

Ag-QCNS have the potential to act as host-specific antibacterial agents with real time monitoring of antibacterial activity due to their bright red photoluminescence properties. We have demonstrated their antibacterial effect on *E.coli*, both antibiotic sensitive and resistant strains. Furthermore, antimicrobial assessment was extended with *Staphylococcus aureus* and *Pseudomonas aeruginosa* to examine the overall antimicrobial susceptibility of Ag-QCNS. The Ag-QCNS were found to acutely accumulate in liver and follow a biliary excretion pathway during short-term pharmacokinetic biodistribution evaluation. Preclinical safety assessment of host-specific autologous serum stabilised Ag-QCNS was established in Balb/c mice model with no notable changes in serum biomarkers and absence of any atypical signature found in tissue microarchitecture for 24 hour and 28 days post injection. The antimicrobial

efficacy of Ag-QCNS can be enhanced by conjugating clinically approved antibiotics for optimal use in order to decrease their dosage as well as for combating different antibiotic resistant strains as a novel personalised anti-bacterial alternative.

References:

[1] L. J. Shallcross, S. J. Howard, T. Fowler, and S. C. Davies, "Tackling the threat of antimicrobial resistance: from policy to sustainable action.," *Philos. Trans. R. Soc. London. Ser. B, Biol. Sci.*, vol. 370, no. 1670, p. 20140082, Jun. 2015.

[2] R. Paul, "State of the Globe: Rising Antimicrobial Resistance of Pathogens in Urinary Tract Infection.," *Journal of global infectious diseases*, vol. 10, no. 3. India, pp. 117–118, 2018.

[3] V. Puca *et al.*, "Microbial Species Isolated from Infected Wounds and Antimicrobial Resistance Analysis: Data Emerging from a Three-Years Retrospective Study.," *Antibiot. (Basel, Switzerland)*, vol. 10, no. 10, Sep. 2021.

[4] G. A. Martínez-Castañón, N. Niño-Martínez, F. Martínez-Gutierrez, J. R. Martínez-Mendoza, and F. Ruiz, "Synthesis and antibacterial activity of silver nanoparticles with different sizes," *J. Nanoparticle Res.*, vol. 10, no. 8, pp. 1343–1348, 2008.

[5] Z. Xiu, Q. Zhang, H. L. Puppala, V. L. Colvin, and P. J. J. Alvarez, "Negligible Particle-Specific Antibacterial Activity of Silver Nanoparticles," *Nano Lett.*, vol. 12, no. 8, pp. 4271–4275, Aug. 2012.

[6] L. Rizzello and P. P. Pompa, "Nanosilver-based antibacterial drugs and devices: Mechanisms{,} methodological drawbacks{,} and guidelines," *Chem. Soc. Rev.*, vol. 43, no. 5, pp. 1501–1518, 2014.

[7] K. Zheng, X. Yuan, N. Goswami, Q. Zhang, and J. Xie, "Recent advances in the synthesis{,} characterization{,} and biomedical applications of ultrasmall thiolated silver nanoclusters," *RSC Adv.*, vol. 4, no. 105, pp. 60581–60596, 2014.

[8] Z. Luo, K. Zheng, and J. Xie, "Engineering ultrasmall water-soluble gold and silver nanoclusters for biomedical applications," *Chem. Commun.*, vol. 50, no. 40, pp. 5143–5155, 2014.

[9] S. Javani, R. Lorca, A. Latorre, C. Flors, A. L. Cortajarena, and Á. Somoza, "Antibacterial Activity of DNA-Stabilized Silver Nanoclusters Tuned by Oligonucleotide Sequence," *ACS Appl. Mater. Interfaces*, vol. 8, no. 16, pp. 10147–10154, Apr. 2016.

[10] P. Gao, H. Wang, G. Zou, and K.-Q. Zhang, "Silk fibroin-derived peptide directed silver nanoclusters for cell imaging," *RSC Adv.*, vol. 8, no. 49, pp. 27805–27810, 2018.

[11] X. Sun, S. Dong, and E. Wang, "One-Step Preparation and Characterization of Poly(propyleneimine) Dendrimer-Protected Silver Nanoclusters," *Macromolecules*, vol. 37, no. 19, pp. 7105–7108, Sep. 2004.

[12] K. Hurtuková *et al.*, "Antibacterial Properties of Silver Nanoclusters with Carbon Support on Flexible Polymer," *Nanomaterials*, vol. 12, no. 15, 2022.

[13] W. Gao, X. Wang, W. Xu, and S. Xu, “Luminescent composite polymer fibers: In situ synthesis of silver nanoclusters in electrospun polymer fibers and application,” *Mater. Sci. Eng. C*, vol. 42, pp. 333–340, 2014.

[14] J. Xie, Y. Zheng, and J. Y. Ying, “Protein-Directed Synthesis of Highly Fluorescent Gold Nanoclusters,” *J. Am. Chem. Soc.*, vol. 131, no. 3, pp. 888–889, Jan. 2009.

[15] A. Mathew, P. R. Sajanlal, and T. Pradeep, “A fifteen atom silver cluster confined in bovine serum albumin,” *J. Mater. Chem.*, vol. 21, no. 30, pp. 11205–11212, 2011.

[16] S. Kalita, R. Kandimalla, A. C. Bhowal, J. Kotoky, and S. Kundu, “Functionalization of β-lactam antibiotic on lysozyme capped gold nanoclusters retrogress MRSA and its persisters following awakening,” *Sci. Rep.*, vol. 8, no. 1, p. 5778, 2018.

[17] D. P. Linklater *et al.*, “Lethal Interactions of Atomically Precise Gold Nanoclusters and Pseudomonas aeruginosa and Staphylococcus aureus Bacterial Cells,” *ACS Appl. Mater. Interfaces*, vol. 14, no. 28, pp. 32634–32645, 2022.

[18] K. Zheng, M. I. Setyawati, D. T. Leong, and J. Xie, “Antimicrobial Gold Nanoclusters,” *ACS Nano*, vol. 11, no. 7, pp. 6904–6910, Jul. 2017.

[19] K. Zheng, M. I. Setyawati, T.-P. Lim, D. T. Leong, and J. Xie, “Antimicrobial Cluster Bombs: Silver Nanoclusters Packed with Daptomycin,” *ACS Nano*, vol. 10, no. 8, pp. 7934–7942, Aug. 2016.

[20] L. Mei *et al.*, “Silver Nanocluster-Embedded Zein Films as Antimicrobial Coating Materials for Food Packaging,” *ACS Appl. Mater. Interfaces*, vol. 9, no. 40, pp. 35297–35304, Oct. 2017.

[21] J. Wu *et al.*, “Responsive Assembly of Silver Nanoclusters with a Biofilm Locally Amplified Bactericidal Effect to Enhance Treatments against Multi-Drug-Resistant Bacterial Infections,” *ACS Cent. Sci.*, vol. 5, no. 8, pp. 1366–1376, 2019.

[22] N. Kundu, D. Mukherjee, T. K. Maiti, and N. Sarkar, “Protein-Guided Formation of Silver Nanoclusters and Their Assembly with Graphene Oxide as an Improved Bioimaging Agent with Reduced Toxicity,” *J. Phys. Chem. Lett.*, vol. 8, no. 10, pp. 2291–2297, May 2017.

[23] L.-A. Pirofski and A. Casadevall, “Antimicrobial Therapy in the Context of the Damage-Response Framework: the Prospect of Optimizing Therapy by Reducing Host Damage.,” *Antimicrob. Agents Chemother.*, vol. 64, no. 2, Jan. 2020.

[24] Mimansa, M. Jamwal, R. Das, and A. Shanavas, “High Drug Loading Nanoparticles Stabilized with Autologous Serum Proteins Passively Inhibits Tumor Growth.,” *Biomacromolecules*, vol. 23, no. 12, pp. 5065–5073, Dec. 2022.

[25] K. Sood, P. Yadav, M. Jamwal, R. Das, and A. Shanavas, “Preclinical safety assessment of photoluminescent metal quantum clusters stabilized with autologous serum proteins for host specific theranostics.,” *Nanotheranostics*, vol. 7, no. 3, pp. 316–326, 2023.

[26] P. D. Krishnan *et al.*, “Silver Nanomaterials for Wound Dressing Applications,” *Pharmaceutics*, vol. 12, no. 9. 2020.

[27] A. Munteanu, I. P. Florescu, and C. Nitescu, “A modern method of treatment: The role of silver dressings in promoting healing and preventing pathological scarring in

patients with burn wounds.," *J. Med. Life*, vol. 9, no. 3, pp. 306–315, 2016.

[28] I. Chakraborty, T. Udayabhaskararao, and T. Pradeep, "High temperature nucleation and growth of glutathione protected ∼Ag75 clusters," *Chem. Commun.*, vol. 48, no. 54, pp. 6788–6790, 2012.

[29] X. Le Guével, B. Hötzer, G. Jung, K. Hollemeyer, V. Trouillet, and M. Schneider, "Formation of Fluorescent Metal (Au, Ag) Nanoclusters Capped in Bovine Serum Albumin Followed by Fluorescence and Spectroscopy," *J. Phys. Chem. C*, vol. 115, no. 22, pp. 10955–10963, Jun. 2011.

[30] T. Gunasekaran, T. Nigusse, and M. D. Dhanaraju, "Silver nanoparticles as real topical bullets for wound healing.," *J. Am. Coll. Clin. Wound Spec.*, vol. 3, no. 4, pp. 82–96, Dec. 2011.

[31] F. Paladini and M. Pollini, "Antimicrobial Silver Nanoparticles for Wound Healing Application: Progress and Future Trends.," *Mater. (Basel, Switzerland)*, vol. 12, no. 16, Aug. 2019.

[32] H. Xu *et al.*, "Role of reactive oxygen species in the antibacterial mechanism of silver nanoparticles on Escherichia coli O157:H7.," *Biometals an Int. J. role Met. ions Biol. Biochem. Med.*, vol. 25, no. 1, pp. 45–53, Feb. 2012.

[33] X. Yuan, M. I. Setyawati, A. S. Tan, C. N. Ong, D. T. Leong, and J. Xie, "Highly luminescent silver nanoclusters with tunable emissions: cyclic reduction–decomposition synthesis and antimicrobial properties," *NPG Asia Mater.*, vol. 5, no. 2, pp. e39–e39, 2013.

[34] K. Kirketerp-Møller *et al.*, "Distribution, organization, and ecology of bacteria in chronic wounds.," *J. Clin. Microbiol.*, vol. 46, no. 8, pp. 2717–2722, Aug. 2008.

[35] K. Rahim, S. Saleha, X. Zhu, L. Huo, A. Basit, and O. L. Franco, "Bacterial Contribution in Chronicity of Wounds," *Microb. Ecol.*, vol. 73, no. 3, pp. 710–721, 2017.

[36] X.-D. Zhang, D. Wu, X. Shen, P.-X. Liu, F.-Y. Fan, and S.-J. Fan, "In vivo renal clearance, biodistribution, toxicity of gold nanoclusters," *Biomaterials*, vol. 33, no. 18, pp. 4628–4638, 2012.

[37] Y.-N. Zhang, W. Poon, A. J. Tavares, I. D. McGilvray, and W. C. W. Chan, "Nanoparticle–liver interactions: Cellular uptake and hepatobiliary elimination," *J. Control. Release*, vol. 240, pp. 332–348, 2016.

Chapter 6

Summary and Outlook

To summarize, we have developed both plasmonic and photoluminescent noble metal nanostructures (Au and Ag) and employed them for addressing the challenges in cancer and infectious diseases management. The thesis focussed on facilitating the ease of design and utility of nanostructures and potentially mitigating the risk of adverse side effects and immunogenicity using personalised nanomedicine.

The first part of the thesis deals with developing a novel and interesting approach for synthesising gold semi shells (SS) by employing a rapid colloidal procedure involving pH degradable MOF structures. Herein, we have addressed the limitations faced during the fabrication of metallic SS involving the use of toxic template precursors, sophisticated instrumentations, long tedious, multi-step procedures at high temperatures and addition of etching agents to dissolve the templates. The reported one-pot colloidal procedure aims to facilitate the synthesis of metallic SS with minimal laboratory requirements and their subsequent utilization in diverse fields such as therapeutic and sensing applications. The anisotropic SS, due to their unique and anisotropic morphology, exhibited LSPR in the NIR region allowing use as photo-nanotransducers for therapeutic applications. PEGylation of SS not only prevented them from aggregation and improved colloidal stability but also acted as a cryoprotectant and aided in retaining their optical property post lyophilisation. Readily reconstitutable SS powder therefore emerged advantageous for enhancing the shelf-life of nanomaterials for on-demand usage. The SS were found to be photothermally stable and recyclable up to 5 cycles at 1W power. As for the future prospects, the synthetic methodology utilized for SS could be further explored for other metals such as Ag and Cu, offering opportunities to develop cost-effective photothermal nanotransducers. Additionally, the SS formation process could be adapted and assessed with various MOF structures to evaluate the viability of colloidal synthesis methods.

Consequently, we employed the colloidal PEGylated gold SS for the photothermal ablation of breast tumor. Firstly, compatibility of SS with RBCs and biocompatibility in normal HUVEC cell line was established. Next, we evaluated the *in-vitro* photothermal ablation ability against breast cancer MDA MB 231 cells with 808 nm laser and found that within 10 minutes of laser irradiation with a biocompatible concentration of 100 µg/mL, we could observe high

cytotoxicity results. All these encouraging *in-vitro* results led us to assess the acute and sub-acute preclinical safety and immunogenicity assessment in C57BL/6 mice post dual dosage of 25 mg/Kg equivalent to Au content of ~5mg/kg. There was no acute inflammatory response in PEG SS dosed mice, ruling out any immunogenic effects. The serum biochemical parameters and histopathological analysis ruled out any acute and sub-acute damage post single and dual dosage for a period of 28 days. The preclinical tumor regression was studied in CD1 nude mice xenografted with 4T1 breast tumor cells and was found to efficiently inhibit the primary tumor load along with lung and bone metastasis inhibition. Thereafter, a survival study in 4T1 syngeneic Balb/c tumor mice model was conducted revealing a 75% relapse-free survival for a period of 3 months. Hence, the gold SS mediated photothermal therapy is not only expected to depict photothermal ablation and metastatic inhibition of breast tumor cells but also to increase the chances of survival in patients in a clinical setting and thus exhibit high translational potential. Furthermore, through the integration of combinatorial chemo/photothermal therapy, it is anticipated that the expected outcomes will be enhanced owing to the synergistic effects. Moreover, evaluating a biocompatible membrane coating over the drug-conjugated SS could be explored for its potential to improve stability and efficacy in cancer theranostic applications.

In the later part of the thesis, we delved into host-specific nanomedicine by synthesising red photoluminescent whole serum protein stabilised gold quantum clusters (Au-QCNS). The Au-QCNS were predominantly stabilised by serum albumin which is the most abundant protein found in the serum. However, the other major serum proteins such as globulins and lipoproteins also have the basic chemical composition required to stabilize QCs. As expected, the Au-QCNS were found to be highly biocompatible and hemocomaptible *in-vitro*. The ability of Au-QCNS to act as radiosensitizers was exhibited in hepatoma PLC/PRF/5 cells with differential ɤ-radiation doses. It was found that hepatoma cells treated with 100 µg/mL Au-QCNS with 5Gy irradiation lead to enhanced ROS production which ultimately lead to complete nuclear and cytoskeletal damage as exhibited by confocal microscopy. The acute and sub-acute preclinical safety analysis was carried out using mice autologous serum protein stabilised Au-QCNS in C57BL/6 mice. The inflammatory cytokine analysis revealed non-immunogenicity post intravenous injection. The Au-QCNS were found in liver and spleen similar to albumin stabilised Au_{25} QCs. However, further evaluation of Au-QCNS for long term biodistribution and their in-depth excretory pathway analysis would be beneficial for strategizing their application in personalized theranostics. The serum biochemical parameters assessing the vital

organ functioning of liver and kidney using ALT/AST, urea and creatinine in addition to the tissue histopathological analysis indicated that in general that Au-QCNS is safe with double dosage intravenous administration indicating their potential for clinical translation. Future investigations could be directed towards evaluating the preclinical treatment's effectiveness in tumor models and the impact of different radiation doses on treatment outcomes. Moreover, the potential synergistic benefits of combining chemotherapy and radiotherapy for enhanced therapeutic effects could also be explored.

Taking a step further, we developed host-specific serum protein stabilised Ag-QCNS using sera proteins from bovine, human and murine sources and employed them for their antibacterial and wound healing ability *in-vitro*. The red emitting photoluminescent Ag-QCNS exhibited a concentration and time-dependant uptake in murine fibroblast cell lines and were found to be highly biocompatible up to a concentration of 1 mg/mL. Further, the *in-vitro* scratch assay revealed that Ag-QCNS supported cellular migratory abilities highlighting their potency as personalised wound healing agents. The antibacterial efficacy was established in both normal and kanamycin–resistant *E.coli*, which is the majorly responsible bacteria for UTI infections. The antibacterial mechanism was found to be a combination of intracellular ROS formation and cell membrane damage ultimately leading to their bactericidal effect. However, the antimicrobial efficacy of Ag-QCNS could also be enhanced even more by conjugating clinically approved antibiotics for designing personalised antibacterial nanomedicine to overcome antibiotic resistance with added feature of their real time antibacterial monitoring as personalised antibacterial theranostic nanomedicine. The preclinical safety analysis using autologous serum stabilised Ag-QCNS was carried out in Balb/c mice over a period of 28 days to reveal their acute and sub-acute toxicity. The short-term biodistribution and hemocompatibility revealed that the autologous Ag-QCNS were localised in liver and GIT during short-term pharmacokinetic biodistribution evaluation and in liver after 24 h post intravenous injection, indicating liver as primary interaction site for Ag-QCNS. The acute and sub-acute assessment of serum biochemical parameters: ALT, AST, creatinine, urea and troponin-I indicated no vital organ functioning damage. The histopathological assessment of all vital organs including skin found no atypical signature in tissue microarchitecture for 24 h and 28 days dpi, revealing their safe translational potential. Future research could delve into exploring antibiotic-conjugated Ag-QCNS and assessing their comparative preclinical efficacy in an infected wound model against Ag-QCNS alone using conventional antibiotics as positive standard controls for the treatment.

Moreover, considering their host specific nature, Au/Ag-QCNS have immense potential to be utilized in a heterogenous population, that fail to tolerate generic medicinal approaches. Additionally, other major serum proteins such as globulins and lipoproteins also have the basic chemical composition required to form Metal-QCNS. Therefore, identifying these proteins for QC formation may lead to development of targeted theranostic applications.

Appendix

List of Publications, Book Chapters & Patent

Publications:

- **Kritika Sood** *et al*; Preclinical safety assessment of photoluminescent metal quantum clusters stabilized with autologous serum proteins for host specific theranostics. Nanotheranostics (2023) Vol. 7,3 316-326
- **Kritika Sood** *et al*; PEGylated autonomous open gold nano shells derived from metal organic framework for pronounced photothermal therapy. (Manuscript under review)
- **Kritika Sood**, Asifkhan Shanavas; Autologous Serum Protein Stabilized Silver Quantum Clusters as Host Specific Antibacterial Agents. (Manuscript under review)
- **Kritika Sood**, Asifkhan Shanavas; The Role of Gold Nanoclusters as Emerging Theranostic Agents for Cancer Management. Current Pathobiology Reports, Vol 9, 33-42, 2021
- **Kritika Sood** *et al*; Cytotoxicity profile of Schiff base organotin (IV) complexes: Experimental and theoretical approach. (Manuscript submitted)
- Gagandeep Kaur *et al*. and **Kritika Sood**; Design of Silica@Au Hybrid Nanostars for Enhanced SERS and Photothermal Effect, ChemPhysChem, July 2023

Book Chapter:

- **Kritika Sood**, Asifkhan Shanavas Gold Nanoclusters as Emerging Theranostic Interventions for Biomedical Applications. In: Borse, V., Chandra, P., Srivastava, R. (eds) BioSensing, Theranostics, and Medical Devices. Springer, Singapore (2022).

Patent:

- One-pot process for preparation of metallic semi shells with metal organic framework as template: **Kritika Sood**, Purvi Mathur, Pranjali Yadav, Navneet Kaur, Rohit Srivastava, Abhijit De, Asifkhan Shanavas, (2021) *Indian patent application number: 202111016843 Date of filing: April 9, 2021.*